Multi-Frequency Study of the NVSS Foreground Sources in the Cosmic Background Imager Fields

Dissertation

zur

Erlangung des Doktorgrades (Dr. rer. nat.)

der

Mathematisch-Naturwissenschaftlichen Fakultät

der

Rheinischen Friedrich-Wilhelms-Universität Bonn

vorgelegt von

Emmanouil Angelakis

aus

Ierapetra, Griechenland

Bonn, January 2007

Angefertigt mit Genehmigung der Mathematisch-Naturwissenschaftlichen Fakultät der
Rheinischen Friedrich-Wilhelms-Universität Bonn

To my mother Evangelia Angelaki and my aunt Maria Angelaki.

Acknowledgments

The currently handed thesis is a piece of work which was frankly carried out with constant dedication, honesty and faith to the scientific spirit. It is totally outside the bounds of my authority and definitely decency, to make the slightest statement about the quality of this work. I would thus kindly ask the reader to be tolerant with any impression of pride throughout the text. It is not meant intentionally.

I feel entirely obliged on the other hand, to specifically express my gratitude to certain people that have been of any sort of assistance, help or support throughout my PhD course.

To begin with, I want to thank Professor Dr. U. Klein Priv. Doz. Dr. W. Huchtmeier for the time they allocated to me either reading my manuscript or advising me during my thesis committee meetings despite their responsibilities and limited time. Their comments have always been so important! I also want to thank them for their wholehearted friendliness. Moreover, I wan to thank Professor Dr. K. Maier and Professor Dr. C. Simmer for being so willing to be in my examination board despite the load of work they have.

I would like to express my thankfulness to my advisor Dr. A. Kraus. I thank him for sharing his knowledge and his time with me always in atmosphere of scientific enthusiasm and creativity. I am grateful for all the scientific discussions we have had during long observing nights at the 100-meter telescope. I thank him for all the encouragement, the strength and inspiration he gave me in moments of tiredness and saturation. I deeply thank him for his honesty, fairness and the patience that always provided me with a solid ground of support.

All the work I have been doing these last years would be impossible without the support of my director Prof. Dr. J. A. Zensus. I feel privileged to be in his group and to have received his trust, faith and the scientific liberty he allowed to me right from the start.

It is so difficult to summarize my gratitude to Dr. A. Witzel. He has been the authority embracing all my scientific activities with wisdom. His presence has been absolutely motivating and assuring. I want to express my thankfulness for the inspiration I have received from Dr. T. P. Krichbaum. He has been and constant source of ideas so valuable within a scientific group. I also thank Dr. R. Porcas for the encouragement and the long absolutely inspiring discussions we had.

I owe all my gratitude to the CBI part of the CBI-Effelsberg collaboration, namely Prof. Dr. A. C. S. Readhead, Dr. T. J. Pearson R. Bustos and R. Reeves. Prof. Readhead has been the Principal Investigator and the driving force of the CBI project itself. I feel entirely privileged though to have worked with them even though only for a limited time.

Contents

1. Introduction

The history of astronomy is a history of receding horizons.

Edwin Powell Hubble

Abstract

"Our universe is flat. From this it follows that the mean energy density in the universe is equal to the critical density. This is equivalent to a mass density of $9.9 \times 10^{-30}\,g\,cm^{-3}$, which is equivalent to only 5.9 protons per cubic meter. In detail, 4% of that is Atoms, 23% is Cold Dark Matter, 73% is Dark Energy. Thus 96% of the energy density in the universe is in a form that has never been directly detected in the laboratory." - WMAP outreach web site.

All those statements being observationally determined knowledge rather than the artistic abstraction of a science fiction writer, are part of the harvest of the sophisticated study of the Cosmic Microwave Background Radiation. That is, the eldest detectable light carrying all the history of the heavens that comprises the solid ground of what is nowadays called "precision cosmology".

1.1 The Cosmic Microwave Background Radiation

Crudely speaking, our universe emerged from an adiabatically expanding primordial singularity that contained all mater and energy concentrated in a single point. This is nothing but the "big bang" theory that enhanced with some fundamentally necessary modifications is attempting to describe the cosmic creation. Already this rough description implies some observationally testable facts: (a) The cosmic expansion and (b) The cosmic microwave background radiation (CMBR or CMB).

The first prediction orders that everything descends from every other point on the cosmic fabric. It was testified and quantified for the first time by Hubble (1929). As for the latter, Gamow (1946) and Alpher and Herman (1950) predicted the existence of a radiation field characterized by a black body spectrum that follows from the adiabatic expansion of the universe.

The discovery of the black body Microwave Radiation of roughly 3 K by Penzias and Wilson (1965) and was most precisely described by Dicke et al. (1965) in the same volume, came as a strong indication of the correctness of the "Big Bang" theory. Moreover, it ignited a tremendous explosion of discoveries in the field of modern cosmology.

1.2 Anisotropies in the CMB

According to the gravitational instability theory it is necessary that at the last-scattering (that is, the moment at which the universe density drops enough for it to become transparent to CMB photons) redshift

($z \approx 1000$) there must have existed fractional density fluctuations $\delta \leq 10^{-3}$ for galaxies and clusters to have subsequently formed (e.g. Peacock, 1999). Those perturbations must have been imprinted in the cosmic background radiation in the form of fluctuations in the measured temperature.

In practice, the perturbations in the CMB can be attributed to three basic effects causing such anisotropies at different angular scales:

- **Large scales**: Gravitational effect (Sachs-Wolfe): This is the result of the fact that photons from high-density regions have to climb out the potential wells with the result that they are redshifted.

- **Intermediate scales**: Intrinsic (adiabatic) perturbations. Those are induced when in high-density regions the coupling of matter and radiation can compress the latter causing an increase in the temperature.

- **Small scales**: Velocity (Doppler) perturbations. At the recombination era the plasma has non-zero velocity. That leads to Doppler frequency shifts and hence change in the brightness temperature.
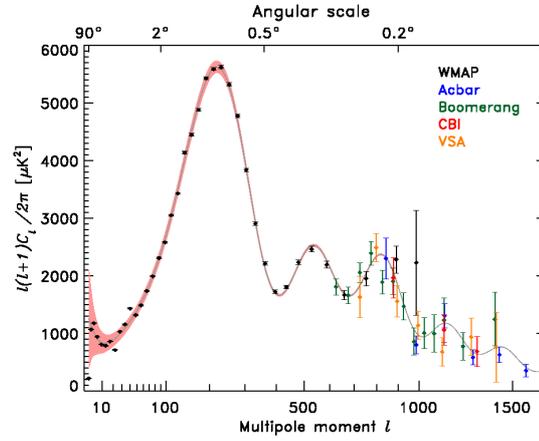
Figure 1.1: **The power spectrum of CMB anisotropies as provided by Hinshaw et al. (2006) on the basis of the 3rd-year WMAP data release. It must noted that smaller angular scales correspond to larger multipoles ℓ.**

Already from the previous discussion it is clear that the anisotropies in the brightness temperature carry a large amount of information concerning the history of the universe and its characteristics (the energy and matter and the dark matter content etc). Generally, their spatial distribution is described in terms of spherical harmonics and the the power spectrum as a function of angular scale is the tool for the estimation of all those parameters. Specifically, the temperature fluctuations ΔT are distributed in the entire sky and are described by expansion in spherical harmonics, as:

$$\frac{\Delta T}{T}(\theta, \phi) = \frac{T(\theta, \phi) - T_0}{T_0} = \sum_{\ell=2}^{\infty} \sum_{m=-\ell}^{\ell} \alpha_{\ell m} Y_{\ell m}(\theta, \phi) \tag{1.1}$$

where T_0: the average temperature
(θ, ϕ): polar coordinates
$Y_{\ell m}$: the spherical harmonic functions
$\alpha_{\ell m}$: the spherical harmonic transform coefficients with:
$\alpha_{\ell m} = \int_{4\pi} \frac{\Delta T}{T}(\theta, \phi) Y_{\ell m}(\theta, \phi) \, d\Omega$

Now, complete statistical description of the fluctuations is done through the angular power spectrum which is the two-point correlation function in Fourier space of the previous expression:

$$C_\ell = \frac{1}{2\ell + 1} \sum_{m=-\ell}^{\ell} \alpha_{\ell m} Y_{\ell m} (\theta, \phi) = |\alpha_{\ell m}|^2 \tag{1.2}$$

An example of the power spectrum is shown in figure 1.1 taken from the release of the 3rd year data of WMAP experiment.

The shape of the power spectrum depends on an extended set of parameters that describe the present properties and the history of the universe. Thus their values are computed by fitting cosmological models to the observed spectrum. A nice review is given by White and Cohn (2002).

1.3 The CMB polarization

The cosmic microwave background appears to be linearly polarized. That is not obvious at first place since it presumes the existence of a quadrupole temperature anisotropies. It is worth it a brief discussion on the matter.
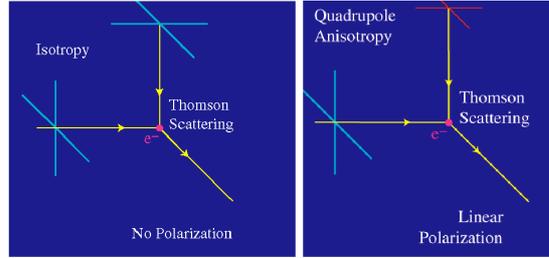
Figure 1.2: **The mechanism imposing linear polarization on the CMB photons (Hu 2001). On the left-hand side panel is shown the case of isotopic incident radiation. In the right-hand side sketches is shown the case that the radiation is characterized by quadrupole anisotropy. The blue color represents warmer and the red colder radiation. The net scattered wave then is linearly polarized.**

The interaction between a free electron and a photon is described by the Thomson scattering. During such an encounter (electron-photon) the scattered wave is polarized perpendicular to the incident direction. At the moment of the decoupling of the radiation from the matter the photon are scattered off by free electrons. This is the moment at which the universe becomes transparent and hence the one at which the CMB photons originate. Assuming that the radiation at this stage was isotropic (or had only dipole variation) then the net polarization of the scattered radiation would be zero as it is shown in figure 1.2. However, if the incident radiation approaching from perpendicular directions (separation angle 90°) had different intensities then the scattered light would be linearly polarized. This anisotropy is called "quadrupole" because the poles of the anisotropy are four ($360°/90° = 4$).

It is apparent then that the existence of a quadrupole anisotropy is essential in the production of polarization in the CMB photons. There exist three types of perturbations capable of creating such anisotropic fields:

- **Scalar**: Those are caused by density fluctuations in the plasma.

- **Vector**: These perturbations are related to vorticity in the plasma.

- **Tensor**: The Gravity waves are responsible in this case.

Technically, the study of the polarization pattern is done by analyzing the sky polarization pattern in two components:

- **Curl-free component**: This is called "E-mode" (electric-field like) or "gradient-mode" with no handedness (related to scalar perturbations). E-mode has parity $(-1)^{\ell}$. Hence, under parity change ($\hat{n} \to -\hat{n}$) it remains unchanged for even ℓ.

- **Grad-free component**: This is called "B-mode" (magnetic-field like) or "curl-mode" with handedness (related to vector perturbations). B-mode has parity $(-1)^{\ell+1}$ and under parity change it changes sign for even ℓ.
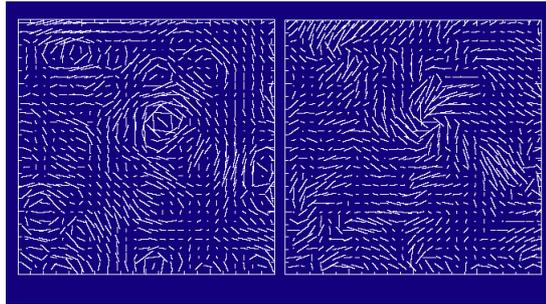
Figure 1.3:   **The pattern of the sky polarization for the purely E-mode on the left-hand side panel and the purely B-mode on the right-hand side panel.**

Both cases are shown in figure 1.3. Once maps of the E and B components are available along with that
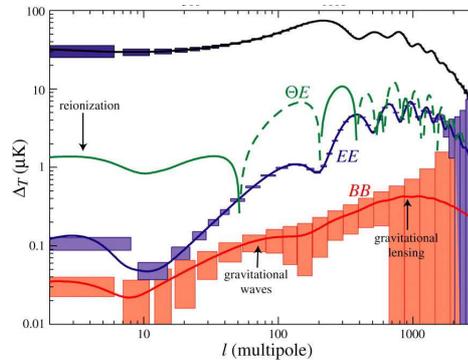
Figure 1.4:   **The power spectrum of the polarization pattern of the CMB (Hu & Dodelson 2002).**

of the temperature anisotropy, one can analyze them again in terms of spherical harmonics and study their power spectrum as it is shown in figure 1.4.

1.4   The CMB contaminants (foregrounds)

As we already discussed the cosmological parameters and characteristics are extracted from the study of the CMB that happens to be quite but not completely isotropic in terms of brightness temperature. In reality it is exactly those anisotropies that reveal many of the cosmic secrets to the scholars.

The background radiation anisotropies are of the order of $\Delta T/T \sim 10^{-6}$. Unfortunately, there is a long series of factors intervening between the last scatter surface and the observer that could cause

anisotropies of that order or even larger. It is among the most crucial tasks and the most difficult challenges to deal with the identification of anisotropies that are "intrinsic" to the CMB and thus represent universe characteristics at the last scatter surface.

For a CMB experiment it is already perplexing what is "signal" and what "foreground". A common convention is that everything around or before $z \sim 1000$ is signal (for a review see e.g. Refregier, 1999). Tegmark et al. (2000) on the other hand give a more "operational" definition of what a foreground is. According to them:

> A foreground is an effect whose dependence on cosmological parameters we cannot compute accurately from first principles at the present time.

It is interesting to at least briefly name those contamination factors and examine what angular scales each one affects.

Galactic: diffuse synchrotron emission. The synchrotron radiation from our galaxy is (see e.g. Smoot, 1999) is attributable to the relativistic electrons. Its spectrum is $\sim \nu^{\alpha}$ where the index α depends on the energy distribution of the electrons. That already implies that this contaminant is orientation-dependent because it depends on the plasma distribution. Given that the synchrotron radiation is polarized this may contaminate both the total power data and the polarization of the CMB. The influence that this factor may have spans practically throughout the entire $\ell-$space (Tegmark et al., 2000).

Galactic: free-free emission. The frequency dependence of the free-free emission is best known among the galactic foregrounds and it is described by a power law decay. Scattering off of free electrons within H_{II} regions may cause polarization of the free-free emission (Keating et al., 1998). The domination of the free-free emission is mainly at low multipoles.

Galactic: dust emission. This component originates at vibrating dust grains in the interstellar medium and is described by black body radiation. It can be highly polarized in case the dust grains are in local magnetic field (Wright, 1987). This component is significant at all multipoles.

Sunyaev-Zel'dovich effect: Thermal and kinematic. The thermal Sunyaev-Zel'dovich (SZ) effect is the characteristic distortion of the black body spectrum of the CMB induced by hot ionized gas in galaxy clusters (Sunyaev and Zeldovich, 1970). The kinematic SZ effect is due to matter fluctuations. The influence of the latter is rather small. The former on the other hand is an important factor mainly dominating large ℓ's.

Point sources. This component is the one we are dealing with. It refers to the contamination of the CMB data due to the existence of a point source on the line-of-sight. Given that most experiments target sky fields far from the galactic plane so that this contaminants are minimum, the point sources are mostly extra-galactic source (generally, they are active galaxies). Depending on how polarized a source is it can significantly distort the polarization of the CMB sky. Most often the treatment of this issue is statistical on the basis of the number counts of sources per sr and flux density unit. Alternatively, people tend to rule out pixels of CMB maps that coincide with the position of such a source. That results the loss of data and consequently lower signal-to-noise ratios. The point sources affect strongly the high multipoles that is the small angular scales.

1.5 The Cosmic Background Imager

The detection of the anisotropies has been a challenge and only upper limits were set prior to 1992. Their discovery took place with *Differential Microwave Radiometer* an instrument aboard the Cosmic

Background Explorer (COBE, e.g. Mather 1982) probe by Smoot et al. (1992)[1]. The angular resolution characterizing the first detection by was only 7°. After this momentous discovery a long series of experiments were set to study the anisotropies with always better sensitivity and higher angular resolution.

Figure 1.5: **The Cosmic Background Imager (CBI) at its open configuration for observing with high angular resolution. This mode is for total intensity measurements.**

Among the most prominent experiments in the field and one amongst those with the highest resolution is the Cosmic Background Imager (CBI, Padin et al., 2002). It is located at an altitude of 5080 meters near San Pedro de Atacama, in northern Chile (at the same site lies the APEX telescope). It is an interferometer made of 13 70-cm elements mounted on a 6 meter platform operating in ten 1-GHz frequency bands from 26 GHz to 36 GHz (see figure 1.5). The instantaneous field of view of the instrument is 44 arcmin and its resolution ranges from 4.5 to 10 arcmin. That gives the ability to do construct images of the CMB and study its statistical properties on angular scales from 5 arc minutes to one degree (spherical harmonic scales from $l = 3000$ down to $l = 300$, see figure 1.1).

The CBI is imaging the anisotropies in the CMB within four "patches" in the sky located far from the galactic plane in order to minimize the influence on the observations of the galactic emission (see table in sub-section 2.1.4 and figure 2.3).

Apart from total power measurements, CBI is capable of conducting also deep polarization maps (Readhead et al., 2004).

1.6 Introduction to the current study

The commonly followed strategy to resolve the problem of point source contamination has been the removal of the contaminated pixels from CMB maps. This method has many drawbacks such as the fact that it is usually based on low frequency surveys, it does not account for variability etc. Besides, it apparently results a significant data loss decreasing the sensitivity of the experiment. Within the CBI fields there exist as many as almost 6000 point sources as detected by the NRAO VLA Sky Survey (NVSS, Condon et al., 1998). Given the fact that around each such source an area of a few beams has been removed makes clear how severe the problem may be.

For all these reasons it has been decided that a alternative method should be followed. In brief, that is:

---

[1] John C. Mather and George F. Smoot were awarded the The Nobel Prize in Physics for the year 2006 "for their discovery of the blackbody form and anisotropy of the cosmic microwave background radiation"

The identification of those NVSS sources that can indeed contribute a flux density of the order of a few mJy at the frequency regime of the CBI operation (26-36 GHz). Afterwards, only those sources should be vetoed out during the CMB data analysis.

Ideally that could in principle be done by re-targeting those NVSS "suspicious" sources with a telescope operated at the frequency of 31 GHz (central frequency of the CBI band) with enough sensitivity to reach the desirable flux density limit. That appeared to be highly time-consuming even for the 100-meter telescope at Effelsberg forbidding the implementation of such a plan. Alternatively, one could measure the flux density of the sources at different frequencies. Assuming then a power law ($S \sim \nu^\alpha$) evolution of the spectrum in the radio regime one can extrapolate at higher frequencies. Particularly for the needs of CBI, we have employed the 4.85 and the 10.45 GHz receivers mounted on the secondary focus of the 100-m Effelsberg telescope. Those are among the most stable receivers and the central frequencies are less sensitive to atmospheric conditions and hence are more efficient. Having available for each source the 1.4, 4.85 and 10.45-GHz flux density one can calculate the three-point spectral index and the high frequency extrapolated flux.

1.7 The rest of this thesis

A careful consideration will make it clear that the previously mentioned sample observed at those three frequencies can serve as a basis of several studies that can prove beneficial in different ways. There has been put effort in keeping each different research direction in a single chapter.

Chapter 2. The requirement of reaching very low flux density limits while being time-efficient has forced us to operate the 100-m telescope close to its theoretical limits. That has inevitably revealed peculiarities in its behavior which demanded special care. As a result a totally new software pipeline was developed in order to automate the data reduction. The most important details concerning the observations and the data reduction are included there.

Chapter 3. In this chapter we include the actual results that of the current work which are directly related to the initial proposal of the project. Parallel to that other studies such as the quantification of the system repeatability are presented.

Chapter 4. As it was described earlier, the extrapolation of the spectrum to higher frequencies and hence the estimation of each source contribution at the CBI frequency regime, is done with the help of the three-point spectral index. The extended sample of 6000 sources is an excellent probe of the statistics of those sources.

Chapter 5. The extrapolation of the flux densities to different frequencies provides with the opportunity to estimate the expected sources counts at each such frequency. Comparing those results with the ones from independent surveys can be very fruitful in estimating the completeness of such studies etc. Most importantly though for the current study is the estimation if the "confusion limit" expected at each band. This study among others is presented there.

Chapter 6. Although most of the current work shares a rather statistical approach on the several topics it important to note that the studied sample comprises an rich pool of interesting individual sources to be revealed. Sources like GHz Peaked Sources or High Frequency Peakers are among them. Such investigations are reported here.

Chapter 7.   The CBI-Effelsberg survey has definitely not been designed for polarization studies. However, there has been attempted that the statistical properties of the polarization are investigated.

2. Observations and Data Reduction

> *To measure is to know.*
>
> Lord Kelvin (Sir William Thomson)

Abstract

The first chapter was meant as a very brief introduction to the CMB and the anisotropies in its temperature. From the discussion there it is clear that those anisotropies are exceptionably weak ($\Delta T/T \sim 10^{-6}$). This fact justifies all the effort that has been put in the study of foregrounds. For the currently presented project a great amount of time was invested in reaching very low flux density levels within very short integration times. In other words, it was attempted to operate the 100-meter telescope at its theoretical limit. That demanded the development of new data analysis technique etc that eventually proved very time consuming. It is worth therefore discussing the most important points of this work that occupied admittedly a significant part of the project duration.

2.1 Observations

For the flux density measurements the multi-beam heterodyne receivers at 4.85 and 10.45 GHz have been used. Both systems are mounted on the secondary focus cabin of the 100-meter telescope. Solely for efficiency reasons, the "on-off" method has been employed. The calibration has been done by observing "main" calibrators with well known flux densities. All the important details related to the observational part of the work are discussed here.

2.1.1 The observing system

The most important characteristics of the receivers used are summarized in table 2.1. A detailed block diagram is included in appendix B. Both receivers are multi-beamed allowing the subtraction of mostly linear atmospheric effects as is demonstrated in sub-section 2.1.2 by having always one of the horns pointing "on-source" and another pointing "off-source". The angular distance between the two beams is 485 arcsec for the 4.85 GHz receiver and 182 for the 10.45 GHz one (i.e. ~3 FWHM in each case). As a matter of fact the 10.45 GHz receiver consists of rather four independent horns the signal from which could be used for a statistically more precise atmospheric effects subtraction. For the project reported here and for reasons of uniformity and consistency between the two receivers, only two horns of each receiver have been used. For each receiver the one is designated as "main" and the other as "reference" horn.

Each horn detects and outputs simultaneously left and right circular polarization signals (hereafter LCP and RCP, respectively). Those are routed through independent channels. This may have important

Table 2.1: The most important characteristics of the receivers used. T_{cal} **is the presumably constant thermodynamic temperature of the noise diode that is used for the stabilization of each receiver (see sub-section 2.1.1).** T_{sys}^{zenith} **is the system antenna temperature at the zenith.**

Frequency (GHz)	T_{cal} (K)	T_{sys}^{zenith} (K)	Bandwidth (MHz)	sensitivity (K/Jy)	FWHM (arcsec)	Beam separation (arcsec)
4.85	1.8	27	500	1.5	145	485
10.45	9.0	50	300	1.3	65.8	182.4

consequences concerning for example their stability, their system temperature and the gain. Conventionally, they are designated as channel A, B for the LCP and RCP signal respectively of the main horn and channel E, F for that of the reference horn[1]. Table 2.2 clarifies this notation.

Table 2.2: The notation used for the total intensity data channels.

Horn	LCP	RCP	Stokes Q	Stokes U
Main	A	B	C	D
Reference	E	F	G	H

The receiver stability is controlled by using a noise diode of known temperature. An excellent discussion on several engineering problems being encountered during the design of high quality low noise receivers is given by Rohlfs and Wilson (2004). The noise diode is furthermore used for the translation of the received astronomical signal from voltage to units of antenna temperature (for more details see subsection 2.1.1).

The conversion of K to Jy ($10^{-26}\,\mathrm{W\,m^{-2}\,Hz^{-1}}$) is done by observing the "main" calibrators. That is, sources of well defined flux density by independent methods. For consistency the same four calibrators have been observed throughout the duration of the project. In table 2.7 are summarized their fluxes at the two frequencies of interest. A detailed description of this step is given in subsection 2.2.3.

The role of the noise diode: the primary calibration

As shown in figures B.1 and B.2 the calibration and the gain control is done with the help of a noise diode of known temperature. The diode's signal is "fed" in the system exactly after the horn. Thus it is also routed through all the steps that the sky signal is passing.

As a working assumption let us denote the power from the sky P and the signal from the diode D for any given channel. Both P and D at this stage are in units of voltage or in arbitrary "counts". The data recoding then is done in four steps or "phases". For our project the duration of each phase is set to 16 ms. The physical meaning of one phase is that it is the interval over which the received photons are integrated to produce the detected signal. Each phase includes the signal from the sky P. During the last two phases though also the diode is switched on (for 16 ms in each phase) and added to the recorded signal. Finally the four phases are added together. The total power then integrated over the 64 ms that all

---

[1]Channels C, D, G and H contain Stokes parameters Q and U

four phases put together last (hereafter sig, as it is designated within the standard data analysis package at Effelsberg, namely *Toolbox*), can be written as:

$$sig = P_1 + P_2 + (P_3 + D_3) + (P_4 + D_4) \tag{2.1}$$

where P_i: the power from the sky in phase i

            D_i: the power from the noise diode in phase i

Assuming that over the 64-ms cycle both the sky signal P and that from the diode, D are constant (that is $P_i = P$ and $D_i = D$), equation 2.1 gives:

$$sig = P + P + (P + D) + (P + D) = 4\,P + 2\,D \tag{2.2}$$

With a different combination of the 4 phases one can construct a second signal namely cal (following the designation in *Toolbox* package) as follows:

$$cal = -P_1 - P_2 + (P_3 + D_3) + (P_4 + D_4) \Rightarrow cal = -P - P + (P + D) + (P + D) = 2\,D \tag{2.3}$$

Equations 2.2 and 2.3 give the handle for performing the calibration operation which is nothing but the comparison of sig to cal. Provided that the temperature of the noise diode T_{cal} is known and given that both sig and cal are in the same arbitrary units (counts), the calibrated signal measured in K, hereafter antenna temperature T_A, will be:

$$T_{\text{A}} = \frac{sig}{2\,cal}\,T_{\text{cal}} = \frac{4\,P + 2\,D}{4\,D}\,T_{\text{cal}} = \left(\frac{P}{D} + \frac{1}{2}\right)T_{\text{cal}} \tag{2.4}$$

As long as the standard data reduction package used at Effelsberg is concerned, the above operation is done on the one-data-point basis. That is, each data point (usually two four-phase cycles) is calibrated individually. This inherits potential dangers when low flux density levels are attempted as in the case of the current project. Essentially, the problem arises when the assumption that both the gain of the receiver and the signal from the diode are stable brakes. As it will be shown later (sub-section 2.4.2) this may cause severe data distortion. To prevent that from happening a newly used slightly modified calibration procedure is applied as will be discussed in that paragraph.

2.1.2   The "on-off" versus "cross scan" technique

The technique routinely used for flux density measurements of point sources at Effelsberg has been the "cross scans" one. The method relies on "scanning" with the main beam over the source position in both elevation and azimuth direction (hence the term "cross"). Simultaneously, the reference horn is scanning the assumed empty sky. The subtraction of the two signals produces one that is in principle free of linear atmospheric effects (differential observing).

Assuming that the measured source is point-like and that the beam pattern is described by a Gaussian, the observed flux density distribution (which is the convolution of the beam pattern and the sky brightness distribution e.g. Kraus 1986) will be a Gaussian. Its peak corresponds then to the flux density of the measured source; its center corresponds to the true position of the source including all necessary coordinate transformations and the telescope pointing model; its *Full Width at Half of the Maximum power* (FWHM) to that of the telescope beam.

This method has two advantages. Firstly, it provides instantaneous information about the possible existence of confusing sources in the observing vicinity. In case there were a source nearby the targeted one it would immediately be detected as an additional peak in the observed flux density distribution. Secondly, it makes possible the correction for power losses due to "pointing" errors. These are introduced when the source is observed slightly off the horn center where the sensitivity is not maximum. This is the case whenever there appears a divergence between the source position and the intersection of the two

scanning directions (azimuthal and elevation). Ideally, those two points should coincide. Since the peak of the observed flux density distribution corresponds to the "real" source position and assuming to know the beam pattern as a function of the offset distance, one can correct for such errors (see Kraus, 1997).

However, the disadvantage of this technique is its limited time efficiency that makes it inadequate for projects demanding large amounts of observing time. Indeed, most of the observing time is spent for telescope driving rather than on-source integration. For instance, with the default Effelsberg settings the slewing distance in total is ∼5 FWHM. Then only 1/5 of the observing time is spent on on-source integration.

Contrary to that is the "on-off" method which appears prominently efficient in terms of observing time. This technique is also differential. It is based simply on observing "on" and "off" the source and subsequently subtracting the power measured at those two stages (for a more complete description see subsection 2.1.3). In cases that multi-beam systems are available, like in the current project, simultaneous observation of the sky and the source are possible. This results a dramatic increase of the efficiency in subtracting atmospheric effects as is shown in figure 2.2.

Despite its efficiency, this method suffers mainly from three problems. The first is related to the often false assumption that the source is observed with maximum sensitivity. Even when the position of the source is known precisely, there exist telescope pointing errors. That results in observing the source with a pointing offset causing a recorded power loss. The second problem arises from the potential of another source being in any of the two beams (reference or main) during the observation. This problem being termed as "confusion" can prove very severe as is demonstrated in subsection 2.4.1. Finally, it is only an assumption that the "off" position of a beam is indeed off the source which can be contributing some power in the side-lobes.

For the current project the "on-off" method has been applied mainly because the same flux density level is reached in shorter observing time. A detailed description follows in sub-section 2.1.3.

2.1.3 The "on-off" method with the help of two horns
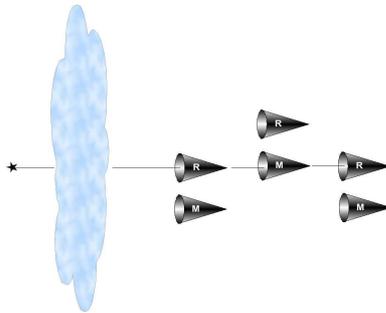
Figure 2.1: **The observing scheme. The reference horn is designated with the letter "R" and the main one with "M". Each measurement consists of four sub-scans. Since the feeds lie on a plane parallel to the horizontal the driving of the telescope for the realization of the on-on method is done on the azimuthal direction.**

In understanding much of the following material it is essential that the details of the observing technique as it has been realized for our observations are explained. For both receivers a measurement, termed as a "scan", is done at four stages or "sub-scans". In figure 2.1 the exact arrangement of the main and the reference horn with respect to the source for each sub-scan is illustrated. As shown there, there is always a horn observing on-source. This observing fashion is termed as "on-on" rather than the traditional "on-off". Let us consider the signal detected and consequently recorded from each horn at each sub-scan. Everything is summarized in table 2.3. There, T_{src} stands for the source temperature and

Table 2.3: **The signal recorded at each sub-scan in each channel and the duration of each sub-scan.**

Horn	sub-scan 1	sub-scan 2 and 3	sub-scan 4
Main	$T_{\text{sys-1}}\,(t)$	$T_{\text{sys-23}}\,(t)+T_{\text{src}}$	$T_{\text{sys-4}}\,(t)$
Reference	$T_{\text{sys-1}}\,(t)+T_{\text{src}}$	$T_{\text{sys-23}}\,(t)$	$T_{\text{sys-4}}\,(t)+T_{\text{src}}$
Main−Reference	$-T_{\text{src}}$	T_{src}	$-T_{\text{src}}$
Length in seconds for 4.85/10.45 GHz	13/50	26/100	13/50

$T_{\text{sys-i}}$ is the system temperature during sub-scan i. Considering that the system temperature may signif-icantly change from one sub-scan to the next this convention makes the study more realistic compared to assuming a constant T_{sys} for each channel and scan. As it is discussed in subsection 2.2.3 T_{sys} refers to cumulatively everything but the signal from the source (e.g. see equation 2.24). From this table it is obvious that after subtracting the reference horn from the main horn output it is possible to get rid of every contribution apart from T_{src}. The resulted intensity profile depends only on the source temperature T_{src} which can immediately be measured by simply measuring the half difference between the intensity in the first sub-scan and that in the second one or in the third and the fourth.

$$T_{\text{src}} = \frac{1}{2} \cdot \left(\frac{S_2 - S_1}{2} + \frac{S_3 - S_4}{2} \right) \tag{2.5}$$

where s_{i}:   The average of the signal is sub scan-i after the subtraction

This way there are two independent measurements that can afterwards be averaged. Besides, the dif-ference between them (which is attributed to the non-perfect atmospheric contribution subtraction) gives an estimate of the real uncertainties in the actual measurement (see error calculation in sub-section 2.2.1).

A closer look in the operations described above shows that the on-on method (as any other differential method) can prove efficient only under certain assumptions:

- The system temperature $T_{\text{sys-i}}$ is assumed to be horn-independent. Simply put, T_{sys} at a given sub-scan is the same for both horns. Of course this is not the case in a realistic system already due to the fact that each channel is processed independently. However, as it is shown in figure 2.2 the result is satisfactory.

- The system temperature is assumed to be constant over the entire sub-scan. From the principle of the method it appears that this should not cause any complications. But combined with channel-dependent gain factor result in different amplification in different channels for the same signal.

- The horns are presumably pointing at the same part of the sky and hence recording exactly the same signals as regards the noise contributors (atmospheric emission, CMB etc.). This is definitely not completely true.

Nonetheless, the efficiency of the method is still superb especially in cases of atmospheric behavior which is linear with time. This is clearly shown in figure 2.2. It must be pointed out though, that in fact the "on-on" method of course can be constructed by any possible combination of sub-scans and durations of them. For example, one could design a similar pattern that consists of more in number and shorter in length sub-scans that afterwards are averaged. This would behave as a "low-cut" filter for long term atmospheric changes. On the other hand, it would demand more telescope driving time.
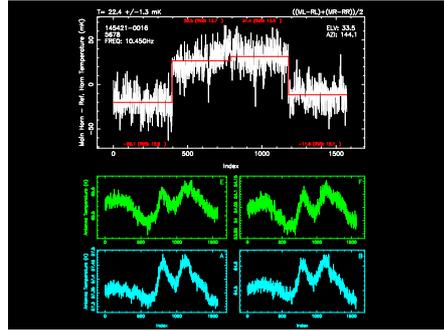
Figure 2.2: **The efficiency of the "on-on" method. In the upper panel of the plot is the "detection profile". That is, the result of the subtraction of the signal from the two horns. In light blue are the channels A and B that correspond to the main horn and in green channels B and F corresponding to the reference horn. As it is shown there, the peak-to-peak antenna temperature variation is of the order of 100 mK and the source is no brighter than roughly 25 mK.**

2.1.4 Observing strategy

The Cosmic Background Imager observations are confined within four well defined regions or "fields" in the sky selected to be far from the galactic plane as shown in figure 2.3. Their boundaries are:

Field name	NE (RA,DEC)	NW (RA,DEC)	SW (RA,DEC)	SE (RA,DEC)	Area (deg^2)	
02-Hour	(3,2)	(2.65,2)	(2.65,−5.5)	(3,−5.5)	5.5×7.5	=41.3
08-Hour	(9,0)	(8.6,0)	(8.6,−5.5)	(9,−5.5)	6×5.5	=33.0
14-Hour	(15,0.5)	(14.6,0.5)	(14.6,−7)	(15,−7)	6×7.5	=45.0
20-Hour	(21,−2)	(20.6,−2)	(20.6,−8)	(21,−8)	6×6	=36
					155=0.047 sr	

Notice: the RA is measured in hours and the DEC in degrees

In total there exist as many as 5998 NVSS source that comprise the sample that has been observed. A large portion of the observing time has been spent on auxiliary studies that hopefully by the end of the current report will prove themselves of great importance. The observing strategy that appeared to be optimum, can be summarized in the following points.

Organization: First of all, the observations have been organized so that the telescope driving time is least (problem similar to the *traveling salesman problem*). That was achieved by driving the telescope in the field in a "zig-zag" way. Each field has been organized in stripes parallel to the right ascension axis and half a degree across in declination. The sources within such a belt have been organized in dozens in order of monotonous (in each stripe) right ascension change as shown in figure 2.4. During an observing session each field would be targeted within *Hour Angle* range from -3 to 3 hours.

Calibration: At the beginning of each field a calibration source (see table 2.7) would be measured after having the pointing and the focus of the receivers corrected. For each field the same calibrator has been being used at all times. At the end of each field the calibrator of the next field would be measured again for a second calibration factor determination (see subsection 2.2.3). This measurement would be done after only pointing corrections.
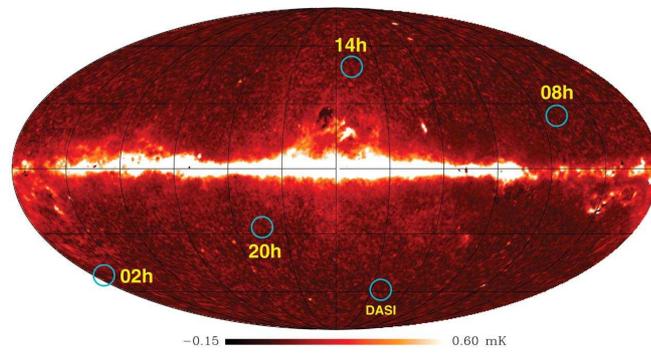
Figure 2.3: **CBI fields marked on the "K-band" (26-35 GHz) image of the Milky Way as observed by WMAP satellite. Each field is named after the corresponding right ascension.**
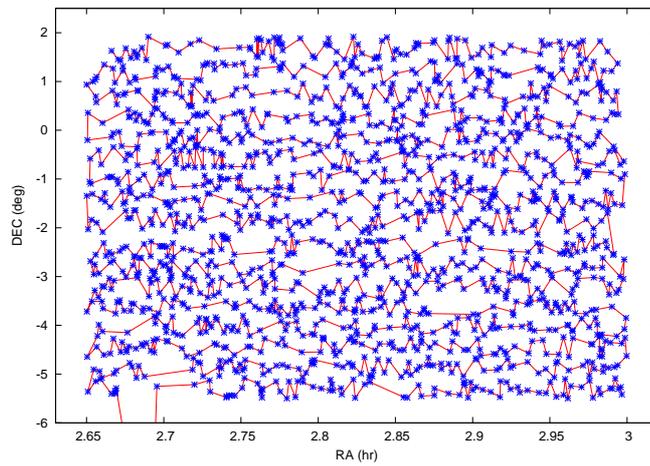
Figure 2.4: **The organization of the observations. The blue symbols represent the NVSS sources and the red line the advance of the telescope.**

Pointing sources: For each field three bright sources, either within the field or in its very vicinity, have been selected for performing pointing corrections (every one or two dozen sources). The "pointing" sources have been selected basically on the basis of their flux density so that they can be used for pointing correction at both frequencies. They have been measured both with cross-scans and on-ons so that a comparison of the two methods could be carried out later. In case of a detected systematic difference, corrections could be applied (for a complete study see subsection **??**).

Repeaters: A considerable portion of observing time has been invested in quantifying the "repeatability" of the system. For each field a sample of $\sim$10 sources has been selected to serve as "repeaters". That is, sources which are expected to show no significant intrinsic variability and hence to be of repeatable flux density. Any divergence from their otherwise assumed constant flux (within the bounds of errors) can be attributed to systematics. This study is of great importance since it reveals the most realistic uncertainty in a measurement by taking into account every possible source of error such as weather effects, receiver instabilities, confusion etc. This study is formally presented in subsection 2.3.

Simultaneity: Since the goal is the accurate determination of the spectral index, it is important that the two frequencies are observed quasi-simultaneously. However, this is only partially done since the unstable weather conditions demand flexibility provided that the 10.45-GHz observations are far more sensitive to them than the 4.85-GHz ones. Therefore, compromise has often been necessary ending up with non-simultaneous measurements.

Time budget: The integration time has been 52 s for the 4.85 GHz observations and 200 s for the 10.45 GHz ones. A small overhead imposed by the back-end and the front-end system increased the time per source to roughly 1 min and 4 min respectively. Each dozen of sources (one dozen is one loop) took approximately $\sim$15 min for the former and $\sim$55 min for the latter frequency. The excess time is mainly because of telescope driving.

2.2 Data reduction

It has been mentioned in subsection 2.1.3 that the measurement of a source temperature boils down to estimating the distance between two consecutive sub-scans in the profile following the subtraction method. The involved details allow the calculation of the formal errors. However, this is only the first step towards the determination of the source flux density in its own rest frame. Indeed, after having measured the "raw" source brightness temperature several corrections must be applied in order to extract the flux density of the source. All these are discussed in the immediately following paragraphs.

2.2.1 Actual measurement

For the discussion that follows it is essential that the individual channels are let into play (see table 2.2). Throughout the following, the signal in channel X during sub-scan i as a function of time will be conventionally designated as x_i. In practice, such a signal is a time series of antenna temperatures. The average over the whole sub-scan i is denoted as X_i so that $X_i = \langle x_i \rangle_t$. Moreover, the system temperature which is of course a function of time and channel in denoted as $T_{\text{sys-i}}^{\text{X}}$. Finally, $T_{\text{src}}^{\text{LCP/RCP}}$ is the corresponding circular polarization comment of the source temperature. Everything is measured in K.

As has been discussed in subsection 2.1.3, the signal in channels A, B (main horn) and E, F (reference horn) is as in table 2.4.

Subtracting the signal in channel E from that in channel A one derives the left circular polarization total intensity. Accordingly, the signal in channel F subtracted from that in B gives the right circular

Table 2.4: The signal detected and recorded by each channel per sub-scan.

Channel	sub-scan 1	sub-scan 2 and 3	sub-scan 4
A	$a_1 = T_{\text{sys-1}}^{\text{A}}$	$a_{23} = T_{\text{sys-23}}^{\text{A}} + T_{\text{src}}^{\text{LCP}}$	$a_4 = T_{\text{sys-4}}^{\text{A}}$
B	$b_1 = T_{\text{sys-1}}^{\text{B}}$	$b_{23} = T_{\text{sys-23}}^{\text{B}} + T_{\text{src}}^{\text{RCP}}$	$b_4 = T_{\text{sys-4}}^{\text{B}}$
E	$e_1 = T_{\text{sys-1}}^{\text{E}} + T_{\text{src}}^{\text{LCP}}$	$e_{23} = T_{\text{sys-23}}^{\text{E}}$	$e_4 = T_{\text{sys-4}}^{\text{E}} + T_{\text{src}}^{\text{LCP}}$
F	$f_1 = T_{\text{sys-1}}^{\text{F}} + T_{\text{src}}^{\text{RCP}}$	$f_{23} = T_{\text{sys-23}}^{\text{F}}$	$f_4 = T_{\text{sys-4}}^{F} + T_{\text{src}}^{\text{RCP}}$

polarization total intensity. This subtraction is done simply by subtracting the recorded data point by point. From this already one can extract the T_{src} provided that the source is not circularly polarized[2]. Otherwise, the two results should be averaged. So, the pipeline for extracting the T_{src} from the data, is: If s denotes the power after all the operations described earlier, it is:

Table 2.5: The resulted signal per sub-scan after the differentiation is applied.

Operation	sub-scan 1	sub-scan 2 and 3	sub-scan 4
$a - e$	$-T_{\text{src}}^{\text{LCP}}$	$T_{\text{src}}^{\text{LCP}}$	$-T_{\text{src}}^{\text{LCP}}$
$b - f$	$-T_{\text{src}}^{\text{RCP}}$	$T_{\text{src}}^{\text{RCP}}$	$-T_{\text{src}}^{\text{RCP}}$
$\frac{(a-e)+(b-f)}{2}$	$s_1 = -T_{\text{src}}$	$s_{23} = T_{\text{src}}$	$s_4 = -T_{\text{src}}$

$$s = \frac{a - e + b - f}{2} \qquad (2.6)$$

After having worked out s its average along with its uncertainties for each sub-scan is calculated. For each sub-scan i therefore the average S_i ($=\langle s \rangle_i$) is calculated as well as its uncertainty in that. Then the source temperature can be extracted from half the difference of the average in sub-scan 1 and 2 or 3 and 4. Denoting the former as T_{I} and the latter as T_{II}, we have:

$$T_{\text{I}} = \frac{S_2 - S_1}{2} \qquad (2.7)$$

$$T_{\text{II}} = \frac{S_3 - S_4}{2} \qquad (2.8)$$

T_{I} and T_{II} comprise a set of two independent measurements of the antenna temperature that can be averaged for a better approximation of the source observed antenna temperature:

$$T_{\text{obs}} = \frac{T_{\text{I}} + T_{\text{II}}}{2} = \frac{S_3 - S_4}{4} + \frac{S_2 - S_1}{4} \qquad (2.9)$$

It is important here to clarify the used notation. So far we have been referring to the source antenna temperature as T_{src} to keep the operations simple. In reality though, the observed source antenna temperature

---

[2]This is a reasonable assumption given that the extragalactic radio sources usually have circular polarization $\leq 0.5\,\%$ (Weiler and de Pater, 1983)

T_{obs} needs to be corrected as discussed in sub-section 2.2.3. Therefore, from now on the result of the actual measurement before any corrections will be noted as T_{obs} so that after applying all the necessary corrections on can reconstruct the "real" source temperature T_{src}.

Provided that theoretically T_{I} and T_{II} should be identical (the source flux density is unlikely to change is such short time intervals), their difference can be attributed to any source of uncertainty. Therefore, their difference can provide a good estimate of the error in our measurement (see subsection 2.2.2).

Parallel to the actual measurement there take place a long series of operations. Among them measuring the system temperature which, as it appears in table 2.4, can be extracted simply from the off subs-cans of the individual channels.

2.2.2   The thermal limit

Before working out the errors in a measurement it is useful to examine the expected lowest reachable flux density for the applied integration times.

Since the receivers used are operated in total power mode (see table 4.2 Rohlfs and Wilson, 2004) the thermal noise level reachable σ_{th}, with integration time t will be given by:

$$\sigma_{\text{th}} = \frac{K \cdot T_{\text{sys}}}{\Gamma \cdot \sqrt{\Delta\nu \cdot t}} \tag{2.10}$$

where K: Receiver dependent constant (usually $K \simeq 1 - 2$). In our case $K = \sqrt{2}$
         T_{sys}:   the system temperature
         Γ: the sensitivity of the telescope that is the K to Jy factor
         $\Delta\nu$:   the receiver bandwidth
         t: the integration time

For the values given in table 2.1 and for integration time of 1 minute for the 4.85 and 4 for the 10.45 GHz, we get:

$$\sigma_{\text{th},4.85} = \frac{\sqrt{2} \cdot 27\,\text{K}}{1.5 \cdot \sqrt{500\,\text{MHz} \cdot 52\,\text{s}}} = \frac{0.24}{1.5}\,\text{mK} = 0.16\,\text{mJy}^3 \tag{2.11}$$

and

$$\sigma_{\text{th},10.45} = \frac{\sqrt{2} \cdot 50\,\text{K}}{1.3 \cdot \sqrt{300\,\text{MHz} \cdot 200\,\text{s}}} = \frac{0.29}{1.3}\,\text{mK} = 0.22\,\text{mJy}^4 \tag{2.12}$$

According to these values one could reach very low flux densities levels. Particularly, 1 mJy is achievable with a confidence level of $\sim 10\,\sigma$ at either frequency. Of course, this is only a theoretical estimation that is not feasible. As will be shown later (sub-section 3.2.3) the achievable flux density limit is larger though still satisfactory.

Errors analytically

The definitions described in subsection 2.2.1 already provide the necessary background for the calculation of the formal error in a single measurement.Nonetheless, this is only an estimate of the uncertainty in a single measurement.

According to the Gaussian statistics the uncertainty in the final measurement T_{obs} of the source temperature σ_{obs} depends on the statistical scatter of the data. From the error propagation theory we have:

$$\sigma_{\text{obs}} = \sqrt{\left(\frac{\partial T_{\text{obs}}}{\partial T_{\text{I}}}\right)^2 \cdot \sigma_{\text{I}}^2 + \left(\frac{\partial T_{\text{obs}}}{\partial T_{\text{II}}}\right)^2 \cdot \sigma_{\text{II}}^2} = \frac{1}{2} \cdot \sqrt{\sigma_{\text{I}}^2 + \sigma_{\text{II}}^2} \tag{2.13}$$

---

[3]Assuming a sensitivity Γ of 1.5
[4]Assuming a sensitivity Γ of 1.3

where σ_{I}:   the formal error in the measurement of T_{I}

         σ_{II}:   the formal error in the measurement of T_{II}

It happens so that it is:

$$\sigma_{\mathrm{I}} = \sqrt{\left(\frac{\partial T_{\mathrm{I}}}{\partial S_1}\right)^2 \cdot \sigma_1^2 + \left(\frac{\partial T_{\mathrm{I}}}{\partial S_2}\right)^2 \cdot \sigma_2^2} = \frac{1}{2} \cdot \sqrt{\sigma_1^2 + \sigma_2^2} \tag{2.14}$$

and

$$\sigma_{\mathrm{II}} = \sqrt{\left(\frac{\partial T_{\mathrm{II}}}{\partial S_3}\right)^2 \cdot \sigma_3^2 + \left(\frac{\partial T_{\mathrm{II}}}{\partial S_4}\right)^2 \cdot \sigma_4^2} = \frac{1}{2} \cdot \sqrt{\sigma_3^2 + \sigma_4^2} \tag{2.15}$$

where σ_i: the uncertainty in the average in sub-scan i

So, equation 2.13 with the help of 2.14 and 2.15, will give:

$$\sigma_{\mathrm{obs}} = \frac{1}{2} \cdot \sqrt{\left(\frac{1}{2} \cdot \sqrt{\sigma_1^2 + \sigma_2^2}\right)^2 + \left(\frac{1}{2} \cdot \sqrt{\sigma_3^2 + \sigma_4^2}\right)^2} = \frac{1}{4} \cdot \sqrt{\sigma_1^2 + \sigma_2^2 + \sigma_3^2 + \sigma_4^2} \tag{2.16}$$

This is the formal uncertainty in the calculation of T_{obs}. On the other hand, as we discussed earlier at the end of sub-section 2.2.1 the diffrence between T_{I} and T_{II}. Hence, the final error at a given measurement, will be:

$$err = \max\left(\frac{T_{\mathrm{I}} - T_{\mathrm{II}}}{2}, \sigma_{\mathrm{obs}}\right) \tag{2.17}$$

2.2.3 Corrections

As soon as a measurement has been performed and the source temperature has been calculated, three corrections must necessarily be applied in order for the source flux density to be correctly determined. These are namely the "opacity", "gain-curve" and the "sensitivity" correction.

Opacity corrections

As for any ground-based radio astronomical observations the signal detected by the receiver has traveled through the Earth's atmosphere and hence experienced several distortions such as attenuation or atmospheric emission. The latter is resolved by executing the differential observation. The attenuation effect on the other hand must still be corrected for. This correction is described as "opacity" correction.

The earth's atmosphere is fairly transparent to radio waves over a considerable frequency range from a few tens of MHz ($\lambda \sim 10\,\mathrm{m}$) to a few THz ($\lambda \sim 0.1\,\mathrm{mm}$). The lower limit is attributed to the reflection of radio waves on the ionosphere. The reflectivity of the latter is due to free electrons. The cut off frequency ν_{p}, is given by:

$$\frac{\nu_{\mathrm{p}}}{\mathrm{kHz}} = 8.97\sqrt{\frac{N_{\mathrm{e}}}{\mathrm{cm}^{-3}}} \tag{2.18}$$

where ν_{p}:   cut-off frequency

         N_{e}:   plasma electron density

and it is of the order of a few tens of MHz. The upper limit is mainly due to the resonant absorption of molecules in the troposphere. Potentially, any atmospheric constituent could cause absorption as long as their resonance bands overlap with that of the signal. However, the major absorption factor is the water molecule present in the atmosphere in the form of vapor absorbing at 22.2 GHz and the oxygen ones absorbing at 183 GHz.

Despite the atmosphere acting as a radio wave attenuator it also acts as an emitter. Assuming the atmosphere to be in in local thermodynamic equilibrium any of its components can behave as black body radiators. Hence, not only is the radiation from a celestial source attenuated by traveling through the atmosphere, but also blended with radiation emitted by the atmospheric constituents themselves. This nothing but the radiative transfer problem where the medium is the terrestrial atmosphere. The basics of this problem are discuss in appendix A.

In the radio regime, where the Rayleigh-Jeans approximation is valid, equation A.5 can be expressed in terms of temperature as:

$$T_\mathrm{b} = T_\mathrm{src}\, e^{-\tau_\mathrm{atm}} + T_\mathrm{atm} \left(1 - e^{-\tau_\mathrm{atm}}\right) \tag{2.19}$$

where T_b: observed brightness temperature
            T_src: "real" source brightness temperature
            T_atm: effective atmospheric radiation temperature
            τ_atm: opacity at the source elevation

This equation describes the radiative transfer of radio waves through the Earth's atmosphere. The first term of the right-hand side part of equation 2.19 describes the attenuation of the source signal due to the presence of the atmosphere. The right-hand side part represents the radiation and absorption of the atmosphere itself.

In the above it has been implied that the atmosphere behaves as an single-temperature T_atm black body radiator which of course is far from true. A more realistic approach would assume isothermal layers of gas and integrate over the whole atmosphere thickness. However, since the change in the gas density with altitude is much faster than that of temperature the introduction of the effective temperature is a well-working reasonable approximation. The effective temperature of the atmosphere can be approximated, by:

$$T_\mathrm{atm} = 1.12 \cdot T_\mathrm{ground} - 50\,K \tag{2.20}$$

where T_ground: the ground temperature

The atmospheric emission term: The antenna temperature level attempted for the current project is only a few mK. It is important then to make sure that any source of noise is efficiently subtracted from the actual signal. Among the most prominent factors of noise is the atmospheric emission itself. A "back off the envelope" calculation can demonstrate its level. For a typical summer day ($20°$) equation 2.20 gives the effective atmospheric temperature to be $\sim$278 K. On the other hand, a usual value for the zenith opacity at 4.85 GHz is $\sim$0.017. Assuming the observation of a source at 30 degrees elevation the opacity is then roughly 0.034. The right-hand-side term then in equation 2.19 is $\sim$9 K at corresponds to the emission from the atmosphere. This is an admittedly large antenna temperature compared to the source temperature.

The importance of the differential observing method comes into play exactly here. Since the atmospheric emission signal is recorded by both horns then the subtraction of the two signals frees the result from this very influence. This is the main reason why multi-beam systems have been developed. The same method however is applied even for single-feed systems with the support of auxiliary methods (e.g. "choppers" or simply by performing either "on-off" or cross-scan measurements). However, as has already been pointed out this works only under some assumptions that are scratched in subsection 2.1.2.

To summarize, the atmospheric emission part is discarded by applying the differential method. This term though provides an excellent method for calculating the zenith atmospheric opacity τ_z which in turn is necessary for correcting for the absorption. These matters are discussed in the next paragraph.

The atmospheric absorption term: Assuming then that the atmospheric emission is fully subtracted during the differentiation a correction for the absorption term, namely "opacity" correction must still be applied. The source temperature corrected for the atmospheric absorption temperature T_{opc} is calculated from the observed one T_{obs}, from:

$$T_{\text{obs}} = T_{\text{opc}} \cdot e^{-\tau_{\text{atm}}} \Rightarrow T_{\text{opc}} = T_{\text{obs}} \cdot e^{\tau_{\text{atm}}} \tag{2.21}$$

where T_{obs}:   observed source temperature
         T_{opc}:   the source temperature outside the atmosphere
         τ_{atm}:   opacity at the source elevation

From the last equation it is obvious that the opacity corrections boils down to the calculation of the correct atmospheric opacity τ_{atm} at the elevation of the observation. This is approximated by:

$$\tau_{\text{atm}} = \tau(ELV) = \tau_{\text{z}} \, AM = \tau_{\text{z}} \, \frac{1}{\sin(ELV)} \tag{2.22}$$

where τ_{z}:   the opacity at the zenith (ELV=90°)
        AM: the "air mass" $AM = 1/\sin(ELV)$
        ELV: the source elevation

From the previous discussion it is clear that is crucial to correctly calculate the opacity at zenith, τ_{z}. Interestingly, this is done by utilizing atmospheric emission term. The next paragraph is meant to thoroughly explain the applied method.

The opacity calculation: In case the telescope is pointing to an astronomically empty part of the sky then the received signal will correspond to the system temperature (T_{sys}). That can be resolved in its constituents (a) the emission from the atmosphere that is a function of elevation and (b) every other contribution cumulatively described as T_0 that is mostly elevation-independent:

$$T_{\text{sys}} = T_0 + T_{\text{atm}} \left(1 - e^{-\tau_{\text{atm}}}\right) = T_0 + T_{\text{atm}} \left(1 - e^{-\tau_{\text{z}} \, AM}\right) \tag{2.23}$$

This equation is similar to equation 2.19. The difference is that the first term need not be modulated by $e^{\tau_{\text{atm}}}$ because it is not traveling through the atmosphere. Now, T_0 can be further analyzed into well established factors, as follows:

$$T_0 = T_{\text{rec}} + T_{\text{CMB}} + T_{\text{ground}} + T_{\text{ant}} + T_{\text{RadBack}} \tag{2.24}$$

where T_{rec}:   receiver noise temperature
       T_{CMB}:   cosmic microwave background
       T_{ground}:   radiation from the ground (spillover). It is elevation dependent
       T_{ant}:   antenna temperature
     T_{RadBack}:   radio background from blends of weak sources (confusion), radio background etc.

For $\tau \ll 1$ the previous relation can be expanded in a Taylor series. After keeping the first order term, it follows that:

$$T_{\text{sys}} \simeq T_0 + T_{\text{atm}} \, \tau = T_0 + T_{\text{atm}} \, \tau_{\text{z}} \, AM = T_0 + T_{\text{atm}} \, \tau_{\text{z}} \, \frac{1}{\sin(ELV)} \tag{2.25}$$

Presuming that T_0 and τ_{z} are constant, the system temperature is a function of the effective atmospheric temperature and the airmass (AM) which in turn is a function of elevation, in a linear fashion. Therefore, at any given T_{atm} the T_{sys} will increase linearly with increasing airmass (decreasing elevation). In figure 2.5 an example of system temperature against airmass is plotted over an airmass range. Points of system temperatures well above the straight line trend can be attributed mainly to weather effects that cause an increase in T_{sys}. Practically, for each observing session all scans have been used for the construction of such plots. After fitting a lower envelope to these data points one can extract the following information:
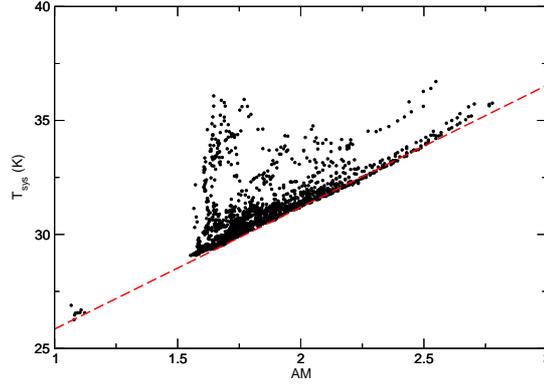
Figure 2.5:   **System temperature as a function of airmass (or elevation) for a given observing session. This example is for 4.85 GHz. The red line is the lower envelope to the data. It slope gives the zenith opacity and the cross-section with the y-axis provides T_0. Incidents of fast increase in the system temperature are clearly seen and they correspond to weather changes or any other effect that could possibly affect it (receiver disfunction etc.).**

- τ_z: from the slope of the fitted line since $slope = T_{atm} \cdot \tau_z \cdot AM$

- T_0: from the point where the fitted line crosses the abscissa axis (T_{sys})

Consequently, for each individual measurement the zenith opacity τ_{atm} is calculated from the original equation 2.23:

$$\tau_{atm} = -\frac{1}{AM} \cdot ln \left(1 - \frac{T_{sys} - T_0}{T_{atm}} \right) \tag{2.26}$$

where T_{sys}:   is the system temperature for the associated scan
         T_{atm}:   the effective atmospheric temperature from equation 2.20

and used in equation 2.21 for the calculation of the actual source temperature.

Alternative to this method is the often used "sky-dip" technique which is based on measuring the T_{sys} at different elevations free of astronomical sources. According to a recent trend especially in the Very Long Baseline Interferometry field, radiometers are used for the direct opacity measurement particularly around 22 GHz (water spectral line).

"Gain curve" corrections

The mass of a 100-meter telescope is so large ($\sim$ 3200 tons) that it easily distorts its otherwise assumed perfect parabolic shape. Traditionally, all the effort has been put in constructing structures rigid enough to resist the gravitational effect.

The 100-meter radio telescope at Effelsberg has been the first one to be designed on the basis of the homology principle (von Hoerner, 1967). According to that, instead of exhaustingly aiming the construction of unbendable structures, the movable compartments of the telescope have been chosen so that the shape of the telescope even after the deflection remains parabolic. That is on the cost of slightly displacing the focal point. Then optimum gain is achieved by accordingly displacing the receivers so that they are always on the focal point. This takes place dynamically so that when the source is being tracked there takes place a continuous change of the receiver position so that it always lies on the focal plane.

However, small scale deformations of the reflector lower the sensitivity of the antenna. That is simply due to an increase in its rms. Since the deformation of the reflector is elevation-dependent it is apparent that the gain of the antenna is elevation-dependent. The "gain curve" is the plot that shows the antenna gain as a function on elevation and it is used for correcting this effect as described immediately.
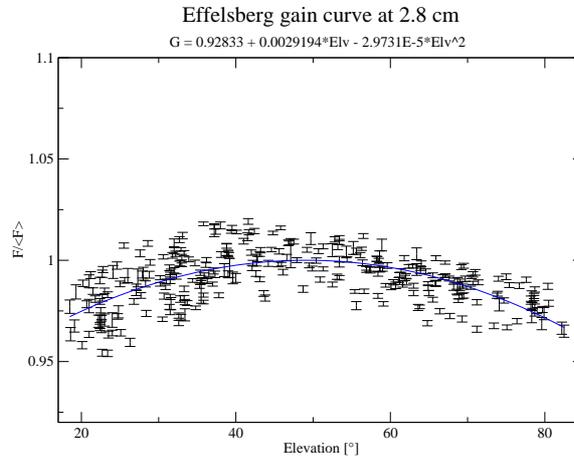
Figure 2.6:   **The "gain curve" at 2.8 cm as measured during November 2003.   That is the normalized gain versus elevation. The maximum lies around 45-50 degrees.**

Selected sources, preferably non variable (e.g. steep spectrum sources are not likely to vary on short time scales), are being observed regularly. The sources are selected to also uniformly cover the equatorial coordinates space (azimuth, elevation). By plotting all the normalized flux density measurements as a function of elevation one can construct the so-called "gain curve" (hence the correction term). An example is illustrated in figure 2.6. The gain curve is a parabola[5] with its maximum corresponding to gain equal to unity:

$$G(ELV) = A_0 + A_1 \cdot ELV + A_2 \cdot ELV^2 \tag{2.27}$$

This formula then can be used for correcting the subsequent measurements. For observed source temperature T_{obs} the one corrected for the gain curve effect T_{gc}, will be:

$$T_{\mathrm{gc}} = \frac{T_{\mathrm{obs}}}{G(ELV)} = \frac{T_{\mathrm{obs}}}{A_0 + A_1 \cdot ELV + A_2 \cdot ELV^2} \tag{2.28}$$

The parameters of the gain curves that have been used for the current project are presented in table 2.6. It must be noted that the gain curve changes with time and hence within the duration of the current project.

Sensitivity corrections

So far, all the brightnesses have been referred to in units of temperature. The conversion from voltage (which is what the telescope physically delivers) to antenna temperature units is achieved during the primary calibration with the comparison of the signal to that from a load of known temperature as described in subsection 2.1.1. However, it is essential that the signal is further translated into Jy as the source temperature is telescope dependent. For that the "sensitivity" Γ (i.e. K/Jy) must be known. That

---

[5]The parabola is only a good approximation

Table 2.6: **The parameters of the fitted gain curves for both frequencies.**

Frequency	A_0	A_1	A_2
10.45 GHz	0.97493	$1.2035 \cdot 10^{-3}$	$-1.4439 \cdot 10^{-5}$
4.85 GHz	0.98834	$6.9824 \cdot 10^{-4}$	$-1.0455 \cdot 10^{-5}$

is achieved by frequently measuring the sources of independently known flux density. These source are the "calibrators" and are chosen to be of temporally unchanging flux density. The sensitivity is frequency dependent. For a given factor Γ the corrected flux density S_{src} of a source that has been measured to have antenna temperature T_{src}, will be:

$$S_{\mathrm{src}}\,[\mathrm{Jy}] = \frac{T_{\mathrm{src}}\,[\mathrm{K}]}{\Gamma\,[\mathrm{K/Jy}]} \tag{2.29}$$

It is worth noting that Γ could in principle be calculated theoretically since (see Rohlfs and Wilson, 2004, equation 7.17):

$$\Gamma = \frac{\pi}{8\,k}\,n_{\mathrm{A}}\,D^2 = 2.84\,10^{-4}\,n_{\mathrm{A}}\,D^2 = 2.8\,n_{\mathrm{A}}\,\mathrm{K/Jy} \tag{2.30}$$

where n_{A}:   aperture efficiency
         D: antenna diameter

However, n_{A} is the result of several effects. Consequently, the exact theoretical computation of Γ is not trivial to calculate.

The calibrators and the Γ factor: In table 2.7 the flux densities of the calibrating sources are summarized along with their type and their spectral index. As already mentioned, the calibration sources are selected on the basis of several criteria. Among them, the stability of their emission which is confined to no more than a few percent. As has already been mentioned, the determination of Γ is achieved by

Table 2.7: **The calibrators.**

Source	$S_{4.85}$ (Jy)	$S_{10.45}$ (Jy)	Spectral Index[*] $\alpha_{1.4}^{4.85}$	Type	Reference
3C48	5.48	2.60	-0.88	Quasar	1, 2, 3
3C161	6.62	3.06	-0.82	Radio Galaxy	1, 2, 3
3C286	7.48	4.45	-0.54	Quasar	1, 2, 3
NGC7027	5.48	5.92	$+1.12$	Planetary Nebulae	1, 2, 3

[*]: Computed from the NVSS 1.4 and CBI-Effelsberg 4.85 and 10.45 GHz measurements.

1: Kraus priv. Comm.

2: Ott et al. (1994)

3: Baars et al. (1977)

observing the calibrators. Any changes in the telescope characteristics therefore (e.g. focus, pointing etc.) may affect the value of Γ and hence introduce an error in the flux densities of the target sources. For example, in case the focus parameters are not properly set then the receiver is not lying correctly on the focal plane causing a loss of power in terms of antenna temperature. From the definition of Γ

then it follows that it will be underestimated. This example is chosen on purpose since not only is it the most common one but also because it can be relatively easily resolved. As it is discussed in sub-section 2.1.4, at the beginning of each field the focus is corrected by observing one of the main calibrators. That gives the "correct" Γ factor. Within the subsequent roughly 5 to 6 hours span, during which the field is observed, the focal plane may be displaced without having the new parameters determined. This refers to deformations of the reflector different from those described by the homology principle. That could be for instance because of sunlight warming up the reflector. A reasonable treatment is, to re-observe a calibrator and determine the sensitivity before focus corrections at the end of the field. That results a sensitivity factor of a "short sighted" telescope. Then, for the sources observed in between a linear interpolation is used.

The typical values of Γ determined by observing these sources are roughly 1.5 and 1.3 K/Jy for the 4.85 and 10.45 GHz receiver, respectively. Γ is expected to vary less than a few percent.

The final source flux density: To conclude this section it is wise summarize all the data processing steps in a way consistent with the notation used earlier and easily understood. Once the antenna temperature of a source $T_{\mathbf{obs}}$ has been measured, the following steps eventually lead to the source flux density:

Telescope output: $T_{\mathbf{obs}}$	Calculated from equation 2.9
Opacity correction: $T_{\mathbf{opc}}$	The previously calculate temperature is corrected for opacity effects for 2.21
Gain curve correction: $T_{\mathbf{gc}}$	The source temperature that has been corrected for opacity is corrected for gain curve effect as described by equation 2.28
The final source flux density: $S_{\mathbf{src}}$	The temperature that has experienced the previous corrections is divided by Γ as in equation 2.29.

Of course, at each step of the data reduction the formal error propagation theory is applied for calculating the final errors.

2.3   Repeatability study: the overall uncertainty

It has been mentioned often that a large portion of the observing time has been used for auxiliary studies such as calibration or pointing control etc. Among them the namely "repeatability" checks. That is, observations that will reveal how repeatable a given measurement is in practice and therefore be setting a realistic limit on the confidence for a measurement.

The idea behind that is very simple. A sample of roughly 10 sources (termed as "repeaters") have been selected from each field and repeatedly observed once each time the field is observed. Then, sources of error such as the weather, the receiver instability, calibration errors and so on, will result a distribution of the flux density for the same source around a mean value that is assumed to be the true one. The rms of of those distributions can be used for characterizing the error in a single measurement.

The sample has been selected on the basis of two criteria:

1. **Intrinsically non-variable:** Since the goal is to observe the uncertainties resulting from any possible factor, it is crucial that the monitored source has no intrinsic variation. Sources of steep spectrum ($\alpha < -0.5$ with $S \propto \nu^{\alpha}$) are not likely to be variable. Hence most of the "repeaters" have been chosen to be of steep spectrum.

2. **Uniform flux density coverage:** It is essential that a uniform coverage of flux densities is achieved, for the range of interest. That is, a few mJy to a few Jy.

The flux density and the spectral index of the repeaters are shown in table 2.8. The $S_{4.85}$ and the $S_{10.45}$ there are the weighted averages of several measurements. For each repeater the average flux

density at each frequency has been calculated. The rms in such measurements must reflect the realistic uncertainty for a single measurement at that flux density level and frequency. The plots of the rms as a function of S are shown in figures 3.2 and are referred to as "repeatability" or "S-rms" plots. Sub-section 3.2.1 provide a thorough discussion of these topics.

Table 2.8: **The repeaters, the pointing sources and the calibrators that were used for the investigation of the system repeatability. Most of the repeaters are chosen to be steep spectrum so be unlikely to vary. The flux density at 4.85 and 10.45 GHz here is the weighted average over all measurements. Note the agreement between the spectral indices between 1.4 and 4.85 and 1.4 and 10.45 GHz. Note that the fluxes of the calibrators are slightly different here. That is because the values here are the average measured ones.**

Name	$S_{1.4}$(mJy)	$S_{4.85}$(mJy)	$S_{10.45}$(mJy)	$\alpha_{1.4}^{4.85}$	$\alpha_{4.85}^{10.45}$
		Repeaters			
024747+0131	276.6	75.6	29.3	−1.050	−1.098
024941+0134	60.4	15.0	4.9	−1.128	−1.199
025020+0130	39.0	8.0	2.5	−1.289	−1.275
025341+0100	562.3	137.1	50.7	−1.133	−1.178
025438+0056	117.4	75.3	52.8	−0.374	−0.412
025515+0037	30.5	32.6	63.9	0.077	0.362
025613+0039	19.4	25.8	17.7	0.189	−0.036
025615+0057	16.5	10.4	3.5	−0.422	−0.507
025631+0041	72.8	20.6	7.0	−1.078	−1.085
025800+0113	11.8	5.9	5.1	−0.517	−0.542
025825+0103	35.8	8.4	3.9	−1.170	−1.294
084037−0034	22.2	3.8	2.1	−1.539	−1.306
084550−0051	113.6	55.3	30.6	−0.598	−0.669
084601−0040	30.1	11.4	3.5	−0.807	−0.985
084709−0047	62.0	21.7	8.3	−0.828	−1.029
084721−0025	72.4	18.4	5.9	−1.101	−1.238
084840−0034	131.4	37.2	16.9	−1.055	−1.079
084950−0010	40.3	12.3	5.2	−0.879	−0.932
085255−0023	32.0	12.3	6.4	−0.749	−0.842
085418−0036	57.5	17.6	8.0	−0.976	−0.978
144043+0017	69.6	20.2	7.8	−1.001	−1.115
144119+0025	84.4	23.8	10.4	−1.023	−1.049
144232+0019	30.1	7.9	5.0	−1.033	−1.077
144505+0027	19.8	9.0	4.5	−0.621	−0.876
144615+0009	57.5	17.5	7.6	−0.969	−1.012
145004+0024	50.5	13.9	4.6	−1.118	−1.204
145421−0016	83.6	33.6	17.3	−0.724	−0.793
145430−0030	23.5	11.0	4.9	−0.589	−0.671
145548−0037	66.5	36.9	20.5	−0.486	−0.625
145554−0037	32.1	28.9	13.3	−0.063	−0.447
204952−0245	114.7	29.3	9.8	−1.091	−1.244
205001−0249	261.1	95.4	46.5	−0.807	−0.870

Continued on Next Page...

Table 2.8 – Continued

Name	$S_{1.4}$(mJy)	$S_{4.85}$(mJy)	$S_{10.45}$(mJy)	$\alpha_{1.4}^{4.85}$	$\alpha_{4.85}^{10.45}$
205041−0249	25.9	20.9	16.0	−0.276	−0.273
205155−0243	13.1	3.4	2.3	−0.963	−0.907
205240−0156	44.1	13.0	4.8	−0.927	−1.105
205546−0204	93.6	24.3	8.5	−1.135	−1.200
205612−0206	90.4	21.1	12.0	−1.093	−1.080
205616−0155	62.8	17.2	6.5	−1.099	−1.117
Pointing sources					
024104−0815	912.5	1399.8	1538.3	0.342	0.277
024137−0647	769.7	212.8	94.4	−1.027	−1.056
024240−0000	4848.1	1892.7	954.8	−0.750	−0.817
085509−0715	1156.6	424.2	199.7	−0.817	−0.878
085537+0312	617.7	220.0	102.3	−0.839	−0.901
090225−0516	1198.0	301.4	117.8	−1.110	−1.158
144839+0018	1651.5	570.4	253.0	−0.859	−0.937
145510−0539	1027.7	316.9	148.3	−0.950	−0.966
150334−0230	1040.3	337.1	140.2	−0.910	−0.993
203640−0629	1044.6	974.0	801.7	−0.051	−0.135
204710−0236	2282.2	898.0	483.2	−0.749	−0.775
Calibrators					
3C48	16370.0	5524.4	2607.5	−0.875	−0.917
3C161	18680.0	6635.1	3035.1	−0.824	−0.904
3C286	14660.0	7541.1	4457.2	−0.541	−0.590
NGC 7027	1360.0	5454.4	5973.4	1.119	0.735

2.4 Systematics

Considerable amount of time and effort has been invested in carrying out studies concerning the system it self. Meaning, not only the observing machinery but also the techniques used. This need arises from the quest for reaching very low flux density levels. Furthermore, the available data from the current project comprise a statistically substantial volume that is very appealing in conducting such studies. A great deal of insight and understanding of the system has already been gained. Here are summarized the most important points of this knowledge that may prove essentially important in future projects. Some more detailed points have been pushed to the appendix B.

2.4.1 Confusion

Among the most crucial problems encountered during this project is the "confusion". It is apparent that one or more field sources may be in the reference and/or the main beam causing severe data distortion. A careful look in table 2.9 gives immediately some idea of how severe the problem may appear to be. In fact, whole idea of the differential observation is based on the fact that the T_{sys} is the same in the two horns. Obviously, any flux density contribution in the one horn absent from the other will result

asymmetries that will destroy the efficiency of the method. That could very well happen by the existence of a source other than the target in any of the two beams.

Around 20% of the observations experience some sort of confusion at 4.85 GHz and 7% at 10.45 GHz. The latter percentage is smaller due to the smaller beam-width. See table 3.1 where the precise numbers are presented. The small percentage in the latter case is due to the smaller beam size (see table 2.1). It is highly important though to note that this is only on the basis of the NVSS catalog. As discussed soon the reality is slightly better since most of the sources are already faint enough at 4.85 GHz.
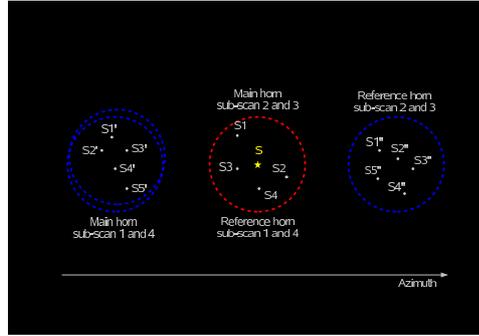
Figure 2.7: **The horns arrangement as a function of time during the execution of an "on-on" observation. In blue is the horn that "off" source each time and in red the one on source. Within each horn there can be a population of confusing sources the flux of which is represented by S_i with i being an index. Confusing sources of same index but prime or double prime are in different regions in the sky. S in yellow is the target source.The two blue circles on the left hand side are misplaced because the sky rotates within a scan.**

In designing an analytical way of resolving the problem, which is indeed the goal, it is inevitable to elaborate on the subject further. The following analysis is entirely done in the (RA,DEC) space. The position of each horn at each sub-scan has already been discussed in subsection 2.1.3 and is shown in figure 2.1. Assume a certain orientation, for instance of the 4.85-GHz dual beam system, with respect to the target source and a distribution of confusing sources as shown in figure 2.7. There, the target is represented by the yellow star symbol. In that illustration there are three distinguished populations of sources.

The "ON" population: These are the sources that lie within a circle of radius one FWHM about the target source. Hence the term "ON" since they are populating the beam that is "ON" source. In the reference illustration those sources are designated as S_1, S_2 and so on. Cumulatively, this group will contribute a brightness temperature:

$$T_{\mathrm{ON}} = \sum_i T_i \tag{2.31}$$

where T_i: the brightness temperature contribution of source S_i

The "SUB-1,4" population: These are the sources that are located within a circle of one FWHM of the horn position during sub-scan 1 or 4. In figure 2.7 these are described by S'_1, S'_2, S'_3 etc. This position is that of the main horn during the 1$^{\mathrm{st}}$ and 4$^{\mathrm{th}}$ sub-scan. In total, this population will contribute a brightness temperature:

$$T_{1,4} = \sum_i T'_i \tag{2.32}$$

where T'_i: the brightness temperature contribution of source S'_i

The "SUB-2 and 3" population: Similarly to the cases before these are the sources occupying the beam during sub-scans 2 and 3. This is the position of the reference horn during the those sub-scans. Their contribution then will be:

$$T_{2-3} = \sum_i T_i^{''} \tag{2.33}$$

where $\quad T_i^{''}:\quad$ the brightness temperature contribution of source $S_i^{''}$

It must be noted that in equations 2.31, 2.32 and 2.33 T_i, $T_i^{'}$ and $T_i^{''}$, respectively are brightness temperature contributions at the frequency of interest and not the brightness temperatures of the corresponding sources. That is, they are the brightness temperatures of the associated sources (at the correct frequency) multiplied by the beam sensitivity at the offset from the beam center that they are located. Being put simply, if a source has an intrinsic brightness temperature T_{src} and is lying $x_0^{''}$ from the center of the beam of the 4.85 GHz system, its temperature brightness contribution, will be:

$$T = T_{src} \cdot e^{-4 \ln(2) \frac{x_0^2}{FWHM^2}} \tag{2.34}$$

where $\quad FWHM:\quad$ the beam-width

Therefore, sources which lie at $x_0 \geq FWHM$ have only a negligible contribution.

From the above it is clear that T_{ON}, T_{1-4} and T_{2-3} will be added to the system temperature T_{sys} changing dramatically the ideal situation described in subsection 2.2.1. Let us consider the new situation that obviously is realistic. The question then is what does the actual observation measure?

In table 2.3 has been gathered the signal in each channel for each sub-scan. In the light of the current approach also the contributions of the confusing sources should be added. The revised table is presented in 2.9. There their circular polarization is neglected. This is a very reasonable assumption given the very

Table 2.9: **The signal detected and recorded by each channel per sub-scan taking into account the presence of the confusing sources. Here it is assumed that the latter are circularly unpolarized. The contribution of the confusing sources is in bold letters.**

Horn	sub-scan 1	sub-scan 2 and 3	sub-scan 4
Main	$T_{sys-1} + \boldsymbol{T_1}$	$T_{sys-23} + T_{src} + \boldsymbol{T_{ON}}$	$T_{sys-4} + \boldsymbol{T_4}$
Reference	$T_{sys-1} + T_{src} + \boldsymbol{T_{ON}}$	$T_{sys-23} + \boldsymbol{T_{2\text{-}3}}$	$T_{sys-4} + T_{src} + \boldsymbol{T_{ON}}$

low average degree of polarization of radio sources. Under these conditions one can work only on the LCP channels A and E. The generalization then to channels B and F is trivial. In table 2.5 is summarized the signal in each sub-scan after the subtraction of the reference from the main beam signal for each polarization. Accounting for the confusing sources results the revised table . Preserving the notation used in equation 2.9, the observable T_I and T_{II} are given by equations 2.7 and 2.8, respectively and will be:

$$T_I = \frac{S_2 - S_1}{2} = T_{obs} + T_{ON} - \frac{T_{2-3}}{2} - \frac{T_1}{2} \tag{2.35}$$

$$T_{II} = \frac{S_3 - S_4}{2} = T_{obs} + T_{ON} - \frac{T_{2-3}}{2} - \frac{T_4}{2} \tag{2.36}$$

The terms T_{obs} and T_{ON} in practice cannot be resolved because of the physical limitation of angular resolution. These cases are characterized as "clusters". It is hence meaningless to refer to them separately.

Table 2.10:   **The resulted signal per sub-scan after the differentiation is applied. Note the contribution of confusing sources (in bold letters).**

Operation	sub-scan 1: S_1	sub-scan 2 and 3: $S_{2,3}$	sub-scan 4: S_4
$S =$ Main-Reference	$-T_{\mathrm{src}} + \boldsymbol{T_1} - \boldsymbol{T_{\mathrm{ON}}}$	$T_{\mathrm{src}} + \boldsymbol{T_{\mathrm{ON}}} - \boldsymbol{T_{2-3}}$	$-T_{\mathrm{src}} + \boldsymbol{T_4} - \boldsymbol{T_{\mathrm{ON}}}$

In fact it is recommended to embody the latter in the former term. That means that the measured source brightness temperature is that of all the sources within the beam put together. It can be written then that:

$$T_{\mathrm{I}} = T_{\mathrm{obs}}^* - \frac{T_{2-3}}{2} - \frac{T_1}{2} \tag{2.37}$$

$$T_{\mathrm{II}} = T_{\mathrm{obs}}^* - \frac{T_{2-3}}{2} - \frac{T_4}{2} \tag{2.38}$$

where T_{obs}^*: $T_{\mathrm{obs}} + T_{\mathrm{ON}}$ from now on

From equations 2.37 and 2.38 it turns out that it is very likely that the observable T_{I} and T_{II} are misinterpreted as the source brightness temperature T_{obs}. Imagine for instance the trivial case of a source of $T_{\mathrm{obs}} = (T_{2-3} + T_1)/2$. In this case $T_{\mathrm{I}} = 0$ and equation 2.7 will give $T_{\mathrm{obs}} = 0$ that is completely misleading (notice that this case may result in flux density 0 for a source of any brightness. Illustration 2.8 shows some typical examples of "confused" observations. As it apparent there, it surprising how distorted impression may be given when confusion is not taken into account.

Resolving the confusion problem

The decided strategy for dealing with the confusion problem has been the "analytical" one. That is based on identifying the sources that may be confusing the observations and calculating their contribution analytically. The algorithm may be divided into segments as follows:

1. **Identification of the confusing sources:** From knowing the precise equatorial coordinates of the targeted source, the exact location of the telescope, the LST at which the observation has been performed, the angular separation of the two beams and their orientation one can reconstruct the exact position of each beam in the (RA,DEC) plane. Afterwards, every NVSS source that falls within a circle about the center of each beam of radius that corresponding to 10% sensitivity is pinpointed as confusing. This way the three groups/populations are constructed. At the same time the confusion case for each sources is constructed. The different confusion flavors that can occur and the corresponding resolution is organized in table 2.11.

2. **Calculation of brightness temperature contributions:** Assuming the brightness temperature of every confusing source at the given frequency as well as its offset from the center off the corresponding beam to be known, its contribution is given by equation 2.34. The confusing source temperature must known from an independent measurement during which it is not confused.

3. **Final source brightness temperature calculation:** After having calculated T_1, T_{2-3} and T_4 the corrected source brightness temperature will be given by:

$$T_{\mathrm{obs}} = T_{\mathrm{I}} + \frac{T_{2-3}}{2} + \frac{T_1}{2} \tag{2.39}$$
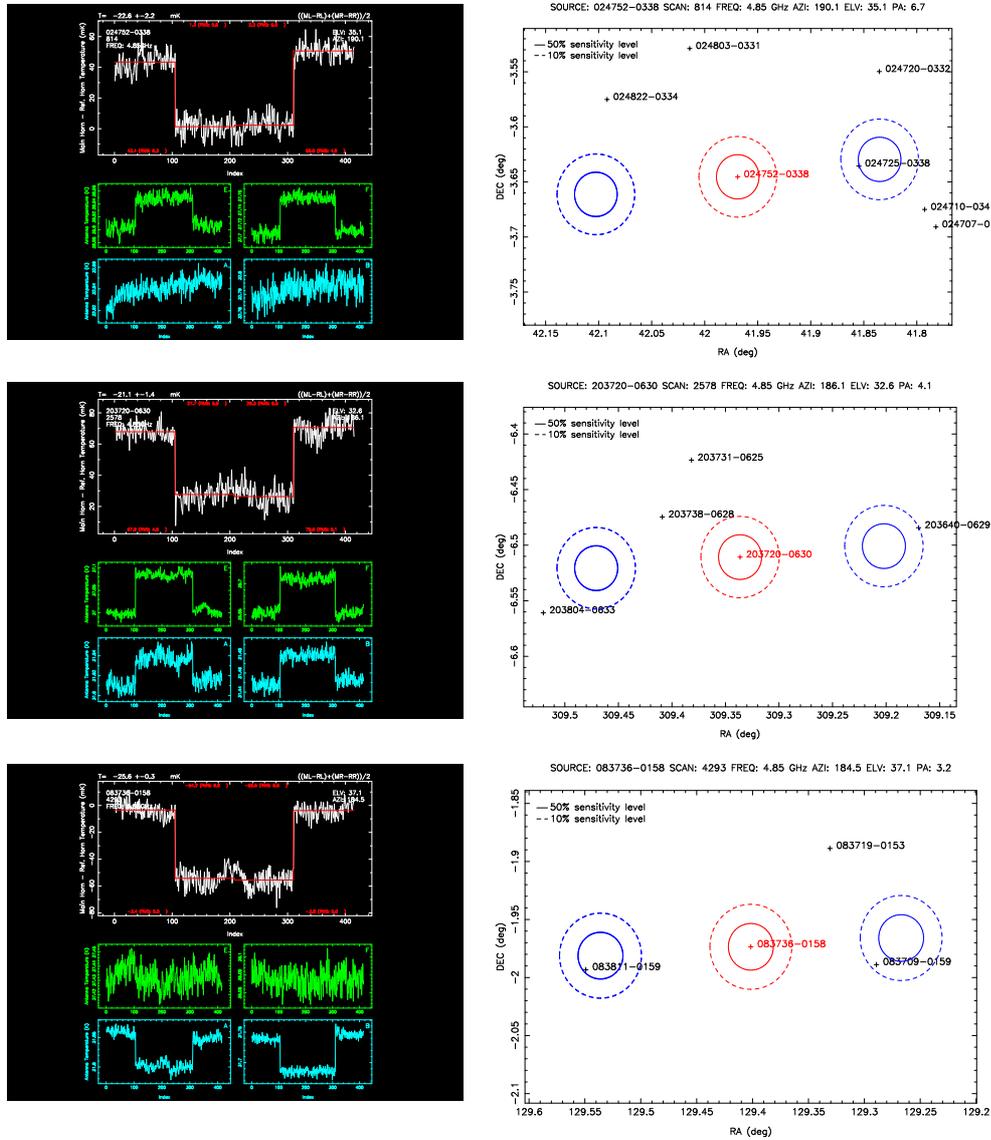
Figure 2.8: **Examples of confusion.** *Top row*: **Looking at channels A and B it seems that the target source is absent from the main horn. Instead, channels E and F indicate a confusing source (of rather high flux density) in the position of the off-beam during sub-scans 2 and 3. Examining the source environment (right hand side plot) proves this to be the case.** *Middle*: **Case similar to the previous one. The difference is that here also the target source is bright enough.** *Bottom* **In this case the target source appears again very faint to be detected. There is a confusing source though in the position of the main horn during sub-scan 1 and 4.**

$$T_{\mathrm{obs}} = T_{\mathrm{II}} + \frac{T_{2-3}}{2} + \frac{T_4}{2} \qquad\qquad (2.40)$$

It is must be made clear that this discussion scratches the principles of the problem and its solution. Effort and time has been put in resolving the technical details that are disclosed only after the solution is implemented and applied on the realistic dataset.

<div align="center">

Table 2.11: **The possible confusion flavors and the corresponding resolution.**

</div>

Confusion Flavor	Description	Resolution
"clean"	In this case there is no confusing source at all	No action need be taken.
"cluster"	Independently of whether there are sources in the off positions, the source is characterized as when there is at least one source in the "ON" population.	No action is taken. There is no way to reconstruct the flux of the target source from the Effelsberg observations alone. Interferometry would be necessary.
"confused"	This is the case in which the "on" population is empty. There are however sources in any of the other populations.	At first it is attempted that measurement of the same source at a different hour angle is found. In case this fails it is attempted the reconstruction of the target source's flux with the method described earlier.

The iterative method

Ideally, the "confusion" problem could be resolved by observing the sources at different parallactic angles so that the confusing source does not lie in any of the beams. Of course this is not realistic though due to time limitations.

It can be shown analytically that an iterative application of the previously suggested method on the other hand, can gradually resolve the problem completely. The only requirement is that there is one confusing source which is not confused. That is based on the fact that if one source is not confused then its temperature can used for the reconstruction of that of a different one etc.

Problems

The previous discussion has hopefully been convincing about the efficiency of the method recommended for resolving the confusion problem. Nevertheless, it has some weak points that must at least be reported if not thoroughly discussed.

1. **Missing "confusers":** It has already been mentioned that the confusing sources are searched among the NVSS catalog. This has the disadvantage that it is disregarding sources that are not detected by the NVSS survey and they become detectable at higher frequencies. For example, sources with appropriately combination of spectral index and low frequency flux density can be completely absent from the NVSS catalog but sufficiently bright at the 4.85 GHz and so on. This is definitely a problem that could only be solved if high frequency surveys of this parts of the sky were available. In their absence, one can only make statistical assumptions. It is interesting though that the careful examination of the individual channels may give clues about the possible existence of an undetected source. An example is shown in figure 2.9.
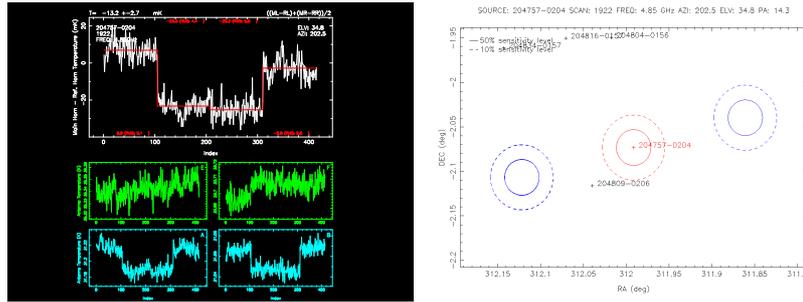
Figure 2.9: An example an "invisible" confuser. The right-hand side plot shows the NVSS environment of the target source marked as a red cross. As sen there there is no source detected by NVSS that exists in the off-positions shown in blue circles. A look in the individual channels on the left-hand side plot shows that channels A and B of the main horn (lower panels) are clearly detecting a source brighter than the target. Considering the exact configuration of the two horns and the sub-scans sequence along with the signal in channels E and F of the reference horn, it is clear that the confuser must be in the left hand blue circled region. That is on the off position of sub-scans 1 and 4.

2. **No corrections applied:** A second source of errors in the previously described method is that no opacity or gain curve corrections are applied to the brightness temperatures of the confusing sources during the resolving algorithm. This is only of the order of a few percent the most being not a major factor of error especially given that the confusing and the confused sources are at the same elevation and hence are influenced by the same atmospheric opacity.

3. **Not extremely accurate positions of beams and beams are Gaussian:** In all the above it has been assumed that the positions of the beams are precisely known and that there are no pointing offsets. Furthermore, the beam pattern is supposed to beam described by a Gaussian. With the former to be the least uncertain assumption these are introducing one more uncertainty.

2.4.2 The "cal" problem

In sub-section 2.1.1 an extensive description of the role of the noise diode has been given. Hopefully, this has made clear its importance in both controlling the stability of the receivers as well as in performing the first calibration (voltage/counts to antenna temperature). It has appeared however, that it can display peculiar behavior contrary to what has been assumed so far both within the scan (intra-scan) or over several scans (inter-scan). This can prove fatal to the measurement procedure. In brief, instead of calibrating the data on a point-by-point basis we have being using one calibration signal throughout the whole scan. The used value is of course the average calibration signal within the scan. In appendix B.2 is presented a short discussion about the inter-scan peculiarities of the diode signal and in B.2 is presented a short investigation of the possible reason for these irregularities.

3. Flux Densities

...In conclusion, data have been presented which show the existence of electromagnetic waves in the earth's atmosphere which apparently come from the direction that is fixed in space. The data obtained give for the coordinates of this direction a right ascension of 18 hours and a declination of -10 degrees...

Karl G. Jansky

Abstract

Every product of the currently presented work that will be discussed later, is based on the flux density measurements of the sample of roughly 6000 NVSS sources that are lying in the CBI fields at three frequencies. Namely, the 1.4-GHz ones coming directly from the NVSS catalog and the 4.85 and 10.45-GHz as carried out with the Effelsberg telescope. It is wise then after having described the basics of the observing system and the data reduction pipeline to go on to discuss the findings of those measurements themselves.

The first topic to be explored is the so-called "repeatability" plot that, as discussed soon, they set the level of the realistically least detectable flux density. Later, we discuss the differential source counts for each available frequency. In particular, the 1.4-GHz measurements are very illuminating since the sample is complete.

3.1   The Sample

Before proceeding with presenting and discussion of data concerning the flux density measurements, it appears essential that some clarifications are made about the sample used for each study along with an associated classification of sources. Specifically, the sources are classified on the basis of the "confusion" status.

As it has often been mentioned, the basis for the current project has been the NRAO VLA Sky Survey (NVSS,Condon et al. 1998). The NVSS survey has been carried out with a resolution of $45''$. The Effelsberg FWHM for the 4.85-GHz receiver is $145''$ (see table 2.1), roughly 3 times wider. It is sensible then to expect that many sources clearly resolved by VLA will be too close to be so by the 100-meter telescope. Additionally, taking into account the fact that the current project has been carried out with dual-beam receivers, makes clear the high probability of a having confusing (or disturbing) sources within the beam-width of any of the beams. This problem (collectively being termed as "confusion") was discussed analytically in sub-section 2.4.1.

Before any of the following computations, the data have been "de-confused". In other words, for each given observation of a single source the confusion status of the source has been identified and resolved following two simplified steps:

1. **Identification of the confusion status:** At the moment of the observation the NVSS sky around the target source is investigated. That enables the identification of the three populations described in sub-section 2.4.1.

2. **De-confusion:** The contribution of each population of confusing sources is evaluated and is accordingly applied to the measured flux density. Simultaneously, the result of the "de-confusion" is graded.
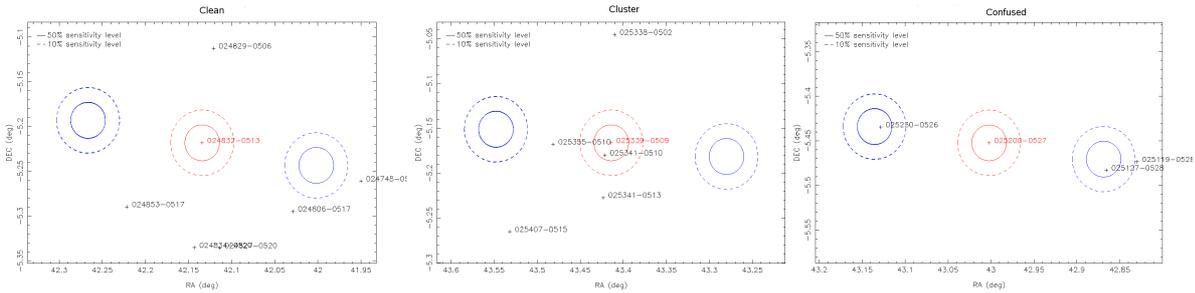
Figure 3.1:   **The classification of sources with respect to their confusion status. The target source is the one in red numbers. The circles show the 10 % and 50 % sensitivity contours for all beam positions. In blue are shown the "off" positions and in red the "on" ones. From left to right there are shown a case of a"clean", a "cluster" and a confused source.**

In reality, the previous procedure is significantly more complicated than described. However, this schematic depiction is representative enough. On the basis of their confusion status, a source can fall in one of the following classes that are also shown in figure 3.1:

1. **clean:** For these sources all three populations as described in sub-section 2.4.1 are 0. In other words these sources suffer no confusion and no resolution problems. The de-confusing algorithm leaves this class untouched.

2. **clustered:** This class is made of the sources that are resolved by the NVSS but not from the Effelsberg beam. That is, in one Effelsberg beam there exist more than one NVSS sources and hence the term "cluster" (see illustration (see figure 3.1). For these cases it is: $T_{\rm ON} \neq 0$ whereas $T_{1,4} + T_{2-3} = 0$. They are ignored by the de-confusing algorithm since there is no way to reconstruct their flux density. For these cases interferometry would be necessary.

3. **confused:** For these sources it happens that $T_{\rm ON} = 0$ and $T_{1,4} + T_{2-3} \neq 0$ and they comprise the species which the de-confusing algorithm is aiming at. The former condition means that within the Effelsberg "on" beams there are no NVSS sources additional to the target one .

In table 3.1 are compiled the facts about our sample. One notices a percentage of ∼22 % of sources that appear to be confused at the 4.85 GHz and ∼7 % that are so at the 10.45 GHz. It must be noted that all this conclusions are based solely on the NVSS catalog that is not necessarily representative of the source population at 10.45 GHz. In particular, the vast majority of sources are already faint at this band as is discussed in chapter 4 and is shown in table 3.5. More interestingly though, it is probable (although not highly so), that sources undetected by the NVSS survey appear at higher frequencies. Nothing is known about this population from the NVSS catalog alone. Interestingly though, there is method to detect such

candidates only by looking at the data from the individual channels of the Effelsberg measurements. This is however a method of very low efficiency due to the sparse probability of having a source within the area of the Effelsberg beam.

For the studies that follow, only the clean and the confused sources (after de-confusing) have been used. The cluster cases would result in a distortion of reality and therefore they have been excluded.

Table 3.1: Cases of confusion in our sample and their percentages.

Field	Sources	4.85 GHz			10.45 GHz		
		"clean"	"clustered"	"confused"	"clean"	"clustered"	"confused"
02-Hr	1624	993 (61 %)	237 (15 %)	394 (24 %)	1466 (90 %)	12 (1 %)	146 (9 %)
08-Hr	1130	744 (66 %)	170 (15 %)	216 (19 %)	1053 (93 %)	21 (2 %)	56 (5 %)
14-Hr	1681	1070 (64 %)	234 (14 %)	377 (22 %)	1522 (91 %)	21 (1 %)	138 (8 %)
20-Hr	1570	977 (62 %)	232 (15 %)	361 (23 %)	1462 (93 %)	14 (1 %)	94 (6 %)
Average		63 %	15 %	22 %	92 %	1 %	7 %

3.2 The flux densities of the "repeaters"

It has already been discussed in chapter 2 that a significant amount of observing time has been dedicated to system studies. Among them the repeatability study described in sub-section 2.3. In brief, a sample of mainly steep spectrum sources and hence unlikely to be intrinsically variable and with flux densities covering the range from a few mJy up to a few Jy, has been selected to be included in every observing session (see table 2.8). Assuming these sources to be intrinsically stable, any observed variability can be attributed to all factors of uncertainty as a whole providing a measure for the "repeatability" of a measurement.

Here are presented the results concerning the flux densities of the repeaters in the form of "S-rms" diagrams. Throughout this document they are often referred to as "repeatability" plots. As has been explained in sub-section 2.3, these diagrams summarize the realistic cumulative uncertainties in a statistical sense. Consequently, they set the flux density limit that is pragmatically reachable. All the important aspects of this work are presented immediately.

3.2.1 The repeatability plots

For the construction of the repeatability plots (figure 3.2) all the repeaters have been used at both frequencies. Additionally the calibrators (which by definition should not vary) as well as the pointing sources have been used. For each source, almost all available measurements have been used. Exception to that is cases that are extraordinary and do not really represent a "normal" observation. For example, cases of receiver failure have been excluded since they increase the noise without describing a realistic situation (data acquired with dysfunctional receiver have been dropped). The abscissa in these plots is the average flux density S and the ordinate is the rms in that.

From the discussion in sub-section 3.2.2 it is expected that the uncertainty (rms) in the determination of S is the sum of a constant term independent of the flux density and a term linearly dependent upon the flux density S of the source. Assuming that the errors are Gaussian, this is formulated as:

$$\sigma(S) = \sqrt{\sigma_0^2 + (m \cdot S)^2} \tag{3.1}$$
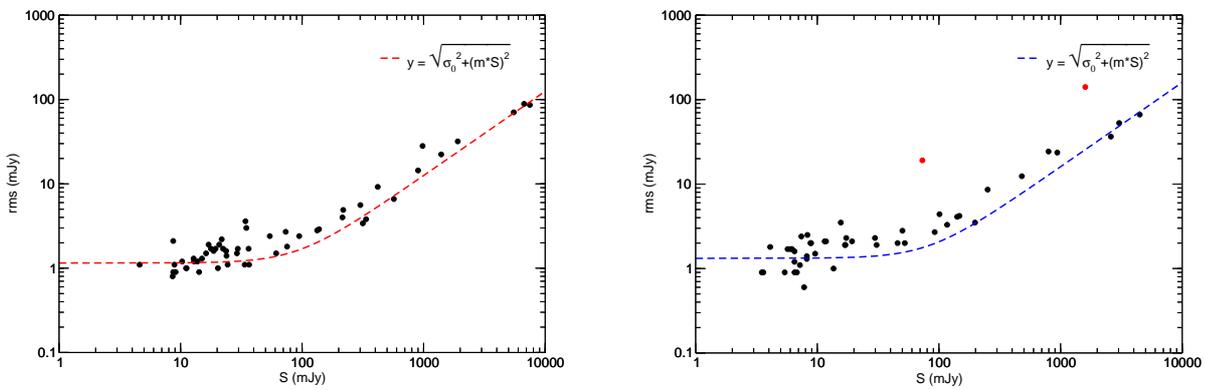
Figure 3.2:   **The "repeatability" plots. If an ideal observing system had been used under ideal conditions to observe an ideally stable source the repetition of the measurement would result in a never-changing value. Any divergence from that can be attributed to any of the possible sources of error. Nonetheless, the scatter of the flux density measurements of a given source comprise a very realistic measure of the uncertainty of a measurement in general. In the left-hand side panel is the plot for the 4.85 and the right-hand side one is that for the 10.45-GHz measurements. Note the two "outliers" in the 10.45-GHz diagram marked with red dots. The exceptionally large degree of variability is due to intrinsic factors as will be discussed in later (chapter 6). The blue and red curve are the model of the form $\sqrt{\sigma_0^2 + (m \cdot S)^2}$ fitted for high and the low frequency data respectively. The two outliers have not been used during the fit. The fitted parameters are shown in table 3.1.**

where $\sigma(S)$: the uncertainty in a measurement of flux density S

σ_0: the offset in the uncertainty equation. It is analytically discussed later

m: the modulation index due to calibration errors

As will be shown in the next sub-section this formula can be broken into well understood components of clear physical meaning. For the $S - rms$ plot at each frequency, such a function has been fitted. The fit is done over parameters σ_0 and m. The best fit results are shown in table 3.2. As can be noticed there the fit is satisfactory with the parameter determination to be of an error of less than 10 %. It is worth noting

Table 3.2: **The results of the fit of the model in equation 3.1 to the repeatability curves.**

Frequency (GHz)	σ_0	Error	m	Error
(GHz)	(mJy)	(mJy)	(%)	(%)
4.85	1.2	0.2	1.3	0.02
10.45	1.3	0.1	1.6	0.04

that in the repeatability plot for the 10.45 GHz exist two points with exceptionally high rms. This is due to intrinsic variability and will be discussed later in chapter 6.

3.2.2 Interpretation of the repeatability plots

It has already assumed in equation 3.1 that the error in a measurement can be broken into two components:

1. a flux-density-independent part σ_0^2 dominating at the low flux density regime.

2. a flux density dependent part $(m \cdot S)^2$ that becomes important at larger flux densities. In particular, when $S \gg \sigma_0/m$.

Both the constant part σ_0^2, and the flux density dependent one m^2, can be broken down to more detailed components of clear physical meaning. Understanding those components will enable us to evaluate the expected overall uncertainty and compare it with the measured one as extracted from equation 3.1.

The constant part: The constant part can be written as:

$$\sigma_0^2 = \sigma_{\text{th}}^2 + \sigma_{\text{conf}}^2 + \sigma_{\text{atm}}^2 \tag{3.2}$$

where σ_{th}: the thermal noise

σ_{conf}: the confusion error

σ_{atm}: the atmospheric emission error

and is measured in mJy. Analytically, it is:

1. **Thermal noise σ_{th}:** It is given by the "radiometer" formula and apparently sets the lower limit in the detectable flux density:

$$\sigma_{\text{th}} = \frac{K \cdot T_{\text{sys}}}{\Gamma \cdot \sqrt{\Delta\nu \cdot t}} \tag{3.3}$$

where K: Receiver dependent constant (usually $K \simeq 1 - 2$). In our case $K = \sqrt{2}$
            T_{sys}:   the system temperature
            Γ: the sensitivity of the telescope, that is the K to Jy factor
            $\Delta\nu$:   the receiver bandwidth
            t: the integration time

2. **Confusion error $\sigma_{\mathbf{conf}}$**: It describes collectively the flux density contribution from unresolved sources that happen to be included in the beam of the telescope. In fact it is a purely statistical quantity and it is described thoroughly in section 5.3.

3. **Atmospheric emission error $\sigma_{\mathbf{atm}}$**: It is the result of having imperfect atmospheric emission subtraction due to variations of the atmosphere during the scan. For bright sources apparently it is of no importance. At low flux densities though it can become significant. It is given by:

$$\sigma_{\mathrm{atm}} = \frac{\Delta\tau \cdot T_{\mathrm{atm}}}{\Gamma} \tag{3.4}$$

where $\Delta\tau$:   the change in the atmospheric opacity within one scan
            T_{atm}:   the effective atmospheric temperature i.e. emission temperature

The flux density dependent part: The flux density dependent part of equation 3.1 m^2, can be written as:

$$m^2 = m_{\mathrm{poi}}^2 + m_{\mathrm{cal}}^2 + m_{\mathrm{atm}}^2 \tag{3.5}$$

where m_{poi}:   the pointing error
            m_{cal}:   the noise diode error
            m_{atm}:   the atmospheric absorption error

And it is conveniently referred to in percentage. For its components, it is:

1. **Pointing error $m_{\mathbf{poi}}$**: This is the result of the telescope pointing uncertainties and it is:

$$m_{\mathrm{poi}} = 1 - \left(-4 \ln 2 \left(\frac{\sigma_{\mathrm{poi}}}{\psi} \right)^2 \right) \tag{3.6}$$

where ψ: the FWHM

2. **Noise diode error $m_{\mathbf{cal}}$**: This is the error introduced by the instability of the noise diode used for receiver stability control (see sub-section 2.4.2). It is given by:

$$m_{\mathrm{cal}} = \frac{\sigma_{cal}}{T_{\mathrm{cal}}} \tag{3.7}$$

where σ_{cal}:   the fluctuation in the diode signal
            T_{cal}:   the assumed temperature of the noise diode

3. **Variable atmospheric absorption error m_{atm}**: This is again related with a change in the atmospheric opacity since such a change causes both a change in the atmospheric emission but also absorption of the observed signal. This is given by:

$$m_{\text{atm}} = 1 - e^{-2 \cdot \Delta\tau \cdot AM} \tag{3.8}$$

where AM: the airmass

3.2.3 The expected and the observed uncertainties

Having identified the potential sources of error in the previous sub-section, it is challenging to investigate (i) what are the values expected for the uncertainties as computed on the basis of typical parameters for our system. (b) How are they compared to the values estimated from the fits of the repeatability plots that must by definition be realistic. For those calculations the values in table 3.4 have been used and the estimated uncertainties are summarized in table 3.3. Comparing the values as extracted from our fits (see

Table 3.3: **The expected uncertainties after having accounted for every potential source of error.**

Term	Explanation	Expected value 4.85 GHz	10.45 GHz
		(mJy)	(mJy)
Thermal noise σ_{th}	Computable from the "radiometer formula" 3.3 (see sub-section 2.2.2)	0.16	0.22
Confusion error σ_{conf}	Condon et al. 1989	0.8	0.08
Atmospheric emission error σ_{atm}	Computable from equation 3.4. For details see sub-section 2.2.3	0.92	1.3
σ_0	The flux density independent term	1.23	1.32
fitted σ_0 (see table 3.2)		**1.2**	**1.3**
		(%)	(%)
Pointing error m_{poi}	Assuming a Gaussian beam pattern and an average pointing offset of $\simeq$ 4" for 4.85 GHz and 4" for 10.45 GHz. These pointing offsets are the average over all available observing sessions (see figure 3.3).	0.21	1.01
Calibration error m_{cal}	Known from Intra-Day-Variability studies	1.5	1.5
Variable atmospheric absorption error m_{atm}	Negligible. The values here are extracted also independently from the water vapor radiometer (Roy, priv. comm.). It must be noted that the radiometer is operating at far higher frequency (22 GHz).	0.004	0.005
m	The flux density dependent term	1.51	1.81
fitted m (see table 3.2)		**1.3**	**1.6**

table 3.2) to those in table 3.3 one can say that there is a satisfactory agreement.

The overall uncertainty and the minimum detectable flux density: In the previous discussion it was found that σ_0 is 1.2 and 1.3 for 4.85 and 10.45 GHz observation respectively. It follows then that for a detection threshold of $5\,\sigma$ the realistic detection limit is:

$$S_{\mathrm{min},4.85} = 5 \cdot \sigma_0 \simeq 6\,\mathrm{mJy} \tag{3.9}$$

$$S_{\mathrm{min},10.45} = 5 \cdot \sigma_0 \simeq 6.5\,\mathrm{mJy} \tag{3.10}$$

For all the material that follows it must be kept in mind that these are the realistic values that any study hereafter should rely on. It is noteworthy mentioning that for the current project the telescope has really been operated at its theoretically limited level.

Table 3.4: **The system parameters used for the calculation of the expected uncertainties.**

Frequency (GHz)	T_{sys} (K)	K	$\Delta\nu$ (MHz)	t (s)	$\Delta\tau$	T_{atm} (K)	ψ ($''$)	Γ (K/Jy)	σ_{poi} ($''$)
4.85	27	$\sqrt{2}$	500	60	$5\cdot10^{-6}$	260	145	1.55	4
10.45	47	$\sqrt{2}$	300	240	$1\cdot10^{-5}$	260	67	1.30	4
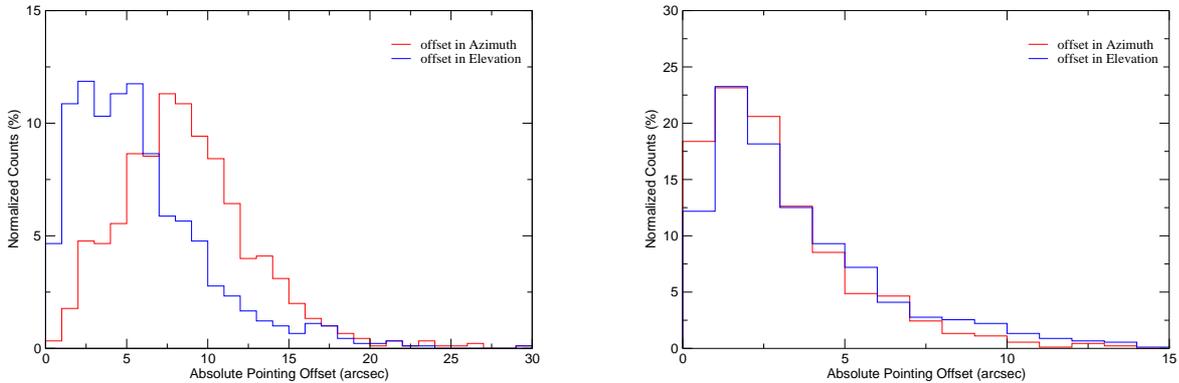
Figure 3.3:   **Here are the distribution of pointing offsets for both frequencies. The upper panel refers to 4.85 GHz and the lower to 10.45 GHz. For both plots the red contour corresponds to the azimuth coordinate and the blue to the elevation. Here are included more or less all the available measurements. Hence the result represents the behavior of the telescope over the entire 3-year span of observations. The numbers used for the calculations in table 3.3. are the average ones over both directions.**

3.3   The Effelsberg flux densities

First of all the goal of measuring the sample of the 6000 sources at 4.85 and 10.45 GHz with the 100-meter Effelsberg telescope is of course the determination of their spectral index. However, on the basis of certain assumptions which involve mainly the completeness of the utilized sample, one can draw conclusions about the spatial source distribution per flux density bin as discussed in later paragraphs. This

is of great practical interest since it provides the ground for computing the confusion limit. Of course, provided that our survey is targeted it is apparent that sources that are detectable at higher frequencies are missed. In any case though lower limits can be set. A more detailed discussion on the topic can be found in section 5.3. The exact knowledge of this quantity is essential for mainly two reasons; (a) it sets a realistic lower limit in the least detectable flux density for a given telescope at a given frequency (recall sub-section 3.2.2 and 3.2.3); (b) it provides a reliable measure for the expected flux density background in experiments studying CMB anisotropies (e.g. Taylor et al. 2001). Such experiments rely on very deep observations given the weakness of the anisotropies ($\Delta T/T \sim 10^{-6}$) making the knowledge of the noise level essential.

The differential source counts ($\log N - \log S$ plots) have been used for studying the evolutionary scenarios of radio sources and the universe it self. A excellent discussion on the topic can be found in Peterson (1997, chap. 10). Interestingly, despite the amount of effort being put in this direction, such research is still very illuminating and motivating as new surveys appear. Here, the Effelsberg flux densities are used for the construction of the $\log N - \log S$ plots that will later be used for the computation of the confusion limit in section 5.3.

Before going on to discuss the detection rates it is important to introduce the tools that are used later in this section. In particular, we start with an introduction to source counts issues since this analysis is applied afterwards for every frequency observed at Effelsberg (sub-section 3.3.1).

3.3.1 The source counts

This sub-section is intended only to draw the necessary background for the following material, it will be very brief without discussing any details.

Let (a) the all radio sources be of the same luminosity L, (b) be uniformly distributed in space with a space density n_0 in a (c) Euclidean space. Then, it can easily be shown that their *cumulative* distribution as a function of flux density, can be written as:

$$N\,(>S) = \frac{n_0}{3}\left(\frac{L}{4\,\pi\,S}\right)^{3/2} \tag{3.11}$$

where $N\,(>S)$:   the number of sources per unit solid angle with flux density larger that S
   n_0:   the constant space density of sources
   L: the luminosity of radio sources (assumed also constant for all sources)

One can immediately notice from this equation that on the bases of the three assumptions made, $N(>S)$ should appear proportional to $S^{-1.5}$. Any departure from the rule of -1.5 would imply a divergence from any of the previous assumptions. For instance, it is probable that the space density changes with distance from the observer. In particular, values steeper than -1.5 would mean that the space density increases with the distance from the observer.

Assuming that the sources have some distance-independent distribution in luminosity L the first term of the right hand part of this equation will not be influencing the dependence on S. Most often the previous equations are conveniently described by:

$$N\,(>S) = K \cdot S^{\gamma} \tag{3.12}$$

where K: constant

or, in its differential form:

$$n\,(S) = \frac{dN}{dS} = K \cdot \gamma \cdot S^{\gamma - 1} \tag{3.13}$$

The last equation describes the number of sources per unit solid angle that have been found to have flux density within the range $[S, S + dS]$ per unit flux density.

In the following paragraphs the very exponent γ is computed from the Effelsberg measurements for both observing frequencies. Under certain assumptions these equations describe the spatial distribution of sources. When convolved with a spectral index distribution can give an estimation of the expected source counts at later frequencies. Such knowledge can consequently be applied for computing the confusion limit for given antennas. This is thoroughly discussed in section 5.3.

3.3.2 Detection rates

It is to the immediate interest of the undertaken project to identify the detection rates achieved for every frequency. Indeed, assuming that this is solely due to the spectral character of the target sources then this already sets a first approximation to the sources that exhibit dangerously flat or inverted spectra for the CBI data (i.e. $\alpha \geq -0.5$ with $S \propto \nu^{\alpha}$). The current sub-section deals with exactly this problem. That is, essentially counting the sources that have been detected at each frequency.

In sub-section 4.3.1 it is explained how the detection levels have been selected for each frequency. For the 4.85-GHz measurements the detection threshold is $5\,\sigma$. For the reasons described there though the 10.45-GHz ones are characterized by a threshold set at $4\,\sigma$. The same convention will be used here.

Table 3.5 includes all the results for the currently utilized sample (61% of the total number of sources). It is important here to clarify that for the following studies only the "clean" sources have been used (see table 2.11 for the definition of the different confusion flavors). That is, sources that have no other NVSS source in neither an off nor an on position. As it is shown there, the sources are classified to the following classes:

1. Sources that have not been detected at any of the observing frequencies. They are designated with flag "00" and comprise 46% of the whole sample. For those one could claim that as long as their spectral index does not change at frequencies above 10.45 GHz they are of no harm to the CBI data. Of course one must be very careful since they still may be marginally dangerous depending on the combination of least detectable flux density and the maximum flux density tolerable by the CBI experiment.

2. Sources detected at 4.85 but not at 10.45 GHz. On the basis of similar argument as before those sources fade far before the 30 GHz. This class makes up almost 30% of the sources and is designated with the flag "10". However, the same precautions as before must be accounted for since one must still estimate the flux at the 30-GHz regime.

3. The class of sources that have been detected at both frequencies. Hence they are flagged as "11". This is the ones that are almost certain to cause contamination of higher frequency data since their radio spectrum is mostly either flat or even inverted. Such sources are the 16% of the total number and should definitely be excluded from CMB data analysis.

4. Finally, there exist a interesting and at the same time puzzling population of "01" sources that have been detected only at 10.45 GHz. It can be the result of source variability or a complex spectrum that turns inverted at higher frequencies.

Both case 1 and 2 can, at least in a statistical manner, be regarded harmless as far as the CBI experiment is concerned. However, when it comes to individual sources one must also consider the upper limits set by non-detections. This aspect is also dealt by the current project.

3.3.3 The Effelsberg 4.85-GHz flux densities

Figure 3.4 illustrates the normalized differential source counts for the 4.85-GHz Effelsberg measurements. The bin is constant in logarithmic space and is chosen to be 0.18 dex. Exact limits of the bin and the sources detected are included in table 3.6. In this study, solely the detected sources have been utilized. That leaves suspicion for sample incompleteness as is discussed in section 3.5.

Table 3.5: **The detection rates for the currently available sample of 3461 sources (61% of the total). The last four columns refer to the detection flags. The convention is X X where X is the flag for 4.85 and 10.45 respectively. X can be either 1 for detection or 0 for non detection**

Field	Sources	"Clean"	"Clean" Coverage	0 0	1 0	1 1	0 1
02-Hr	1624	920	56.7%	431 (46.8%)	238 (25.9%)	167 (18.2%)	84 (9.1%)
08-Hr	1130	694	61.4%	307 (44.2%)	252 (36.3%)	102 (14.7%)	33 (4.8%)
14-Hr	1681	932	55.4%	453 (48.6%)	264 (28.3%)	150 (16.1%)	65 (7.0%)
20-Hr	1570	915	58.3%	412 (45.0%)	268 (29.3%)	153 (16.7%)	82 (9.0%)
Total	6005	3461	57.6%	46.1%	30%	16.4%	7.5%
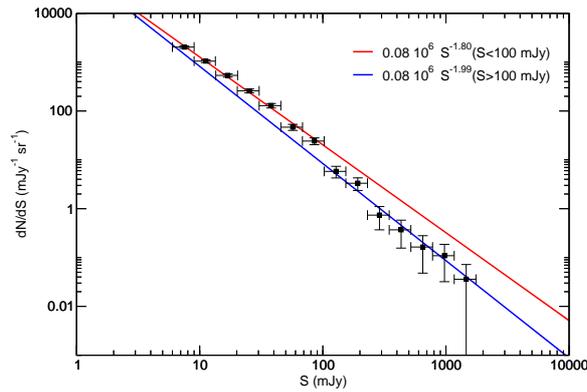
Figure 3.4: **Normalized differential source counts at 4.85 GHz as measured at Effelsberg. The normalization is done over $47 \cdot 10^{-3}$ sr.**

A function of the form 3.13 has been fitted to the data. As can readily be noticed in this figure, there exists a "break" in the slope around 100 mJy. That imposed the fitting to be done in two parts. One for the lower part of the flux densities range ($S < 100$ mJy) and one for the upper one ($S > 100$ mJy). In section 3.5 we elaborate further on the 100-mJy break. The calculated values are included in table 3.6 and result:

$$\text{for } S \leq 100\,\text{mJy:} \quad n(S) = \tfrac{dN}{dS} = 0.08\,(\pm 0.01)\cdot 10^6\cdot S^{-1.80\,(\pm 0.05)}\,\text{mJy}^{-1}\,\text{sr}^{-1} \tag{3.14}$$

$$\text{for } S \geq 100\,\text{mJy:} \quad n(S) = \tfrac{dN}{dS} = 0.08\,(\pm 0.08)\cdot 10^6\cdot S^{-1.99\,(\pm 0.17)}\,\text{mJy}^{-1}\,\text{sr}^{-1} \tag{3.15}$$

In terms of cumulative distribution then, it will be:

$$\text{for } S \leq 100\,\text{mJy:} \quad N(>S) = 0.1\,(\pm 0.01)\cdot 10^6\cdot S^{-0.80\,(\pm 0.05)}\,\text{mJy}^{-1}\,\text{sr}^{-1} \tag{3.16}$$

$$\text{for } S \geq 100\,\text{mJy:} \quad N(>S) = 0.08\,(\pm 0.08)\cdot 10^6\cdot S^{-0.99\,(\pm 0.17)}\,\text{mJy}^{-1}\,\text{sr}^{-1} \tag{3.17}$$

It must be noted that fitting the previous model is not a trivial procedure since it is very sensitive to the initial conditions. The fit has been done in the linear regime that means that a power law has been fit to the data.

Table 3.6: **The data for the study of the normalized differential source counts for the 4.85-GHz measurements.**

Bin limits (mJy)	$\langle S \rangle$ (mJy)	Counts	Bin limits (mJy)	$\langle S \rangle$ (mJy)	Counts
6.0−9.0	7.5	287	102.5−153.8	128.1	14
9.0−13.5	11.2	222	153.8−230.7	192.2	12
13.5−20.2	16.9	170	230.7−346.0	288.3	4
20.2−30.4	25.3	123	346.0−519.0	432.5	3
30.4−45.6	38.0	92	519.0−778.5	648.7	2
45.6−68.3	57.0	50	778.5−1167.7	973.1	2
68.3−102.5	85.4	39	1167.7−1751.6	1459.6	1

3.3.4 The Effelsberg 10.45-GHz flux densities

In the case of the 10.45-GHz data the followed procedure is identical to that discussed in sub-section 3.3.3. The data for the construction of the $\log N - \log S$ plot are shown in table 3.7 along with the result of the model fitting. Figure 3.5 shows the result.

Because of the small numbers of sources at the high flux density bins the fitting algorithm has been crushing. The fitting then has been done for the low flux density regime as in the case of 4.85,GHz and for collectively all the data. The parameters extracted this way imply:

$$\text{for } S \leq 100\,\text{mJy:} \quad n(S) = \tfrac{dN}{dS} = 0.06\,(\pm 0.02)\cdot 10^6\cdot S^{-1.83\,(\pm 0.10)}\,\text{mJy}^{-1}\,\text{sr}^{-1} \tag{3.18}$$

$$\text{for all } S\text{'s:} \quad n(S) = \tfrac{dN}{dS} = 0.10\,(\pm 0.02)\cdot 10^6\cdot S^{-2.08\,(\pm 0.02)}\,\text{mJy}^{-1}\,\text{sr}^{-1} \tag{3.19}$$
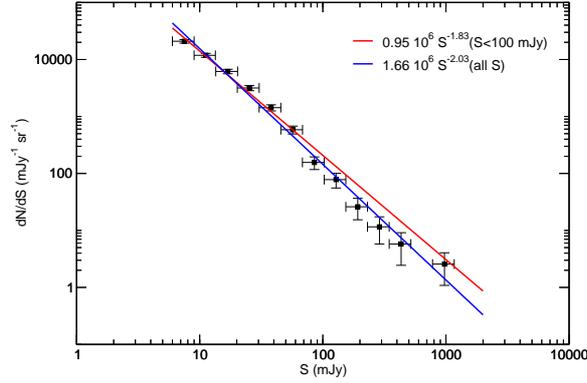
Figure 3.5: **Normalized differential source counts at 10.45 GHz as measured at Effelsberg. The normalization is done over $47 \cdot 10^{-3}$ sr.**

Deriving the cumulative distributions as in the case of 4.85-GHz observations, will give:

$$\text{for } S \leq 100 \, \text{mJy}: \quad N(> S) = 0.07 \, (\pm 0.03) \cdot 10^6 \cdot S^{-0.83 \, (\pm 0.1)} \, \text{mJy}^{-1} \, \text{sr}^{-1} \tag{3.20}$$

$$\text{for all } S\text{'s}: \quad N(> S) = 0.09 \, (\pm 0.01) \cdot 10^6 \cdot S^{-1.08 \, (\pm 0.02)} \, \text{mJy}^{-1} \, \text{sr}^{-1} \tag{3.21}$$

As it can be seen in figure 3.5 at around 100 mJy not only there is no break to steeper index (see figure

Table 3.7: **The data for the study of the normalized differential source counts for the 10.45-GHz measurements.**

Bin limits (mJy)	$\langle S \rangle$ (mJy)	Counts	Bin limits (mJy)	$\langle S \rangle$ (mJy)	Counts
6.0−9.0	7.5	188	102.5−153.8	128.1	12
9.0−13.5	11.2	160	153.8−230.7	192.2	6
13.5−20.2	16.9	125	230.7−346.0	288.3	4
20.2−30.4	25.3	96	346.0−519.0	432.5	3
30.4−45.6	38.0	65	519.0−778.5	648.7	0
45.6−68.3	57.0	40	778.5−1167.7	973.1	3
68.3−102.5	85.4	16	1167.7−1751.6	1459.6	0

3.6) but there is a step and a break to flater index. This is definetely puzzling and it is worth further investigation. Most likely though it is caused by numerical peculiarities. That is, the experience shows that these fits are extremely sensitive the initial conditions, the lowest flux density and of course the number of available measurements. Possibly here such effects are in play. It is most likely tis effect is due to small number statistics (even a few thousand measurements is a small number for such studies).

3.4 The NVSS 1.4-GHz flux densities

Contrary to the case of the Effelsberg measurements the NVSS ones are characterized by a large number of detected sources (~ 6000). That is of course due to the combination of (a) the steepness of the sources' spectra and (b) the lower flux density limit. The goodness of the fit is apparent already from the fit as shown in figure 3.6. The results of the fits are presented in table 3.8. Thus, the NVSS measurements can provide us with the most reliable differential source counts:
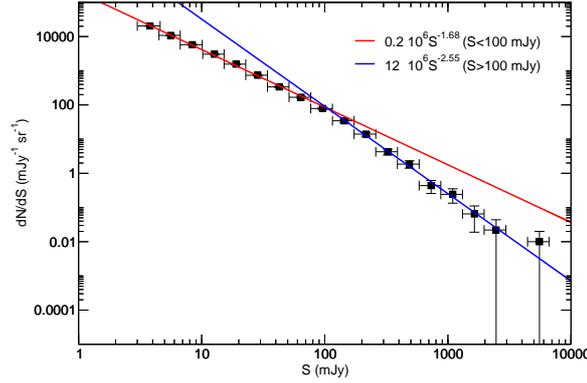
Figure 3.6: **Normalized differential source counts constructed with the NVSS measurements at 1.4 GHz of the source within the CBI fields. The normalization is also done over 0.047 sr since these sources are confined within the CBI fields. Here the point at the largest flux density has been skipped during the fit.**

$$\text{for } S \leq 100\,\text{mJy:} \quad n(S) = \tfrac{dN}{dS} = 0.20\,(\pm 0.01) \cdot 10^6 \cdot S^{-1.68\,(\pm 0.03)}\,\text{mJy}^{-1}\,\text{sr}^{-1} \quad (3.22)$$

$$\text{for } S \geq 100\,\text{mJy:} \quad n(S) = \tfrac{dN}{dS} = 12\,(\pm 4) \cdot 10^6 \cdot S^{-2.55\,(\pm 0.07)}\,\text{mJy}^{-1}\,\text{sr}^{-1} \quad (3.23)$$

Working the cumulative distributions, induces:

$$\text{for } S \leq 100\,\text{mJy:} \quad N(>S) = 0.29\,(\pm 0.02) \cdot 10^6 \cdot S^{-0.68\,(\pm 0.03)}\,\text{mJy}^{-1}\,\text{sr}^{-1} \quad (3.24)$$

$$\text{for } S \geq 100\,\text{mJy:} \quad N(>S) = 7.74\,(\pm 2.6) \cdot 10^6 \cdot S^{-1.55\,(\pm 0.2)}\,\text{mJy}^{-1}\,\text{sr}^{-1} \quad (3.25)$$

3.4.1 Comparison between NVSS and FIRST catalog

In the previous section the NVSS entries for the sources within the CBI fields were used in the determination of the source counts. The practical objective for that is the consequent estimation of the confusion limits as discussed in section 5.3.

Importantly, the NVSS measurements comprise the low frequency flux densities that are used in the estimation of the spectral indices of the target sources. This already raises the issue of the variability of the source flux density as a function of time. That is, it is likely that the source flux density at 1.4 GHz at the moment of the Effelsberg measurements is different from that at the moment of its NVSS observation. Admittedly, sources exhibiting a steep spectrum are not likely to vary significantly and they make up the

Table 3.8: **The data for the study of the normalized differential source counts for the NVSS 1.4-GHz measurements of the CBI-Effelsberg sample of 6000 source.**

Bin limits (mJy)	$\langle S \rangle$ (mJy)	Counts	Bin limits (mJy)	$\langle S \rangle$ (mJy)	Counts
3.0−4.5	3.8	1438	115.3−173.0	144.2	93
4.5−6.8	5.6	1143	173.0−259.5	216.2	57
6.8−10.1	8.4	917	259.5−389.2	324.4	26
10.1−15.2	12.7	726	389.2−583.9	486.5	17
15.2−22.8	19.0	557	583.9−875.8	729.8	6
22.8−34.2	28.5	395	875.8−1313.7	1094.7	5
34.2−51.3	42.7	270	1313.7−1970.5	1642.1	2
51.3−76.9	64.1	202	1970.5−2955.8	2463.2	1
76.9−115.3	96.1	142	2955.8−4433.7	3694.7	0
			4433.7−6650.5	5542.1	1

majority of the sources (more than 60%). It is nevertheless essential that at least a statistical statement is made concerning the variability issue.

For this reason, here the NVSS catalog entries are compared to the FIRST catalog (White et al., 1997) ones. Given the time separation between the two surveys, this comparison is expected to determine the long term variability of the 1.4-GHz flux density variability of the target sources. In fact, one could argue further and distinguish between long and short time scale variability. That is, the suggested correlation traces the variability over time scale of the order of the separation between the two catalogs. No information though is provided for the short time scale behavior of the sources. That is provided at least oartly by the "repeatability" plots.

In figure 3.7 are shown the NVSS ($x-$axis) and the FIRST ($y-$axis) integrated flux densities for most of the sources in the CBI fields that has not been resolved by the FIRST survey (since not all the area covered by CBI is covered by FIRST catalog). It is obvious that those measurements are not identical. As is shown there there is a systematic offset between the two flux densities. In the lower plot in that illustration there has been a Gaussian fitted. Its center μ and its FWHM σ in mJy, are:

$$\mu = 1.04 \pm 0.02 \text{ mJy} \tag{3.26}$$

$$\sigma = 1.30 \pm 0.02 \text{ mJy} \tag{3.27}$$

Generally speaking, there are three obvious reasons for the NVSS integrated flux density of a source to differ from its FIRST one:

1. **Source variability**: That would result variations in the flux density of sources in a random fashion. That is, as many source would appear weaker as brighter. In a plot of the difference between the flux measured by NVSS and that by FIRST survey that would be imprinted as a scatter around zero.

2. **Diffuse emission**: Due to the higher resolution characterizing the FIRST catalog ($5''$) with respect to that of the NVSS ($45''$) the latter detects more diffuse emission. In a plot of difference $S_{\mathrm{NVSS}} - S_{\mathrm{FIRST}}$ that would cause a bias towards positive values due to the systematic loss of diffuse emission in the FIRST survey.

3. **Confusion**. This is obviously the case given the larger beam with which the NVSS survey has been conducted. This would have the same result as the previous effect causing a bias towards the NVSS.

Concerning the first point, the intrinsic source variability is expected to be more prominent for sources of flatter spectral index. Besides, as already mentioned it cannot appear to be systematic. Hence, it is not contributing to the ~ 1 mJy difference that is observed. Subsequently, the only way for justifying this offset is the combination of second and the third effect.

Under these circumstances, it is sensible to decompose the integrated flux density from a sky region of the size of the NVSS beam $S_{\mathrm{NVSS}}^{\mathrm{int}}$, which therefore is regarded as a point source, into the following constituents:

$$S_{\mathrm{NVSS}}^{\mathrm{int}} = \sum S_{\mathrm{FIRST}}^{\mathrm{int}} + D + C \tag{3.28}$$

where $S_{\mathrm{FIRST}}^{\mathrm{int}}$:   is the integrated flux density of the point sources detected by the FIRST survey convolved by the NVSS beam

           D: is the flux density due to diffuse emission collectively for the whole beam area that has been resolved out by FIRST

           C: the flux density due to confusion

As an example, in figure 3.8 is shown a FIRST map of a NVSS point source. Visually one can readily distinguish three sources plus elements of diffuse emission. Since the area covered by the three sources is nearly covered by the NVSS beam, the NVSS integrated flux density should be made of the integrated flux density of the point-like "FIRST" sources (term $\sum S_{\mathrm{FIRST}}^{\mathrm{int}}$) plus the flux density attributed to the elements of diffuse emission (term D). Moreover, there must be some part of flux density coming from confusion (term C). This cannot really be distinguished by the other two terms and it is only statistically constant.
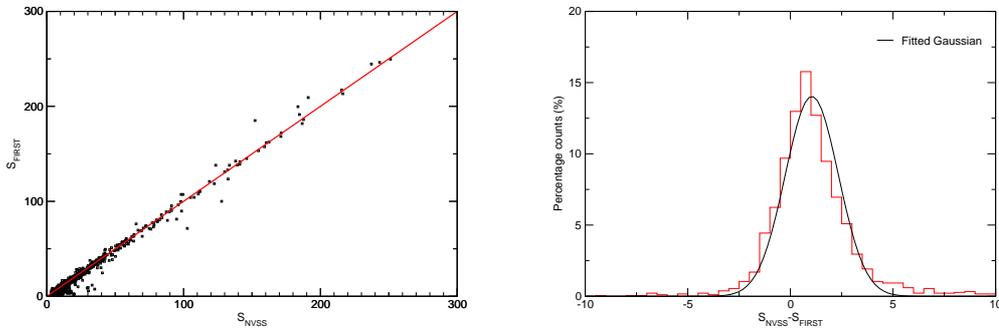
Figure 3.7: **Left: Comparison of the $S_{1.4}$ as extracted from NVSS and FIRST catalog for the sources in the CBI fields. The red line is described by $y = x$. For convenience the only up to 100 mJy is plotted. It is immediately apparent that the measurements are far from being identical. Right: In this plot the histogram of $S_{\mathrm{NVSS}} - S_{\mathrm{FIRST}}$ is shown. The fitted Gaussian is centered at 1.04 mJy and has a σ of 1.3 mJy. Hence there is a bias towards the NVSS which could not be explained by source variability.**

If one could estimate D and C independently then it would be easy to test this interpretation. Concerning D, such a test would be to compare the NVSS integrated flux density with the peak one since the difference:

$$S_{\mathrm{NVSS}}^{\mathrm{int}} - S_{\mathrm{NVSS}}^{\mathrm{peak}} \tag{3.29}$$

comprises an independent measure of the diffuse part D. The term C can be estimated from the $\log N - \log S$ plots and the beam size of the NVSS survey (see section 5.3).
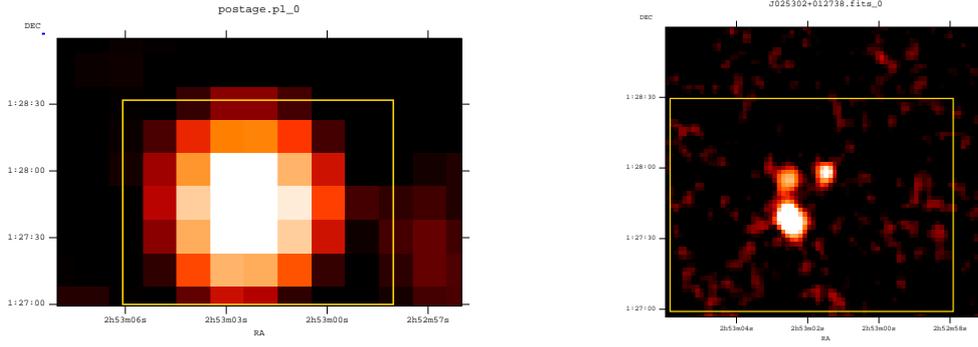
Figure 3.8: **A region of the radio sky as mapped by the NVSS (left) and the FIRST catalog (right). The yellow frames indicate the two identical regions of the sky. It is obvious that the source is far from being point-like as indicated by NVSS. The NVSS image has an integrated flux density of 22 mJy. The FIRST one has a sum of integrated flux densities for the three sources of 20.1 mJy.**

3.5 Discussion

In the previous paragraphs dealing with the differential source counts the flux density break of 100 mJy has been used to divide the source count into two different flux density regions. As it shown in Condon (1984); Peterson (1997) around this level the slope of the source counts changes significantly. Specifically it becomes steeper. For a constant co-moving density it is not expected that such a change occurs. This break then clearly seen in figure 3.6 indicates that the population of radio sources is evolving with time. However, as it has been discussed throughout this manuscript the previously presebted fits are done

Table 3.9: **The Collection of the normalized cumulative source counts. All the rest is extracted from the source counts plots.**

Survey	Frequency (GHz)	$N(> S)$ $(10^6 \, \mathrm{mJy}^{-1} \, \mathrm{sr}^{-1})$			
NVSS	1.4	for $S \leq 100$ mJy:	$0.29 \cdot 10^6 \cdot S^{-0.68}$	for $S \geq 100$ mJy:	$7.74 \cdot 10^6 \cdot S^{-1.55}$
Effelsberg-CBI	4.85	for $S \leq 100$ mJy:	$0.1 \cdot 10^6 \cdot S^{-0.80}$	for $S \geq 100$ mJy:	$0.08 \cdot 10^6 \cdot S^{-0.99}$
Effelsberg-CBI	10.45	for $S \leq 100$ mJy:	$0.07 \cdot 10^6 \cdot S^{-0.83}$	for all S's:	$0.09 \cdot 10^6 \cdot S^{-1.08}$

in alogarithmic space. Therefore, they are very sensititve to the conditions that are set. For example, the lowest acceptable flux desnity is one of them. To conlude then one must mention that these values must be taken rather indicative than literay. Besides, it is important to keep in mind that as far as the 4.85 and th 10.45-GHz measurements are concerned, the survey is targeted. There may be hence sources that exist but are undetected.

4. Spectral Indices

One picture is worth one thousand words;
one spectral energy distribution study is worth one thousand
pictures.

<div align="right">Anonymous</div>

Abstract

The motivation for this work has already been discussed in the introductory chapter. In brief, we aim the identification of sources that at the frequency of 30 GHz they have flux density of more than 1 mJy. This calculations are done on the basis of their spectral index as computed from the flux density at 1.4, 4.85 and 10.45 GHz and the low frequency flux density. They comprise the population that may potentially contaminate the CMBR data as observed by the Cosmic Background Imager. Hence they should be excluded during CMBR data analysis.

As will be shown in section 4.1 the spectral index of a radio source reveals many of its secrets among which the mechanism responsible for the emission we detect. Hence, there is a fundamental interest in exploring the spectral index at different bands especially in the light of such an extended sample of sources.

4.1 Spectra of radio sources

From the very early days of the exploration of the radio sky it has become clear that there exist two distinct classes of radio sources: *galactic*, being in the Milky Way and *extragalactic* ones, uniformly distributed in the celestial sphere. The second class comprises chiefly the class of Active Galactic Nuclei (AGN).

The nature of both has been investigated on the basis of their spectral characteristics as extracted by multi-frequency observations (see figure 4.1). Those revealed a dual classification as well. (a) *Thermal* sources. In this category are the sources emitting as *black body* and those powered by *free-free* emission. In the radio regime the flux density of the former is an increasing function of frequency. For the later it rises and then is constant with frequency. (b) *Non-thermal* sources with their flux density to be rather decreasing with frequency. These sources are generally brighter.

The brightest sources of radio have been found among the extragalactic ones. This very fact sets a meaningful connection between the two classifications in the sense that most of the known extragalactic sources are non-thermal and hence brighter and therefore farther detectable.

The connection between the nature of the radio sources and their spectral characteristics is easily understood with the following example. According to the Rayleigh-Jeans approximation in the radio
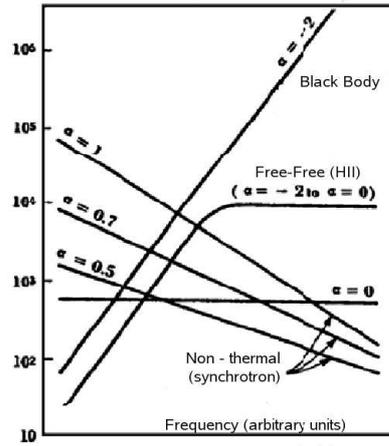
Figure 4.1:   **The classification of the emission mechanisms.**

regime, the flux density of a radio source is given by:

$$S = \frac{2\,k}{\lambda^2} \int \int T\,d\Omega \tag{4.1}$$

where K: Boltzman's constant
           T: equivalent black body temperature
        $d\,\Omega$:   Solid angle element

Assuming that the temperature of the source is constant over the source while integrating over the whole source and using terms of frequency rather than wavelength, one can write:

$$S \propto \nu^2\,T\,\Omega_s \tag{4.2}$$

Provided that the temperature of the source is independent of the observing frequency, which happens to be the case of black body radiation, then the flux density appears proportional to the second power of frequency characteristic of the black body radiation.

On the other hand, the spectra of extragalactic radio sources cannot be described in terms of radiation from a black body at a single temperature. Neither can they be described as a composite over a small range in temperature. Interestingly, they can often be described, at least to first order, by a recipe as simple as:

$$S \propto \nu^\alpha \tag{4.3}$$

where S: the flux density
        ν: the frequency
        α: the spectral index

The physical process at work in the case of non-thermal sources is the incoherent synchrotron emission that undergoes self-absorption. The fundamentals of this idea are described immediately. In fact the formula 4.3 is also valid for black body and free-free emission but with different index. One can say that the spectral index is indicative of the emission process at work.

4.2   Synchrotron and synchrotron self-absorption mechanism

Primarily, due to the broad-band character of the synchrotron mechanism and the similarities of the extragalactic radio sources spectra to those of synchrotron sources, it was suggested that the mechanism at

work in the case of AGNs is the *incoherent synchrotron radiation* or *magnetic bremsstrahlung* (see Alfvén and Herlofson, 1950; Kiepenheuer, 1950; Ginzburg and Syrovatskii, 1965). An extensive description of the synchrotron mechanism can be found in Longair 1994 or Rybicki and Lightman 1986.

Synchrotron radiation is generated when relativistic electrons are accelerated in magnetic field. The radiation from a single particle is confined within a cone of very small opening angle that depends on its energy. In fact, the spectrum of such a relativistic electron is quasi-continuous made of many closely-spaced lines and is described by a power law. It can be shown that the power radiated by a single electron is proportional to the square of its energy and it is qualitatively illustrated in figure 4.2. Hence,
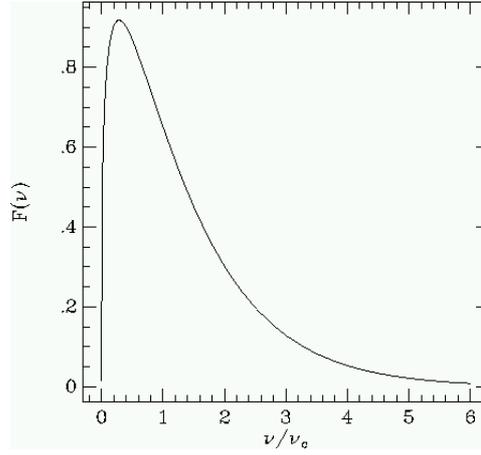
Figure 4.2: The spectrum emitted by a single relativistic electron according to the synchrotron mechanism.

in the case of an assemblage of electrons the resulted spectrum will depend on their energy distribution. Specifically, it will be described by the convolution of the electron energy distribution with the spectrum of a single particle. Assuming a homogenous source, a constant magnetic field and a distribution of electron densities of the form:

$$N(E)\, dE = N_0\, E^{-\gamma}\, dE \qquad (4.4)$$

where γ: electron energy spectrum index

one can work out the resulted spectrum to be of the form of that in equation 4.3 with the spectral index α, being:

$$\alpha = \frac{1-\gamma}{2} \qquad (4.5)$$

So far, it has implicitly been assumed that each emitted photon reaches the observer. This though, is far from being true. In reality, as a photon propagates through the plasma outwards it is possible that it will scatter off one of the electrons responsible for the synchrotron emission. This process is termed as *synchrotron self-absorption*. In case the photon happens to experience such encounters often (before escaping the emitting region) the observer detects only the emission from a thin layer near the surface of the source. The exact spectrum that will then be observed depends on the optical depth of the synchrotron radiation which of course is a function of the self-absorption cross section. A qualitative sketch of the situation is illustrated in figure 4.3. It can be shown that the optical depth is given by:

$$\tau \propto \nu^{(\gamma+4)/2} \qquad (4.6)$$

 At low frequencies the optical depth is large. That allows strong synchrotron self-absorption to take place, resulting in:

$$S \propto \nu^{5/2} \qquad (4.7)$$
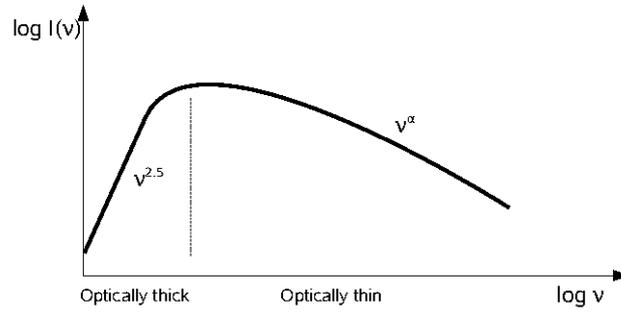
Figure 4.3:   **The expected spectrum of an ensemble of electrons with a power law energy distribution described by equation 4.4.**

In contrast, at high frequencies the optical depth is small. As a consequence the flux density will be:

$$S \propto \nu^{\alpha} \text{ (with } \alpha \leq 0) \tag{4.8}$$

Apart from the low frequency cut-off which is attributed to the self-absorption effect, the synchrotron spectrum exhibits a second cut-off at its high frequency regime. That makes the slope of the optically thin part even steeper than $S \propto \nu^{\alpha}$ (i.s. α becomes more negative). This is interpreted in terms of the combination of the maximum energy that the electrons can gain during their acceleration and the pace at which they loose their energy (see Rees 1967). Concerning the former, according to *Fermi acceleration* (the standard particle acceleration mechanisms) there exists an upper limit in the electron energy. That corresponds to their gyro-radius being larger that the accelerating region. On the other hand, the electrons loose their energy at a pace that is proportional to their energy squared. That is:

$$\frac{d E}{d t} \propto E^2 \tag{4.9}$$

The combination of those two effects results in the fast still smooth high-frequency cutoff as shown in figure 4.4. At typical spectrum interpreted in terms of synchrotron self-absorption mechanism is shown in plot 4.4.

Definitely, the spectra of AGN are not as canonical as that. In reality there exists a variety of spectra shapes. However, it is strongly believed nowadays that in all cases the observed spectrum in the radio band is the composition of several synchrotron self-absorption components. To put it differently, any given spectrum shape can be decomposed to an appropriate number of synchrotron self-absorbed components.

From all the above then it is apparent that the importance of spectral indices studies reaches beyond the practical application of identifying the population that may threat the accuracy of the CMBR experiments. Such studies are important on their own sake since they are immediately related to the physical processes occurring at the sources. Moreover, they comprise the starting point for predicting the high frequency populations as will be discussed later in chapter 5.

Sources powered by the synchrotron self absorbed mechanism are also expected to exhibit very high degree of linear polarization (10-70 %). This discussion is presented in section 7.1.

4.3   Spectral indices of the 6000 sources

In the current section we present the distribution of the spectral indices $\alpha_{1.4}^{4.85}$ and $\alpha_{4.85}^{10.45}$ as determined from our measurements. In terms of the initiatives of the current project, this is the most crucial part of
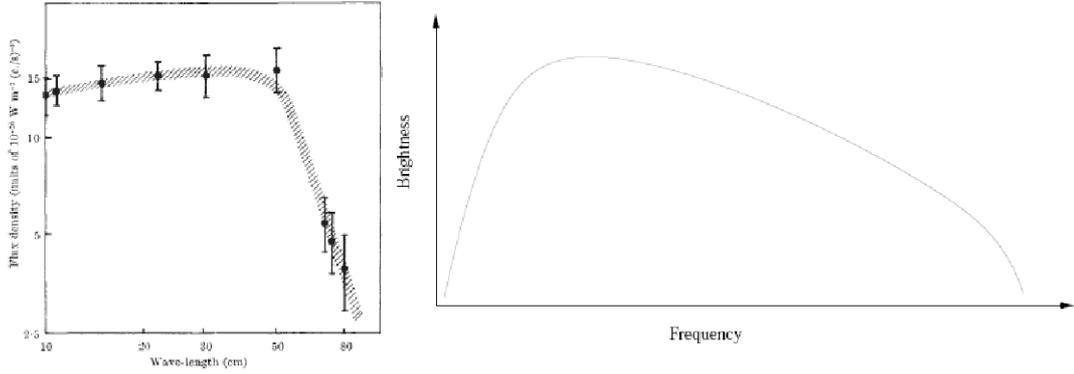
Figure 4.4: **Left: The spectrum of PKS 1934-63 interpreted by the synchrotron self-absorption model. Note that the abscissa is wavelength. In terms of frequency the optically thick exhibits a spectral index of -2.6 and the optically thin an index 0.15 (Bolton et al., 1963). Right: The synchrotron self-absorbed spectrum with its high frequency cutoff.**

the study since it will pinpoint the sources that may prove harmful to any CMBR experiment.

4.3.1 The distribution of spectral indices: $\alpha_{1.4}^{4.85}$, $\alpha_{4.85}^{10.45}$ and $\alpha_{1.4}^{10.45}$

After the short introduction that has been necessary for setting a ground for understanding the statistical characteristics of spectral index of our sample, it is time we draw the attention on the statistics itself. It is important to remember that the adopted definition of spectral index α hereafter, is:

$$S \propto \nu^{\alpha} \tag{4.10}$$

It is expected that the three possible spectral indices distributions ($\alpha_{1.4}^{4.85}$, $\alpha_{4.85}^{10.45}$ and $\alpha_{1.4}^{10.45}$) differ mainly due to the combination of frequency bands they refer to and the emission mechanisms (and hence spectral energy distributions hereafter SED) assumed for extragalactic radio sources. Second order effects such as relativistic beaming etc can also affect the observed distributions as will be discussed later in this section.

All the distributions discussed here are skewed. Consequently, they cannot be exactly represented by a Gaussian function. Nevertheless, the latter provides a measure for the mean of the distribution as well as its broadness. That is, the Gaussian function is a convenient tool for determining the peak of the distribution. For every distribution then such a function has been fitted. The fitting algorithm applies an implementation of the nonlinear least-squares (NLLS) Marquardt-Levenberg algorithm (Marquardt, 1963). In addition, the average and the median spectral indices have calculated. In fact, the median is very a representative tool since in distributions of that sort it is often the case that many points appear in the tails of the distributions.

In order to detect every possible factor of bias all studies have been carried out separately for each field as well as cumulatively for all four fields. In absence of serious bias factors the resulted values should appear similar among all those distributions. On the other hand, in case for example a field has suffered from atmospheric effects that should be imprinted in the results of those studies.

Concerning the sample that has been used, one should mention the following. Among all the sources observed only those that do not suffer by confusion have been utilized here. That is, sources that either do not suffer from confusion or have been "de-confused" as is described in sub-section 2.4.1. The 4.85-GHz detections are restricted by SNR $\geq 5\sigma$ (SNR: Signal-to-Noise Ratio). On the other hand, for a measurement at 10.45 GHz, detection is regarded a measurement with SNR $\geq 4\sigma$. This decision has been made on the basis of the combination of the following facts:

1. High frequency observations (10.45 GHz) are far more sensitive to the atmospheric conditions that low frequency ones. That often induces a large ΔT. This fact in combination with the error definition[1] often leads to the situation that a visually clear detection is mathematically rejected.

2. Moreover, the discussed measurements are also meant to identify the sources with not steep enough spectrum to be left untouched in analyses of CMB data. In this context it is preferred to allow the spurious high frequency detections rather than fake non-detections. The latter will flag sources as harmless when they can clearly be potential contaminants.

Given the fact that the atmospheric influence is tremendously significant for the weaker among the targets, it follows that a larger SNR threshold would underestimate the counts at this flux density regime. Contrary to that, the decided convention slightly favors them. It is interesting to investigate the significance of this preference.

The distribution of $\alpha_{1.4}^{4.85}$

To begin with, in figure 4.5 is shown the distribution of the spectral indices between 1.4 and 4.85 GHz. The ordinate is the counts normalized by the size of the sample. The bins are set to 0.1. A fitted Gaussian gave a mean spectral index of -0.66 $\pm$ 0.01 (1.8 %). The average appears to be at -0.52 $\pm$ 0.02 (0.3 %) whereas the median is -0.66. In that figure there exist sources that contribute to the very positive part
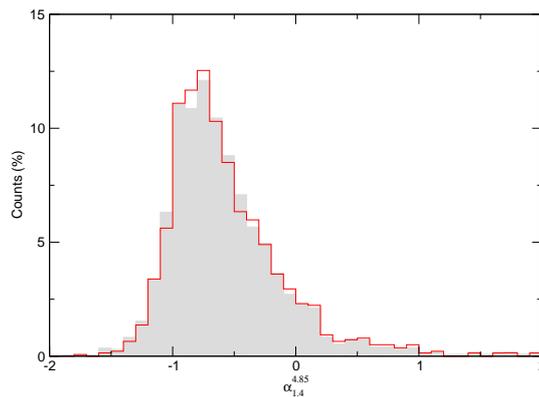
Figure 4.5: **The normalized distribution of the spectral index between 1.4 and 4.85 GHz ($\alpha_{1.4}^{4.85}$ with $S \propto \nu^{\alpha}$) collectively for all four fields. The grey area is characterized by detection limit $5\,\sigma$ whereas the red line by $7\,\sigma$. The ordinate is the counts normalized by the total number of detected sources. Negligible is the presence of a small number of sources with spectral indices larger than 1. This should only be attributed to some expected noise. Fitting a Gaussian to the $5\,\sigma$ sample resulted a mean spectral index -0.66 $\pm$ 0.01. The average calculated for the same dataset is -0.58 $\pm$ 0.01. The median value is -0.67. All the calculated values are included in table 4.1. The median spectral index in the case of the $7\,\sigma$ sample is 0.67 $\pm$ 0.002.**

of the distribution. This is may partly be true but also may be due to the inevitable remaining noise in the calculated spectral indices. At this point what is most important is the statistical significance of the distribution.

Although the distribution in figure 4.5 already summarizes all the important statistics concerning the "low-frequency" spectral indices, it is worth examining the same distribution not over the whole sample

---
[1]The error in a single measurement is the maximum between the thermal noise and the difference between $T_I 0$ and $T_{II} 0$.
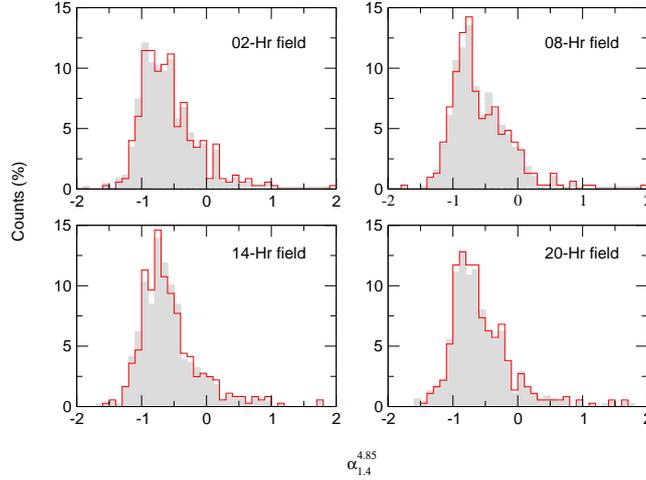
Figure 4.6: **The normalized distribution of the spectral index $\alpha_{1.4}^{4.85}$ for each field separately. The grey area corresponds to the $5\,\sigma$ detections while the red line to $7\,\sigma$ ones. The calculated values can be found in table 4.1.**

as one but rather separately for each one of the four independent sky region that have been studied. This will immediately clarify whether there are incidents of fatal biases such as weather effects. The idea is that assuming that there is a bias from a field-dependent factor, it will result distributions significantly different from one field to another. In those terms, figure 4.6 summarizes the findings for each target field separately. It is clear already from a first glance that the results are similar without any significant difference.

It is worth examining whether a detection threshold higher than $5\,\sigma$ would have any important influence on the resulted distributions. In figure 4.5 is also presented the distribution based on detections with SNR $\geq 7\,\sigma$. In this case the average appears to be -0.56 $\pm$ 0.01 and the median -0.67 $\pm$ 0.002. The slightly different average is of no surprise since apparently setting the threshold higher will abandon some "outliers". It is noteworthy though that the two values agree within the errors. This is an indication that the $5\,\sigma$ threshold is already safe enough.

The distribution of $\alpha_{4.85}^{10.45}$

Let us now repeat the operations of the previous paragraph for the high frequency spectral index, namely $\alpha_{4.85}^{10.45}$. Before presenting the results though it is important to recall that as has already been explained the 10.45-GHz detections are confined above the $4\,\sigma$ level. However, consistency checks similar to those in the previous paragraph will be resented.

Table 4.2 summarizes all the important findings in this band. The first important point to be mentioned is satisfactory agreement of the values extracted from the $4\,\sigma$ detection level sample and that of $7\,\sigma$. It is shown in table 4.2 that within the bounds of errors the average, the mean as calculated by fitting a Gaussian function and the median are essentially identical. That proves the point made earlier that the $4\,\sigma$ sample is already very reliable. In reality, the definition of errors as described in paragraph 2.2.2 is very pessimistic for the high frequency observations.

From the comparison of the low frequency spectral index one can immediately see that statistically the spectra become steeper.

Table 4.1: The distribution of $\alpha_{1.4}^{4.85}$. Here, both the "un-confused" and the "de-confused" sources are included. The detection threshold has been set to $5\,\sigma$. The results for $7\,\sigma$ detections are included in the last line.

Sample	Average index	Mean Index	Median Index
		(as derived from the Gaussian fit)	
02-hr field	$-0.59 \pm 0.02\ (3.5\,\%)$	$-0.66 \pm 0.02\ (2.9\,\%)$	-0.66 ± 0.002
08-hr field	$-0.59 \pm 0.02\ (3.8\,\%)$	$-0.65 \pm 0.02\ (3.5\,\%)$	-0.68 ± 0.002
14-hr field	$-0.58 \pm 0.02\ (4.2\,\%)$	$-0.66 \pm 0.01\ (2.1\,\%)$	-0.65 ± 0.001
20-hr field	$-0.57 \pm 0.02\ (4.0\,\%)$	$-0.67 \pm 0.02\ (2.7\,\%)$	-0.68 ± 0.001
Average	$-0.58 \pm 0.01\ (1.9\,\%)$	$-0.66 \pm 0.01\ (1.4\,\%)$	-0.67 ± 0.001
All sources	$-0.58 \pm 0.01\ (1.9\,\%)$	$-0.66 \pm 0.01\ (2.1\,\%)$	-0.67 ± 0.002
All sources[†]	$-0.56 \pm 0.01\ (2.3\,\%)$	$-0.66 \pm 0.02\ (2.4\,\%)$	-0.67 ± 0.002

[†] $7\,\sigma$ detection limit.
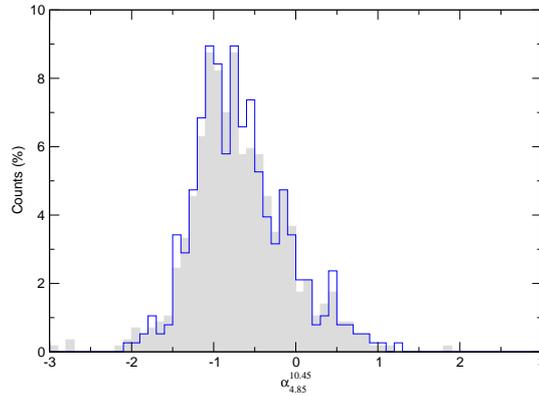
Figure 4.7: The normalized distribution of the high frequency spectral index, $\alpha_{4.85}^{10.45}$. The blue line corresponds to the $7\,\sigma$ detection limit and the grey area to the $4\,\sigma$ ones. The median spectral index as extracted from the latter sample, is -0.75 $\pm$ 0.001. It is noteworthy that there is no apparently significant difference between the distributions of the two samples. The extracted values are included in table 4.2.

Figure 4.8: The normalized distribution of the spectral index $\alpha_{4.85}^{10.45}$ plotted for each field individually. The grey area corresponds to a threshold at $4\,\sigma$ and the blue contour to $7\,\sigma$.
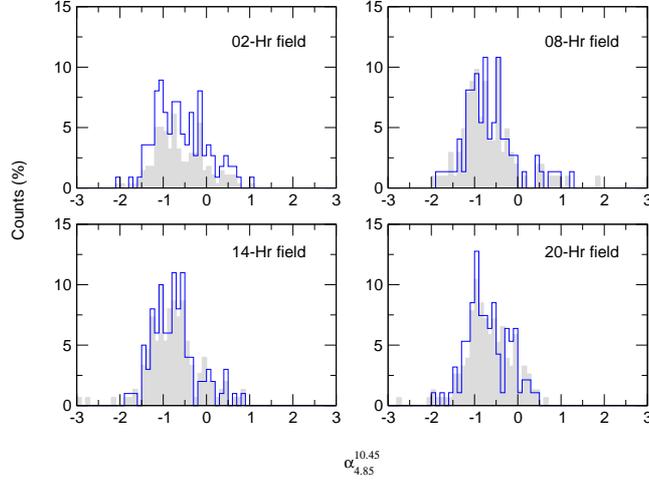
Table 4.2: The distribution of $\alpha_{4.85}^{10.45}$. Here, both the "un-confused" and the "de-confused" sources are included. The detection threshold has been set to $5\,\sigma$ for the 4.85-GHz measurements and $4\,\sigma$ for the 10.45-GHz ones. The results for $7\,\sigma$ detections are included in the last line.

Sample	Average index	Mean Index	Median Index
		(as derived from the Gaussian fit)	
02-hr field	$-0.62 \pm 0.05\,(7.3\,\%)$	$-0.67 \pm 0.05\,(6.8\,\%)$	-0.74 ± 0.01
08-hr field	$-0.68 \pm 0.08\,(12.0\,\%)$	$-0.78 \pm 0.04\,(4.5\,\%)$	-0.77 ± 0.04
14-hr field	$-0.75 \pm 0.05\,(6.5\,\%)$	$-0.79 \pm 0.03\,(3.4\,\%)$	-0.78 ± 0.03
20-hr field	$-0.68 \pm 0.05\,(6.6\,\%)$	$-0.66 \pm 0.03\,(4.2\,\%)$	-0.73 ± 0.01
Average	$-0.68 \pm 0.03\,(4.2\,\%)$	$-0.72 \pm 0.05\,(6.8\,\%)$	-0.76 ± 0.01
All sources	$-0.68 \pm 0.03\,(3.8\,\%)$	$-0.72 \pm 0.02\,(2.7\,\%)$	-0.75 ± 0.001
All sources[†]	$-0.68 \pm 0.03\,(4.4\,\%)$	$-0.73 \pm 0.02\,(3.0\,\%)$	-0.75 ± 0.001

[†] $7\,\sigma$ detection limit.

The distribution of three-point least squares fit α
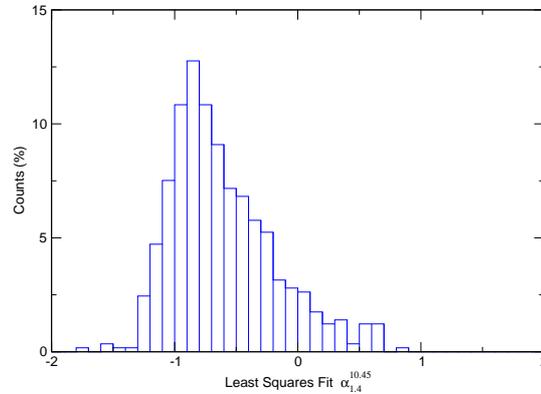
Figure 4.9: **The normalized distribution of the spectral index $\alpha_{1.4}^{10.45}$ derived from the least square fit.**
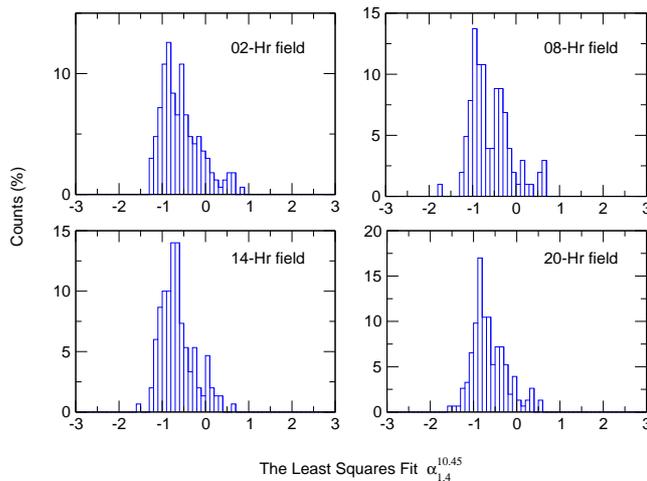
Figure 4.10:   **The normalized distribution of the spectral index $\alpha_{1.4}^{10.45}$ derived from the least square fit presented for each field separately.**

Despite the fact that the spectral index between 1.4 and 10.45 GHz covers a rather extended frequency range, it is interesting to examine its distribution and compare that with the low and high frequency spectral indices presented earlier. In fact, this is among the most important results since it will be later used for estimating the flux densities and hence the source counts at 30 GHz. From that, the confusion limit at this band will be derived.

For reasons that have already been discussed earlier, the detection limit for 4.85 and 10.45 GHz has been set to $5\,\sigma$ for the former and $4\,\sigma$ for the latter. The fitted function has been the one in equation 4.10. The fitting algorithm was again the Levenberk- Marqat and the data points are subject to natural weighting (i.e. $1/\sigma^2$).

In figure 4.9 we present that distribution for all the sources detected at both 4.85 and 10.45 GHz. Figure 4.10 includes the same but for each field separately. In table 4.3 are shown all the values extracted from those plots. It is impressive to notice that the median for the collective distribution is identical to the canonical value of -0.7. It is also worth noting that within the bounds of errors, the individual fields give similar values for the median and the mean.

Table 4.3: **The distribution of the three-point Least Squares Fit α.**

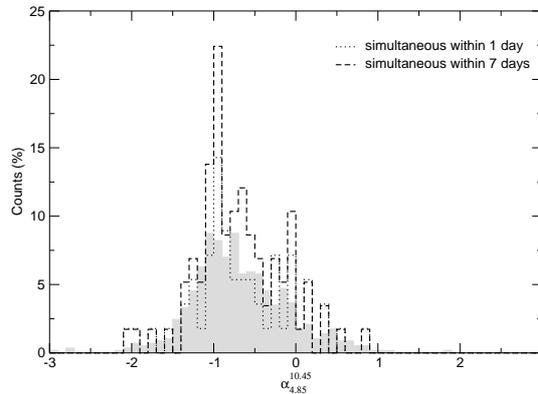| Sample	Average index	Mean Index	Median Index
		(as derived from the Gaussian fit)	
02-hr field	$-0.57 \pm 0.04\,(6.2\,\%)$	$-0.66 \pm 0.02\,(3.3\,\%)$	-0.64 ± 0.01
08-hr field	$-0.58 \pm 0.05\,(7.9\,\%)$	$-0.66 \pm 0.04\,(5.2\,\%)$	-0.72 ± 0.01
14-hr field	$-0.65 \pm 0.03\,(4.9\,\%)$	$-0.71 \pm 0.02\,(2.1\,\%)$	-0.71 ± 0.004
20-hr field	$-0.64 \pm 0.03\,(5.2\,\%)$	$-0.69 \pm 0.02\,(2.9\,\%)$	-0.72 ± 0.01
All sources	$-0.61 \pm 0.02\,(3.0\,\%)$	$-0.69 \pm 0.02\,(2.7\,\%)$	-0.70 ± 0.001

Simultaneous spectral indices

Figure 4.11: **The normalized distribution of the spectral index $\alpha_{4.85}^{10.45}$ with different temporal offsets between the 4.85 and 10.45-GHz measurements. The grey area corresponds to all the measurements independently of time offset. The solid line shows the distribution for measurements within 1 day and the dashed the measurements within a month. It apparent that the statistics are not influenced.**

The spectral index distributions presented so far have been based on non-simultaneous observations. This has been a necessary compromise imposed by the weather conditions and the large time demand of the project. However, possible variability of the radio sources can induce a time dependent radio spectrum. Provided that the initiative for the current study is the identification of steep spectrum sources, this very fact may lead to misidentification. On the other hand, it is reasonable to expect only minor changes in the statistics, if at all.

For the sake of the correctness of this statement, the previous studies have been repeated on the basis

only of quasi-simultaneous measurements. Figure 4.11 illustrates the distributions resulted on the basis of 1 and 30 days of separation between the measurements at 4.85 and 10.45 GHz (solid and dashed line, respectively). It is already apparent from that plot that in terms of statistics the lack of simultaneity of the measurements does not comprise a major factor of uncertainty. Nevertheless, one must bare in mind that once a certain spectrum is used as the starting point for further studies of a given source it must be confirmed with truly simultaneous observations.

4.3.2   Flat spectrum sources spectral index

Among the sources that have been clearly detected at both 4.85 and 10.45 GHz, a large portion ($\sim 30\%$) of them exhibit flat or inverted spectral index. That is, according to the widely adopted convention $\alpha \geq -0.5$. These source are usually mostly flat spectrum radio quasars (hereafter FSRQs).

In table 4.4 are gathered the average and the median values for the distributions of those sources. It is interesting to mention that these values are verifying other works at similar frequency bands such as Ricci et al. (2006). By definititon, this class of sources immediate interest to CMB experiments. That is

Table 4.4: **The average and median spectral indices for flat spectrum sources that is, sources with $\alpha \geq -0.5$**

Spectral index	Average index	Median Index
$\alpha_{1.4}^{4.85}$	-0.028 ± 0.031	-0.148 ± 0.004
$\alpha_{4.85}^{10.45}$	-0.025 ± 0.033	-0.158 ± 0.023
LSF $\alpha_{1.4}^{10.45}$	-0.122 ± 0.023	-0.225 ± 0.003

because given their flat spectrum the contaminate the higher frequency flux density data.

4.4   Discussion

Generally speaking, the spectral indices calculated here are very close to the expected values assuming that most of the sources are characterized by steep spectra coming from the synchrotron mechanism.

As it shown earlier, the spectral indices (average, median or mean) similar over different fields especially taking into account the estimated errors. Still, the slight differences can be attributed to noise coming from different weather conditions under which each field has been observed. This is not so obvious at a first glance. It can be the case because different fields have been observed at different time of the day due to LST arguments in combination with the scheduling.

A very interesting topic to be discussed is the steepening of the spectra ($\Delta\alpha$) as a function of the redshift (or equivalently with the luminosity) for steep spectrum sources. This can provide evidences about the evolution of such sources in a very simple way. According to what is believed today, looking at larger z's we see younger sources than when looking at small z's. They are characterized by the typical synchrotron self absorbed spectrum that in the optically thin part is evolving as $\nu^{-0.7}$ and at higher frequencies showing even the high frequency break due to the ageing of the electrons. Under these circumstances, the low frequency spectral index should statistically be less negative than the high frequency one assuming that the former is sampling the part before the break and the latter the one after that. At the local universe the source have gone "old" shifting the high frequency break at lower frequencies. In this case both spectral indices sample the same part of the spectrum (the part after the break) showing no significant change in the spectral index. From this discussion it is already clear why steep spectrum sources are the appropriate sample to apply such an investigation. If for example one studies compact flat spectrum sources there is no change is spectral index expected.

Ricci et al. (2006) find an anti-correlation between $\Delta\alpha$ and luminosity. As they discuss, this translates into an anti-correlation of their high frequency spectral index with luminosity (see also Dunlop and
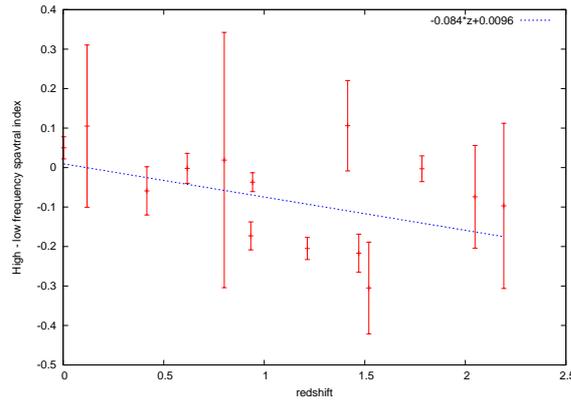
Figure 4.12: **The steepening of the spectral index as a function of z. Here is plotted** $\Delta\alpha = a_{1.4}^{4.85} - a_{4.85}^{10.45}$ **against z. The blue line is described by** $-0.084 \cdot z + 0.0096$. **Only steep spectrum sources have been used.**

Peacock, 1990). For a very small number of steep spectrum sources that there is available redshift information, we attempt to see whether such a steepening appears. The result is shown in figure 4.12. From that plots it is clear that more data points would be necessary. In any case though there is a trend showing that indeed the spectral indices become steep at higher frequencies. It highly important though to clarify that this topic should be investigated thoroughly with dedicated projects. In particular a larger frequency distance would probably reveal a most clear relation.

The findings in the current chapter are used later for important studies concerning the source counts at different frequencies and consequently the calculation of the confusion limits. Besides, the findings presented here are those satisfying the initiative of the project which the estimation of the 31-GHz extrapolated flux density.

5. Cosmological Studies

The question is not what you look at, but what you see.

Henry David Thoreau (1817 - 1862)

Abstract

The flux density measurements as described in earlier chapters comprise the base for estimating the flux density of sources at the high frequency regime of 31 GHz where CBI is operating. Extrapolating at different frequencies one can study the expected number of sources per flux density bin (differential source counts) and compare them if possible with real surveys at each frequency. Moreover, one can predict the "confusion" limits. That is, the flux density levels resulting from the blends of unresolved sources. That has a great practical interest for any observation since this is a physical limitation to the performance of any telescope as we saw in chapter 3. Besides, such studies give the opportunity for some interesting studies of evolutionary models.

5.1   The Extrapolated 31-GHz Flux Densities

In chapters 4 and 3 the measurements at 4.85 and 10.45 GHz with the 100-meter telescope at Effelsberg have been used for the determination of the three-point spectral index of each of the target sources and the construction of the $\log N - \log S$ plots.

Having an estimate of the spectral behavior of a radio source via the determination of the spectral index and the flux densities at 1.4, 4.85 and 10.45 GHz can serve as means of calculating the flux density at higher frequencies. This is done via extrapolating at higher frequencies in a power law manner. That is, the dependence of the flux density on frequency is assumed to be a single power law of the form $S \propto \nu^{\alpha}$. As is already mentioned elsewhere:

$$S = k \cdot \nu^{\alpha} \tag{5.1}$$

Apparently, this relation appears as a straight line when plotted in logarithmic space. Of course, this implies certain assumptions the most important of which being that the spectral index retains the same value through the whole band from 1.4 to the high frequency limit (i.e. 31 GHz). It is common that the spectrum of a radio source is described as a polynomial function of the logarithm of the spectral index as many sources seem to have a curved spectrum. This allows a smoother behavior in the logarithmic space and it is described by:

$$\log(S) = a + b \cdot \log(\nu) + c \cdot \log^2(\nu) \tag{5.2}$$
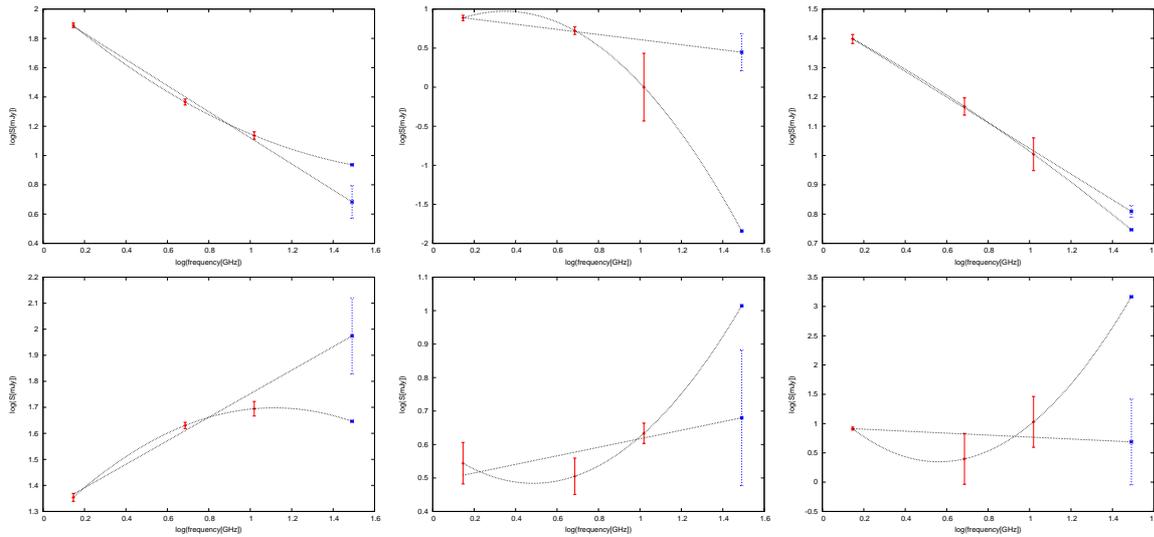
Figure 5.1: **Examples of fitted spectra along with the estimated extrapolated flux density. Both a linear and a quadratic model has been fitted always in log space. It is clear that the two models often differ significantly.**

For the current report both methods have been attempted. However, the latter method has the tendency to exaggerate the results (see figure 5.1). This easily understood given the small number of points (three) available for fitting the spectrum. This is why the actual results are produced by assuming a power law. The data then have been being fitted with the corresponding function by nonlinear least-squares Marquardt-Levenberg algorithm (Marquardt, 1963) as it is discussed in sub-section 4.3.1.

For those fits, every single observation has been used independently of whether it resulted a detection or not. In case of a detection the situation is clear. In the case of a non-detection though the observed noise has still been used as follows. Let σ_S be the noise level reached at a given observation. In case of no detection then for the calculation of the least square fit spectral index the flux density of the source is assumed to be $2.5\,\sigma_S \pm 2.5\,\sigma_S$. This policy assures that even for the not detected sources an estimate concerning their flux density can be made.

Having calculated the extrapolated flux densities at any higher frequency and in particular at 31 GHz, one has a handle on a series of issues. First of all, one can draw conclusions about the amount of flux density that each target may contribute to the CMB anisotropies as observed by the CBI experiment. Further, via the construction of the differential source counts plots, the distribution of radio source can be studied. Of course this topic is very sensitive to the completeness of the sample as has already been mentioned. Consequently, this product can be used for computing the "confusion limit" (sub-section 5.3). This particular result is of great practical importance since it may cast light in several matters among which the overall uncertainties as they were discussed in earlier section (3.2.2). Finally, it is important to examine the possible discrepancy between these results and those from different independent studies such as high frequency surveys.

5.1.1 CBI contamination

The initiation of the CBI-Effelsberg survey has been the identification of the sources that may cause severe data contamination. As it has been discussed in the introduction, the CMB data coinciding with point sources known to exist fro the NVSS survey have been "projected out" causing a severe loss of data of the order of 20 %. In particular, it is easy to show that the necessary levels to be reached at Effelsberg

is around a few mJy. For the sensitivity Γ of a telescope of dimeter D aperture efficiency n_A, it is:

$$\Gamma = n_A \cdot \frac{\pi \cdot D^2}{8 \cdot K} \tag{5.3}$$

where $\quad K$: Boltzman's constant

For Effelsberg telescope then and for the 100-meter telescope one calculate that $\Gamma \approx 2844\,\mathrm{K/Jy}$. That means that 1 mJy at Effelsberg corresponds to a fraction of 10^{-6} K which is the typical amplitude of the CMB anisotropies. Of course this is very simplified calculation since it neglects the fact that CBI is an interferometer etc. It nevertheless gives a good estimate.

Although it is beyond the scope of this report to present exact catalogs it still very interesting to see how many sources show extrapolated flux density at 31 GHz which below the threshold of 1-5 mJy and hence are not potential contaminants. In figure 5.2 we present the histogram of the extrapolated flux densities. This is already possibly the most convenient way of drawing a clear impression of how many
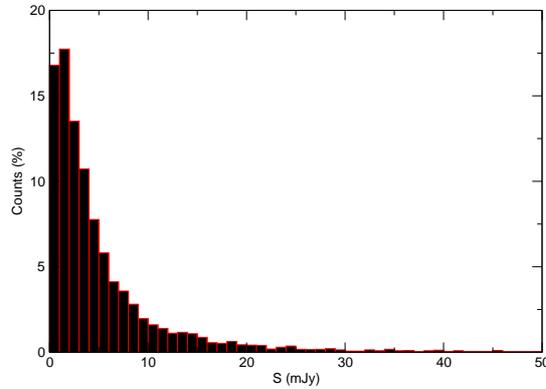
Figure 5.2: The histogram in percentages of the extrapolated flux densities. Also upper limits have used. Here, we focus on the low part of the flux density range. Half of the fluxes are bellow 3 mJy. The bin is 1 mJy wide.

sources can be causing contamination (i.e. be above the set threshold). In that plot also upper limits of undetected sources have been used. Therefore, this plot is representing rather the most pessimistic scenario. As we discussed tough in sub-section 3.3.2 and showed in table 3.5 roughly 76 % of the sources are not detected at 10.45 GHz leading to the reasonable assumption that they are of potential harm to the CBI data. This is already in agreement with the original estimation in the proposal of the project itself that only a number of 20 % is expected to be causing contamination.

A summary then one might say that the projecting out only 20 % of the sources is indeed the correct estimation. That is resulting the necessity of throwing only a 4 % of the data (contrary to 20 %) increasing significantly the sensitivity of the experiment.

5.1.2 The source counts of the extrapolated 31-GHz flux densities

Given that the central frequency of the CBI experiment is 31 GHz (Padin et al., 2001, 2002), it is important that the extrapolated flux densities are calculated at this particular frequency. Sustaining the strategy followed in section 3.3 and assuming the area covered by the Effelsberg-CBI project 0.047 sr, we have fitted to the data a power law as described in sub-section 3.3.1:

$$\text{for } 10\,\mathrm{mJy} \leq S \leq 100\,\mathrm{mJy}: \quad n(S) = 0.48\,(\pm 0.02) \cdot 10^6 \cdot S^{-2.30\,(\pm 0.02)}\,\mathrm{mJy}^{-1}\,\mathrm{sr}^{-1} \tag{5.4}$$
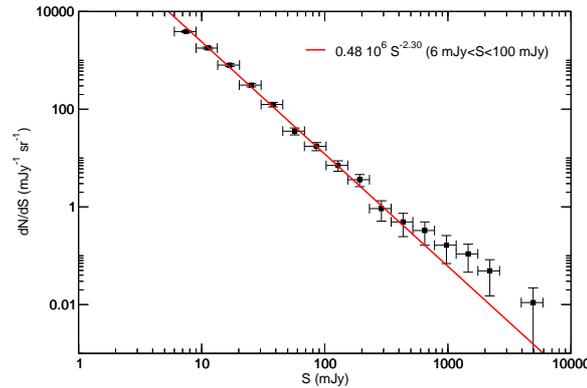
Figure 5.3: **The normalized differential source counts of the extrapolated 31-GHz flux densities. The calculation of the spectral index has been done on the basis of equation and even non-detections have been used by setting an upper flux density limit.**

In figure 5.3 we show the normalized differential source counts plots. Unfortunately, those fits are very sensitive to the chosen binning. For consistency, the bin size used here is identical to those used for the derivation of the same relations at 4.85 and 10.45 GHz (see sub-section 3.3.4 and 3.3.3). Working out the cumulative source counts, gives:

$$N(> S) = 0.37\,(\pm0.02) \cdot 10^6 \cdot S^{-1.30\,(\pm0.02)}\,\mathrm{mJy}^{-1}\,\mathrm{sr}^{-1} \tag{5.5}$$

Given the fact that as it was discussed earlier even upper limits were used for undetected sources, the resulted sample used for the construction of the source counts plots is reasonably statistically complete. In case of multiple measurements of the same source at one frequency, the weighted average of the flux density is used.

In figure 5.3 one can notice a break at around 400 mJy and one at slightly above 1000 mJy. In fact this indicates that there is an good agreement with the theoretically expected counts as it is discussed in sub-section 5.2.3.

5.2   Comparison with high frequency surveys and theoretical models

In sub-section 5.1.2 it was mentioned that it is essential to compare the results from direct high frequency surveys with the ones extracted from the extrapolated flux densities at the same frequency band. This can apparently serve a consistency check that would characterize the reliability of any result that will be drawn from the current work. On the other hand, it can characterize the completeness of our sample. For instance, it is not expected that many sources have such an inverted spectrum as to be missed by NVSS but to appear at higher frequencies. If however this is the case then it will be imprinted in the findings of "blind" high frequency surveys that will significantly differ from our results which are solely based on the NVSS sample. The product that can readily provide a ground for such comparisons is the $\log N - \log S$ plots. By definition, they include the demographics of radio sources integrated over all distances. Hence, they must exhibit significant differences if the used surveys are based on different samples.

In the current section we start with the compilation of some surveys at high frequencies that are of interest to our work. That is, for instance of similar frequency so that the comparison to it is sensible

(sub-section 5.2.1). Afterwards, a short discussion on the expected values is done (sub-section 5.2.2). Finally, we compare out results to the findings of other surveys and to the theoretically expected ones (sub-section 5.2.3).

5.2.1 High frequency surveys

In the current section we mean to gather the findings of some high frequency surveys that appear to have similarities with ours. This is crucial in the evaluation of the completeness and the reliability. Emphasis has of course been given to the high frequency surveys since it is interesting to check whether the population of sources at low frequencies is representative of that at higher frequencies.

To each individual project there has been dedicated a separate sub-section so the manuscript sustains a clarity in the organization.

The 15.2-GHz Ryle telescope survey

The Ryle Telescope (for a description of main features see Jones 1991) has been used for conducting the 9C survey at 15.2 GHz (Waldram et al., 2003). The initiative of this has been the study of the foreground sources that contaminate the fields targeted by the Very Small Array (VSA) experiment (Watson et al., 2003). Practically, the motivation has been the assemblage of a catalog of sources that must be monitored by VSA at 34 GHz (Taylor et al., 2003). The survey has covered three regions of a total area of $520\,\text{deg}^2$ and has been conducted in two parts. A main survey that reaches 25 mJy and a deeper one that reaches 10 mJy. It has detected a total of roughly 760 sources brighter than 10 mJy. It is noteworthy though that this survey is the first one covering a significant area at a frequency above 4.85-GHz Green Bank survey (Gregory et al., 1996).

At the first release of the data (Taylor et al., 2001) and on the basis of a very limited coverage of $63\,\text{deg}^2$, they computed:

$$\text{for } 20 \leq S \leq 500\,\text{mJy}: \quad n(S) = 8 \cdot \left(\frac{S}{100\,\text{mJy}}\right)^{-2.0} \text{mJy}^{-1}\,\text{sr}^{-1} \tag{5.6}$$

In the second release of the data (Taylor et al., 2003), they show that:

$$n(S) = 54 \cdot \left(\frac{S}{\text{Jy}}\right)^{-2.15} \text{Jy}^{-1}\,\text{sr}^{-1} = 0.15 \cdot 10^6 \cdot S^{-2.15}\,\text{mJy}^{-1}\,\text{sr}^{-1} \tag{5.7}$$

The authors do not report the uncertainty in the multiplication factor and the exponent. It is worth mentioning though that this survey is a good example of how complicated the source counts study may be. From the equations above one can immediately see that this study is very sensitive to the sample upon which it has been based and how large it has been. This influence is evident not only in the constant factor but also in the index.

The ATCA 18-GHz pilot survey

As a pilot study for the first all sky radio survey at short wavelengths Ricci, Sadler, Ekers, Staveley-Smith, Wilson, Kesteven, Subrahmanyan, Walker, Jackson and De Zotti (2004) have covered an area of $1216\,\text{deg}^2$ of the southern sky at 18 GHz. The survey is claimed to be 70% complete down to 126 mJy and 95% down to 300 mJy. For the flux density range from 0.1 to 3 Jy the differential source counts are worked out to be:

$$\text{for } 0.1\,\text{Jy} \leq S \leq 3\,\text{Jy}: \quad n(S) = 57 \cdot \left(\frac{S}{\text{Jy}}\right)^{-2.2\,(\pm 0.2)} \text{Jy}^{-1}\,\text{sr}^{-1}$$

$$= 0.23 \cdot 10^6 \cdot S^{-2.2\,(\pm 0.2)}\,\text{mJy}^{-1}\,\text{sr}^{-1} \tag{5.8}$$

The 28.5-GHz OVRO-BIMA survey

Also in the context of studying the point sources contaminating CMB and Sunyaev-Zel'dovich effect experiments Coble et al. 2006 carried out a survey at 28.5 GHz with the Owens Valley Radio Observatory (OVRO) and the Berkeley-Illinois-Maryland-Association (BIMA) arrays. They computed the source counts from 90 fields centered on known massive galaxy clusters and 8 non-cluster fields. From the latter the calculate that:

$$n(S) = 5.81^{+6.7}_{-3.1} \cdot 10^{-3} \cdot S^{-1.98} \, \text{mJy}^{-1} \, \text{arcmin}^{-2} = 0.07^{+0.08}_{-0.04} \cdot 10^6 \cdot S^{-1.98} \, \text{mJy}^{-1} \, \text{sr}^{-1} \quad (5.9)$$

Moreover, they compute significantly different numbers for regions on the clusters. In particular, depending on the distance from the center of the galaxy cluster itself, they find that for the *Inner cluster* ($r \leq 0.5$ arcmin):

$$n(S) = 174^{+89}_{-39} \cdot 10^{-3} \cdot S^{-1.98} \, \text{mJy}^{-1} \, \text{arcmin}^{-2} = 2.05^{+1.05}_{-0.46} \cdot 10^6 \cdot S^{-1.98} \, \text{mJy}^{-1} \, \text{sr}^{-1} \quad (5.10)$$

and for the *Outer cluster* ($r \geq 0.5$ arcmin):

$$n(S) = 19.1^{+6.7}_{-4.9} \cdot 10^{-3} \cdot S^{-1.98} \, \text{mJy}^{-1} \, \text{arcmin}^{-2} = 0.23^{+0.08}_{-0.06} \cdot 10^6 \cdot S^{-1.98} \, \text{mJy}^{-1} \, \text{sr}^{-1} \quad (5.11)$$

Interestingly they argue that it is possible that the enhancement of the sources counts in the direction of the clusters may be attributed to the gravitational lensing of background radio galaxies (Cooray et al., 1998).

The 31-GHz OVRO-CBI survey

Fortunately, at the first stage of the CBI data analysis the experiment team studied the foreground point sources at 31 GHz with the Owens Valley Radio Observatory, hereafter OVRO, telescope (Mason et al., 2003). In particular, the CBI team selected all the NVSS sources brighter than 6 mJy that happen to lie within the area covered by CBI at that time. That resulted a sample of 2225 sources within 22.5 deg². Quasi-simultaneously, they re-observed the sources at 31 GHz with the OVRO 40-meter telescope with a sensitivity of the order of 2 mJy (rms).

Moreover, they used the deep and the mosaic maps to determine the source counts at 31 GHz. Specifically, the used the long baselines data ($> 250 \, \lambda$) to create maps and then search for peaks of more than $5 \, \sigma$. For the range between 5 and 50 mJy, they find:

$$N(>S) = 2.8 \, (\pm 0.7) \, \text{deg}^{-2} \left(\frac{S_{31}}{10 \, \text{mJy}} \right)^{-1.0} \Rightarrow n(S) = 0.9 \, (\pm 0.3) \cdot 10^6 \cdot S^{-2} \, \text{mJy}^{-1} \, \text{sr}^{-1} \quad (5.12)$$

There are no errors concerning the exponent reported in the associated publication. It is noteworthy that there were no objects detected that were not included in the NVSS catalog. It is also important that the flux densities of sources detected at both the mosaic and the deep maps are consistent with that from the OVRO survey within typically 5 %.

The 31-GHz DASI experiment

The Degree Angular Scale Interferometer (DASI, Kovac et al., 2002) is a south-pole experiment dedicated to the study of polarization of the CMB anisotropies. From their measurements at 31 GHz, they calculate:

$$n(S) = 32 \, (\pm 7) \cdot \left(\frac{S}{70 \, \text{mJy}} \right)^{-2.15 \, (\pm 0.20)} \, \text{Jy}^{-1} \, \text{sr}^{-1} = 284 \, (\pm 62) \cdot 10^6 \cdot S^{-2.15 \, (\pm 0.20)} \, \text{mJy}^{-1} \, \text{sr}^{-1} \quad (5.13)$$

for a flux density range between 0.1 and 10 Jy. It should be noted though that the size of their sample is very limited (31 sources).

The 33-GHz VSA survey

The Very Small Array (VSA, Watson et al. 2003) is also a CMB interferometer operating at 33 GHz. Cleary et al. (2005) estimated the source counts at 33 GHz after constructing a sample as follows. A set of well defined regions previously surveyed at 15 GHz within the VSA target fields have been selected. For those fields the survey has been done down to a completeness limit of 10 mJy. This way a total area of 0.044 sr was covered revealing a total of 370 sources with $S_{15} \geq 10$ mJy. Consequently, these sample was re-targeted at 33 GHz.

$$n(S) = 10.6^{+2.3}_{-2.2} \left(\frac{S}{70 \, \text{mJy}} \right)^{-2.34^{+0.25}_{-0.26}} \text{mJy}^{-1} \, \text{sr}^{-1} = 0.22^{+0.05}_{-0.05} \cdot 10^6 \cdot S^{-2.34^{+0.25}_{-0.26}} \, \text{mJy}^{-1} \, \text{sr}^{-1} \quad (5.14)$$

Importantly, provided that the VSA target fields have been selected to encompass no sources brighter than 500 mJy at 33 GHz (from extrapolating the NVSS and GB6 data) the used sample is incomplete at large flux densities.

The WMAP

The Wilkinson Microwave Anisotropy Probe (WMAP, Bennett et al. 2003) is a mission dedicated to the exploration of the geometry, content and the evolution of the universe by means of studying the anisotropies imprinted in the microwave background. The sky maps have been made at five frequency bands (23, 33, 41, 61, 94 GHz) in order to separate the features really intrinsic to the CMB from those of contaminating character. In particular, diffuse Galactic emission and Galactic or extragalactic point sources. The contamination from the latter ones have been estimated on the basis of extrapolation of the source counts from lower or higher frequency surveys (Park et al. 2002; Sokasian et al. 2001; Refregier et al. 2000).

The WMAP team though has carried out a direct investigation of the point-source content off the WMAP maps by constructing a extensive source catalog. Specifically, the GB6 (Gregory et al., 1996) and the PMN catalog (Wright et al., 1994) have been combined in a longest list of 119,619 sources. For each source with $|b| \geq 10°$ they examine the corresponding WMAP pixel. Using also the 4.85-GHz flux density they find that the detected sources are primarily flat spectrum ($\alpha \sim 0$). From these measurements, the extract:

$$\text{K-band (23 GHz), for 2 Jy} \leq S \leq 10 \, \text{Jy:} \quad n(S) = 45 \, (\pm 12) \cdot \left(\frac{S}{\text{Jy}} \right)^{-2.8 \, (\pm 0.2)} \text{Jy}^{-1} \, \text{sr}^{-1}$$

$$= 11 \, (\pm 3) \cdot 10^6 \cdot S^{-2.8 \, (\pm 0.2)} \, \text{mJy}^{-1} \, \text{sr}^{-1} \quad (5.15)$$

$$\text{Ka-band (33 GHz), for 2 Jy} \leq S \leq 10 \, \text{Jy:} \quad n(S) = 44 \, (\pm 12) \cdot \left(\frac{S}{\text{Jy}} \right)^{-2.8 \, (\pm 0.2)} \text{Jy}^{-1} \, \text{sr}^{-1}$$

$$= 11 \, (\pm 3) \cdot 10^6 \cdot S^{-2.8 \, (\pm 0.2)} \, \text{mJy}^{-1} \, \text{sr}^{-1} \quad (5.16)$$

$$\text{Q-band (41 GHz), for 2 Jy} \leq S \leq 10 \, \text{Jy:} \quad n(S) = 32 \, (\pm 9) \cdot \left(\frac{S}{\text{Jy}} \right)^{-2.7 \, (\pm 0.2)} \text{Jy}^{-1} \, \text{sr}^{-1}$$

$$= 4 \, (\pm 1) \cdot 10^6 \cdot S^{-2.7 \, (\pm 0.2)} \, \text{mJy}^{-1} \, \text{sr}^{-1} \quad (5.17)$$

The indices computed here are very close to the ones expected for a Euclidean universe. It is worth noting that the survey favors the flat spectrum sources as the authors of the original paper discuss.

5.2.2 The expected values

Among the most important motivations for the current work is of course the investigation of how complete the extrapolated flux densities are and the agreement between different independent surveys. Disagreements may result from incompleteness of the compared samples since for currently reported project

the counts are the result of extrapolation. That is, the high frequency source counts and later the calculation of the confusion limits, are based by extrapolating the low frequency detections and the low frequency spectral indices ($\alpha_{1.4}^{4.85}$ and $\alpha_{4.85}^{10.45}$). This allows solid conclusion only under the assumption that the used sample is complete and reliable (see definitions in sub-section **??**). In this context one can speculate: is the populations "created" by extrapolation of low-frequency detected sample representative of those at higher frequencies? To put it differently, are we missing a statistically significant population of sources by extrapolating? Or are we even overestimate the contribution of the low frequency population when we go higher?

It is natural to expect that all these issues rely on several matters such as the source evolution and they are addressed by several theoretical models. Large effort has been put in the direction of calculating the population expected at high frequencies (a few tens of GHz). Here it is attempted to recollect what is theoretically expected and see how much these predictions agree with the observations. Earlier work on this direction has chiefly been based on radio source evolution (Dunlop and Peacock, 1990; Jackson and Wall, 1999; Toffolatti et al., 1998). The frequency regime covered is below 8 GHz. Specifically, the model by Toffolatti et al. 1998 has been used for the estimation of the radio source contamination of CMB maps (e.g. Refregier et al., 2000). It appears that it satisfactorily represents the high frequency
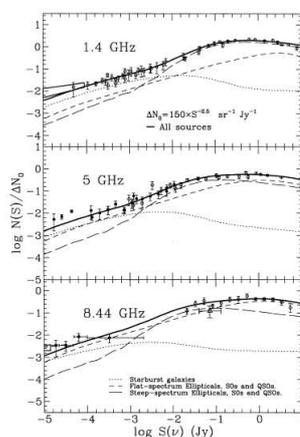
Figure 5.4: **Comparison between predicted and observed differential source counts at 1.4, 5 and 8.44 GHz normalized to $150 S^{-2.5}\,\mathrm{sr}^{-1}\,\mathrm{Jy}^{-1}$ (Toffolatti et al., 1998). The contributions of the most relevant classes of radio sources according to the model of Danese et al. (1987) are label.**

populations. As stated by De Zotti et al. (2005) recently accumulated data required a more detailed treatment.

In particular, De Zotti et al. (2005) take into account the various sub-populations. They consider a canonical radio source population as well as a variety of special source cases. Different evolutionary models have been employed in describing the flat spectrum radio sources (i.e. Flat Spectrum Radio Quasars, FSRQs and BL Lac objects) and the steep spectrum sources. Eventually they derive the expected counts for all radio species; that is star-forming galaxies, extreme GHz-Peaked Spectrum sources (GPS), Advection Dominated Accretion Flow (ADAF, Fabian and Rees 1995) and Adiabatic Inflow-Outflow Solutions (ADIOS, Blandford and Begelman 1999), Sunyaev-Zel'dovich effects (Sunyaev and Zeldovich, 1972) on several scales and even radio afterglow attributable to γ-ray bursts (GRB). In figure 5.5 are collected their results as taken from the original publication. They show very clearly the estimated contribution from each class at 20 and 30 GHz. It is worth noting the flux density range covered (six orders of magnitude). The lack of analytical expressions of their models, currently prohibits a detailed comparison with our results and those from other surveys. At first look though the source counts

from these models are significantly flatter than the surveys in sub-section 5.2.1 imply.

The work of De Zotti et al. (2005) has been based on previous work done by Toffolatti et al. (1998). They worked out the contributions of extragalactic radio sources to the *Planck Surveyor* mission. It is remarkable that here the flux density range covered is even more extended (seven orders of magnitude). As stated in the publication there is a very good agreement of the model by Danese et al. (1987) and the deep counts at 8.44 GHz as given by Partridge et al. (1997) and Windhorst et al. (1993).

It appears that generally the theoretical models can fit the observational data satisfactorily. However, the details can be addressed only under the light of dedicated high frequency surveys that are essential in all the above. Nevertheless, focusing only on the observational part it is interesting to see how the extrapolated values extracted from our survey are compared to those extracted from "blind" surveys. It has already been mentioned that this is a powerful test for the reliability and the completeness of our survey.

5.2.3 The comparison

Let us recall once more the plot in figure 5.3 that shows the differential source counts for the extrapolated flux densities at the frequency of 31 GHz. A careful look there shows two prominent breaks in the index. The first appears at around 400 mJy and the second one at slightly above 1000 mJy. On the other hand, looking at the 30-GHz part of figure 5.5 (the four lower panels) one can easily see that such a behavior is predicted by De Zotti et al. (2005). In fact, especially the high-flux-density break is predicted at the regime we observe it. This is interesting one its own sake since it indicates that we do not really miss much information by extrapolations. Moreover, it supports the models presented by De Zotti et al. (2005). Furthermore, it appears that even the constant factor of $0.48 \cdot 10^6$ in equation 5.4 derived from the fit is in good agreement with the predicted values from the same author. All these of course is a source of great excitement but it must be examined further.

Now, table 5.1 summarizes the differential source counts for the sample within the CBI fields derived after extrapolation (or interpolation) along with the values coming from other direct surveys at the same frequencies. Especially, for the frequency of each of the previously discussed surveys we have computed the source counts. This is a convenient way to compare the two and examine their completeness. The fits to the extrapolated Effelsberg data have been restricted between 6 and 100 mJy and the experiment area has been assumed to be 0,047 sr.

In figure 5.6 are shown the results from that table in a graphical way. The noisiness of the data there is prominent. Most likely this is the result of the small number statistics. As we already discussed in the paragraph concerned about the 15.2-GHz Ryle telescope survey, this study is complicated on its own and very sensitive to technicalities. More importantly though may be the influence of selection effects (biases of the samples). Nevertheless, the strongest influence must be coming from flux density range covered by the sample used. That follows easily when we consider the distribution of sources even at lower frequencies as shown in figure 5.7 (Seymour et al., 2005). However, generally speaking also this plot seems to support the modeling of De Zotti et al. (2005) as long as the index is concerned. As we said already, they predict that above 100 mJy the source counts evolve faster with flux density (they become steeper). This is exactly what one notices from the WMAP data at all three frequencies. Recall that WMAP's flux density range is between 2 and 10 Jy. Now, the ATCA and the DASI experiments are both sensitive in the flattening part of the plots (roughly $300 - 1000$ mJy). The former is observing from 100 to 3000 mJy and the latter from 100 to 10000 mJy indicating that the agreement with the predicted is very satisfactory. BIMA-OVRO and CBI-OVRO surveys are also very close in their findings as expected since they are both sampling the rather low part of the flux density regime. Our extrapolated flux densities appear to be in good agreement with the VSA survey. Remember that for the fits we use only the data between 6 and 100 mJy which is more or less the range of VSA counts (20-114 Jy). The only survey that gives somewhat inconsistent results is the Ryle Telescope one. That should appear with steeper index. It is highly probable thought that the fit is influence by the flat part of the source count between 300 and
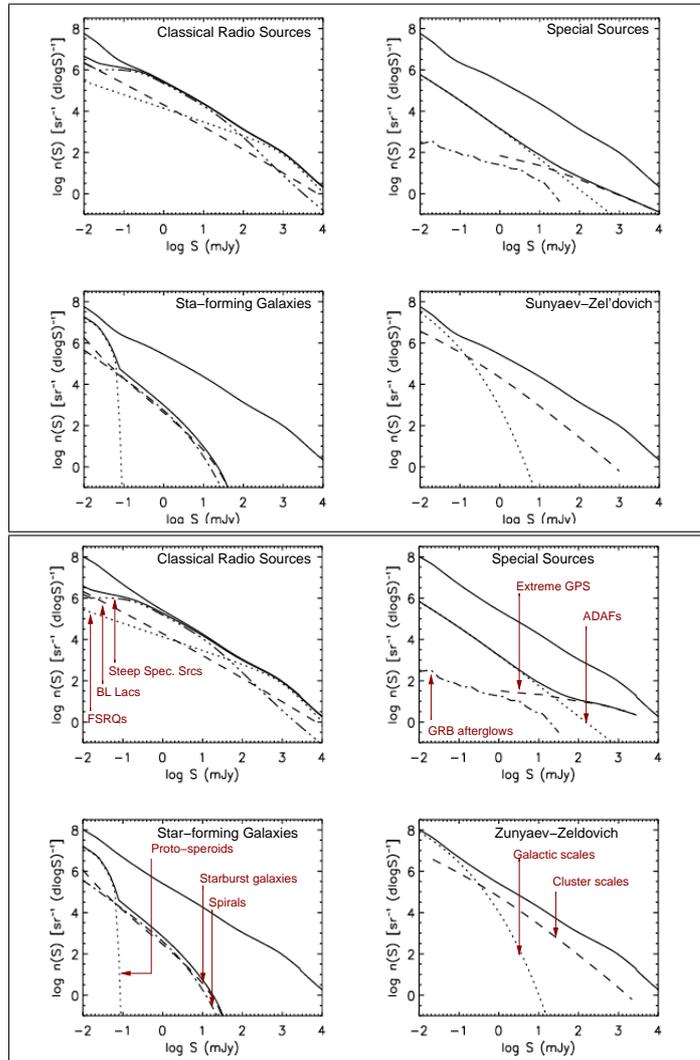
Figure 5.5: **Differential source counts at 20 and 30 GHz for various extragalactic source populations as predicted by De Zotti et al. (2005). The upper group of four panels refers to the 20-GHz predictions whereas the lower n to the 30-GHz ones. For each group the panels are organized as follows.** *Upper left-hand panel*: **Classical radio sources, that is FSRQs (dotted line); BL Lacs (dashed line), steep spectrum sources (triple dot-dashed line).** *Upper right-hand panel*: **Special sources, that is: ADAFs (dotted line), extreme GPS quasars ad galaxies (dashed line), GRB afterglow (dot-dashed line).** *Lower left-hand panel*: **star-forming galaxies. That is, proto-spheroids (dotted line), spirals (dot-dashed line),starburst galaxies (dashed line).** *Lower right-hand panel*: **SZ effect on galactic scales (dotted line) and on cluster scales (dashed line). The sum of all contributors is shown as a thin solid line. The overall total counts as a thick solid line.**

Table 5.1: **The Collection of the normalized differential source counts as taken from several typical high frequency surveys. For each survey the values from the extrapolation of the Effelsberg data is also referred to. That is done simply by fitting a straight line in the $\log N$-$\log S$ plots. It is important to mention that the results from the extrapolated values have been done between 6 and 100 mJy.**

Survey	Frequency (GHz)	Range (Jy)	$n(S)$ measured	$n(S)$ NVSS-Effelsberg extrapolated
			$(10^6\ \mathrm{mJy}^{-1}\ \mathrm{sr}^{-1})$	
Ryle Tel.[1]	15.2	0.02−0.5	$0.15 \cdot S^{-2.15}$	$1.3\,(\pm 0.30) \cdot S^{-2.59\,(\pm 0.09)}$
ATCA [2]	18	0.10−3.0	$0.23 \cdot S^{-2.20\,(\pm 0.2)}$	$0.79\,(\pm 0.09) \cdot S^{-2.44\,(\pm 0.05)}$
WMAP [3]	23	2.0−10	$11.3\,(\pm 3) \cdot S^{-2.80\,(\pm 0.2)}$	$0.62\,(\pm 0.10) \cdot S^{-2.38\,(\pm 0.07)}$
BIMA-OVRO[4]	28.5	0.005−0.010	$0.07^{+0.08}_{-0.04} \cdot S^{-1.98}$	$0.47\,(\pm 0.08) \cdot S^{-2.29\,(\pm 0.07)}$
CBI [5]	31	0.006−	$0.9\,(\pm 0.3) \cdot S^{-2.00}$	$0.48\,(\pm 0.02) \cdot S^{-2.30\,(\pm 0.02)}$
DASI [6]	31	0.1−10	$284\,(\pm 62) \cdot S^{-2.15\,(\pm 0.2)}$	−
WMAP [3]	33	2−10	$11.3\,(\pm 3) \cdot S^{-2.80\,(\pm 0.2)}$	$0.47\,(\pm 0.02) \cdot S^{-2.30\,(\pm 0.02)}$
VSA [7]	33	0.020−0.114	$0.22\,(\pm 0.05) \cdot S^{-2.34}$	−
WMAP [3]	41	2−10	$4\,(\pm 1) \cdot S^{-2.70\,(\pm 0.2)}$	$0.36\,(\pm 0.01) \cdot S^{-2.21\,(\pm 0.02)}$

[1]Taylor et al. (2003)

[2]Ricci, Sadler, Ekers, Staveley-Smith, Wilson, Kesteven, Subrahmanyan, Walker, Jackson and De Zotti (2004)

[3]Bennett et al. (2003)

[4]Coble et al. (2006)

[5]Mason et al. (2003)

[6]Kovac et al. (2002)

[7]Cleary et al. (2005)
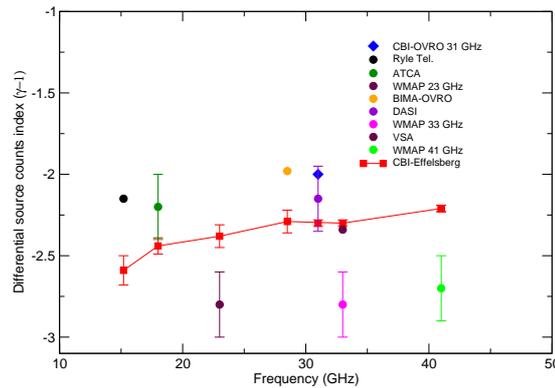
Figure 5.6: **The indices on the differential sources counts power laws (γ-1) for different frequencies. The colored data points are the measured indices and in red those extracted from the extrapolation of the Effelsberg-CBI data (see also table 5.1). Already for the measured indices it apparent a significant noisiness of the data. An important reason for that may be the small number statistics. Moreover, different indices have been extracted from data referring to different flux density ranges.**

1000 mJy.

To summarize one can say that all the surveys together seem to support the idea of De Zotti et al. (2005). From this discussion of course it becomes obvious how sensitive this study is in the selected flux density range. Besides, the counts coming from the extrapolation seem to represent the real populations (as observed by direct "blind" surveys) satisfactorily. In any case, dedicated surveys covering the largest possible flux density ranges would be ideal in reconstructing the observable source counts.

From a different perspective, the knowledge of the extrapolated indices can assist the estimate of the confusion limits. Tat happens to be among the most important initiatives for this work. That is done solely on the basis of the flux densities as extracted from extrapolation of the Effelsberg-CBI measurements. This study is presented in section 5.3.
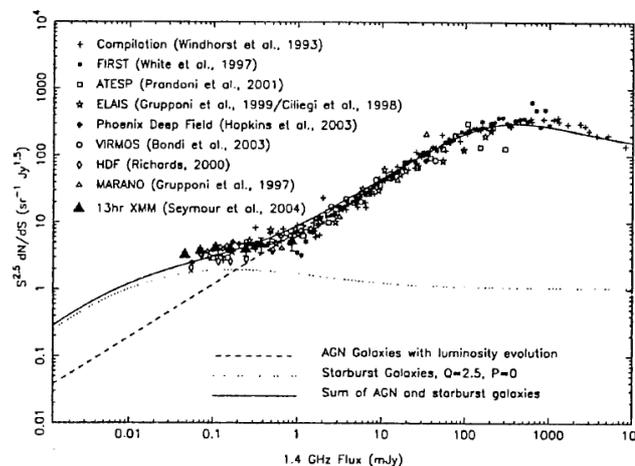
Figure 5.7: **The 20-cm differential source counts normalized at $S^{-2.5}$ based several surveys (Seymour et al., 2005)**

5.3   The confusion limits

The radiometer formula, as given in equation 3.3, does not provide a low limit in the thermal rms noise σ_{th} that characterizes a certain system. Naively then one could expect that a monotonic increase of the integration time would result a similarly monotonic decrease in the least reachable flux density. This is not the case though. In the case of a realistic system any measurement is limited by confusion. That is, the unresolved blends of sources that sum up to significant flux densities. For a given system the confusion level is a function of:

1. The spatial distribution of sources as a function of flux density bin at the corresponding frequency. In other words, the differential source counts $n(S)$.

2. The telescope beam area.

Given the definition of the differential source counts $n(S)$, one can quantify the confusion limit σ_{conf} (see also sub-section 3.2.3), as follows. Let Ω_{beam} be the solid angle subtend to the beam of the telescope at a given frequency ν and S_{min} the attempted minimum flux density. The latter is the value expected from the radiometer formula. Scheuer (1957) has shown that:

$$\sigma_{conf}^2 = \Omega_{beam} \int_0^{S_{min}} n(S)\, S^2\, dS \tag{5.18}$$

with Ω_{beam}, given by:

$$\Omega_{beam} = \int d\phi \int sin\theta\, d\theta \tag{5.19}$$

Given equation 3.13, 5.18 gives:

$$\sigma_{conf}^2 = \frac{|\gamma|}{\gamma + 2} K\, \Omega_{beam}\, S_{min}^{\gamma+2} \Rightarrow \sigma_{conf} = \sqrt{\frac{|\gamma|}{\gamma + 2} K\, \Omega_{beam}\, S_{min}^{\gamma+2}} \tag{5.20}$$

This equation is of great importance as discussed also in sub-section 3.2.3, since it assists in the realistic estimation of the least reachable flux density.

Although trivial at first glance, this piece of information is of essential observational importance. It is clear that such a knowledge is fundamental for a radio-astronomical observation. Even more so is the case for experiments such as CBI, that attempt the un-doubtful detection of anisotropies in the CMB. The anisotropies are expected to be as weak as of the order $\Delta T/T \sim 10^{-6}$.

5.3.1   Confusion limits for the Effelsberg 100-meter telescope

In table 5.2 are summarized the confusion limits calculated for several receivers at Effelsberg. For each receiver (Ω_{beam}) equation 5.20 has been used along wit the values of γ, K and S_{min} included there. For all the calculations the limiting or characteristic flux density level assumed (S_{min}) has been 1 and 5 mJy. The beams are assumed to be circular Gaussian. The solid angle they subtend then is given by (e.g. Rohlfs and Wilson, 2004):

$$\Omega_{beam} = \left[\int_{-\infty}^{\infty} \exp\left(-4 \cdot \ln 2 \cdot \frac{x^2}{\psi^2} \right) \right]^2 = 0.00266 \cdot \psi^2\, 10^{-8} \text{sr} \tag{5.21}$$

where ψ: the FWHM in arcsec

It must be kept in mind that this formula does not account for the side lobes or the deformation of the beam. Nevertheless it still is a good approximation.

The confusion limits calculated from the extrapolated source counts in that table vary smoothly with frequency. That is the consequence of inferring the source counts from extrapolating or interpolating between the measured values at 1.4, 4.85 and 10.45 GHz (they are marked with a dagger symbol). Moreover, the measured source counts result lower values for the confusion limits as compared to that from the extrapolated source counts. That is because in the latter case also upper limits of non detected sources have been used.

It is interesting that the values for the confusion level calculated from the Effelsberg 4.85-GHz measurements agree very well with those from Fomalont et al. (1991, 2002). So is the case for the 2-cm confusion limit as given from our extrapolated source counts and Waldram et al. (2003). It appears then that the measured source counts at the three frequencies used for the CBI-Effelsberg project, can be used to formulate the confusion limit as a function of frequency for the 100-m telescope.

Table 5.2: **Confusion limits for each Effelsberg receiver. All the numbers have been worked out on the basis of the values obtained from the Effelsberg-CBI survey. The parameters at 1.4, 4.85 and 10.45 GHz are from direct measurements. All the computations have been done for two limiting flux densities namely 1 and 5 mJy. There are also some values calculated by Kraus (priv. comm.) based on the literature for comparison (σ_{lit}).**

Frequency	Ω_{beam}	$N(S)$				S_{min}	σ_{conf}	S_{min}	σ_{conf}	σ_{lit}	Ref.
		K	err	γ	err						
(GHz)	(10^{-6} sr)	(10^6 mJy^{-1} sr^{-1})				(mJy)	(mJy)	(mJy)	(mJy)	(mJy)	
1.4[†]	8.000	0.29	0.02	-0.68	0.03	1.0	1.10	5.0	3.16		
2.6	1.800	0.45	0.04	-1.03	0.03	1.0	0.93	5.0	2.02		
4.85[†]	0.540	0.10	0.01	-0.80	0.05	1.0	0.19	5.0	0.49	0.24/0.15	1/2
8.35	0.180	0.77	0.07	-1.5	0.05	1.0	0.64	5.0	0.96		
10.45[†]	0.110	0.07	0.03	-0.83	0.10	1.0	0.07	5.0	0.19		
14.6	0.068	0.65	0.05	-1.5	0.03	1.0	0.36	5.0	0.54	0.11	3
23.05	0.035	0.45	0.08	-1.38	0.07	1.0	0.19	5.0	0.31		
32.00	0.020	0.35	0.07	-1.27	0.07	1.0	0.11	5.0	0.20		
43.00	0.011	0.28	0.05	-1.18	0.07	1.0	0.07	5.0	0.13		

[†]directly measured parameters

[1] Fomalont et al. (1991)

[2] Fomalont et al. (2002)

[3] Waldram et al. (2003)

5.3.2 Formalization of the confusion limit

Using the measured source counts at the three frequencies used for the Effelsberg-CBI project one can formulate the the confusion limit as function of frequency for the 100-meter telescope.

As Condon et al. (1989) discuss, the confusion due to unresolved blends of sources σ_{conf} decreases with frequency. in fact, it is $\sigma_{\mathrm{conf}} \propto \nu^{-2}$. On the other hand the flux density of the source falls a $S \propto \nu^{-0.7}$ for most of the steep spectrum sources. They argue then the there must be a dependency of the form:

$$\sigma_{\mathrm{conf}} \propto \nu^{-2.7} \qquad (5.22)$$

In a more general approach, it would be:

$$\sigma_{\mathrm{conf}} = a \cdot \nu^b \qquad (5.23)$$

Using the values of σ_{conf} calculated for 1.4, 4.85 and 10.45 GHz, and assuming $S_{\text{min}} = 1$ mJy, we get:

$$\sigma_{\text{conf}} = 1.76\,(\pm 0.01) \cdot \nu^{-1.40\,(\pm 0.02)} \text{ mJy} \qquad (5.24)$$

where $\quad \nu$: The observing frequency in GHz

Assuming now that $S_{\text{min}} = 5$ mJy, one calculates:

$$\sigma_{\text{conf}} = 5.19\,(\pm 0.10) \cdot \nu^{-1.48\,(\pm 0.04)} \text{ mJy} \qquad (5.25)$$

where $\quad \nu$: The observing frequency in GHz

Using formulas 5.24 and 5.25 one can provide an estimate for the confusion limit as follows:

Frequency (GHz)	1.4	2.6	4.85	8.35	10.45	14.6	23.05	32.00	43.00
σ_{conf} with $S_{\text{min}} = 1$ mJy (mJy)	1.1	0.46	0.19	0.09	0.07	0.04	0.02	0.01	0.009
σ_{conf} with $S_{\text{min}} = 5$ mJy (mJy)	3.2	1.3	0.5	0.22	0.16	0.1	0.06	0.03	0.02

As an example, for 1.4 GHz these formulas give $1.1 \text{ mJy} \leq \sigma_{\text{conf}} \leq 3.2 \text{ mJy}$. For the 100-meter telescope it has been reported that the confusion is ~ 7 mJy (Wolleben, Diploma Thesis) which is higher that what we get. On the other hand, Reich (priv. comm.) reports a confusion level of ~ 2.3 mJy in good agreement with our estimation.

A careful comparison of the results in table 5.2 and the one above, shows that there is a disagreement.The reason for that is because the latter (which the result of equation 5.25) is derived on the basis of the source counts of detected sources at 4.85 and 10.45 at Effelsberg as it was discussed in the previous sub-section. In any case, equations 5.24 and 5.25 provide a useful formalization for the estimation of the confusion limits at the 100-meter telescope.

6. Peculiar Sources

Your theory is crazy, but it's not crazy enough to be true.

Niels Bohr

Abstract

Being such an extended and complete (in terms of NVSS flux densities) sample the studied one allows its exploitation in several directions. So far the approach is massively statistical neglecting individual source that may exhibit special interest for their characteristics or their nature itself. Admittedly, there is a variety of possible research directions to be followed. Here, the main interest is focused on the GHz-Peaked Spectrum sources their extreme sub-class referred to as High Frequency Peakers. Under certain assumptions and within the context of the "youth" scenario, they comprise the sources with the youngest radio activity. This chapter is meant as a descriptive ones of the main points of our work.

6.1 Introduction

The sample of six thousand sources that has been studied is expected to include a number of sources of special interest such as High Frequency Peakers (HFP), GHz Peaked Spectrum sources (GPS) and Ultra Steep Spectrum sources (USS). Each one being interesting for different reasons, they give the opportunity for some very different studies (eg the early evolutionary studies of young radio sources, see section 6.4).

This approach diverges our study from the massively statistical attitude which attempts the extraction of knowledge from groups of hundreds or thousands of sources, to a more targeted one that treats the source individually yet as a characteristic member of a sub-class of radio sources.

Admittedly, it is anything but trivial to trace down all the interesting sources that happen to be included in our sample. It has been therefore an on-going task to first identify and consequently verify the sources of special interest. Here, we present only a part of the harvest. Specifically, we present some newly discovered GPS sources that according to the "youth" scenario must be amongst the youngest radio sources.

6.2 GHz-Peaked Spectrum and High Frequency Peaking sources

The Compact Steep Spectrum (CSS), Gigahertz Peaked-Spectrum (GPS) and the High Frequency Peaking sources (HFP), comprise a phenomenological classification of radio sources. Their identification is done on the basis of their radio spectra as discussed in following paragraphs. However, it appears that physically they are tightly related with the one being the evolutionary stage of the other. That makes the

physics in play at those environments outstandingly interesting to study. Their properties provides essential information about and constrains on the evolution of the most powerful radio galaxies. A excellent review is given by O'Dea (1998).

The GPS sources display a convex radio spectrum with its observed peak lying in the range of a few GHz. Their are generally compact sources with linear dimensions less than 1 kpc. An extreme case of GPS sources are the HFPs with their turnover frequency above $\sim$10 GHz. Those are among the most interesting species since, under certain circumstances, they comprise the youngest radio sources. Hence, their study provides insight about the very first and rather rapid evolutionary states of radio activity. The CSS sources on the other hand also show convex radio spectra whose peak though appears at far lower frequencies (below the GHz-regime). They are larger in linear size (a few ten kpc) and yet as powerful as the GPS themselves. In figure 6.1 are shown characteristic examples of those three classes of sources.
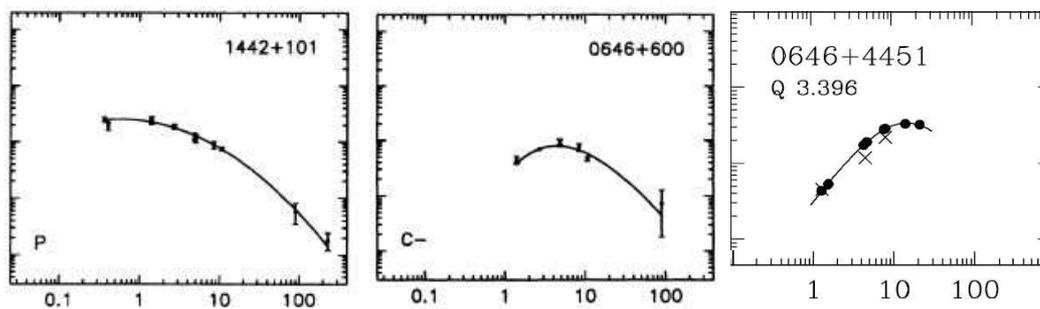
Figure 6.1:   **Characteristic CSS (left-most), GPS (center) and HFP (right-most) sources. The first two are taken from Steppe et al. (1995) and the HFP is taken from Dallacasa et al. (2000)**

Since the presence of the turnover in the spectrum is a determining characteristic of those classes, it is important to mention the possible causes for the presence of such a turnover of the radio spectrum. The most widely accepted idea is that of the synchrotron self-absorption (e.g. Readhead et al., 1996). It has also been suggested that the turnover may be due to free-free absorption (e.g. Bicknell et al., 1997). Within this context, the turnover frequency is anti-correlated with the age of the source (a comprehensive review is given by Tinti et al., 2005). That sets the HFP sources among the youngest objects (see e.g. Baum et al., 1990).

Concerning the physical relation between those three groups of sources one could make the crude approximation that they are evolutionary stages of the same class. Specifically, HFPs age to pass through the GPS and CSS stage till they finally end up becoming lower luminosity FR 1 radio sources (e.g. Dallacasa et al., 2000). This idea is supported by the discovery that there is an anti-correlation between the turnover frequency and the linear projected size of the sources at least in case of symmetric objects (e.g. Fanti et al., 1990; Snellen et al., 2000). This finding combined with the findings of kinematic studies (e.g. Polatidis and Conway, 2003) allows the construction of a very self-consistent picture. In particular, assuming the source to be expanding at a constant pace induces that the higher the turnover frequency the younger the object is (e.g. Fanti et al., 1995).

The last conclusion has been reached under several assumptions. Nevertheless, if true it immediately implies the importance of the HFP research since they can under those assumptions provide us with an excellent probe of the early stages of radio activity and evolution. Especially, they provide the opportunity to probe the physical conditions and the environment of radio sources.

6.3 Searching for GPS and HFP sources

The discussion in section 6.2 has hopefully made clear the importance of the study of GPS and especially HFP sources. In brief, they comprise one of the few means available in the exploration of the early evolutionary stages of radio galaxies. That includes of course probing their immediate environment. Several authors like Conway (1997, 1999) have demonstrated the importance of such research.

With the most efficient possible usage of the studied sample in mind, we have consistently looked for new candidates on the basis of their radio spectrum. Admittedly this is not a trivial task. In reality, several factors such as the variability (NVSS catalog is well separated in time by the Effelsberg measurements) make easily create ambiguous detections of GPS sources. Nonetheless, there has been being detected a number of GPS candidates that are afterwards re-targeted simultaneously at all possible frequencies at Effelsberg 100-meter telescope. This is meant to identify the spectrum and reveal real GPS sources.

This is an admittedly large and time consuming project that has been allocated observing time independently. Here we attempt the summary of the work that has been done in this direction keeping in mind that this is an ongoing find.

6.3.1 The candidates

Throughout the duration of the Effelsberg-CBI project there have been conducted searches for GPS/HFP sources. Then they were re-targeted to verify their spectrum. Some candidates are shown in table 6.1. Those sources have been detected on the basis of their low-frequency spectral index $\alpha_{1.4}^{4.85}$ and mainly the high frequency one $\alpha_{4.85}^{10.45}$. In particular, they satisfy the condition that $\alpha_{4.85}^{10.45} \geq 0$ (for $S \propto \nu^{\alpha}$). As it was discussed elsewhere (see section 6.3) the GPS sources are by definition peaking around 1 and 5 GHz. The previously stated convention then favors sources that display a turnover frequency higher than the 5 GHz.

For sources that have been verified to have indeed a turnover frequency at high frequencies, there is a proposal (Angelakis et al. in prep.) for following the spectrum up to the mm regime. For all these sources the naturally following step would be to conduct mm VLBI imaging to investigate their structure.

In the next paragraphs we summarize some of the work that has been done on this direction.

6.3.2 Examples

Here we compile some spectra of sources re-targeted simultaneously at most frequencies with the 100-meter telescope after their identification as possible HFP sources. In figure 6.2 are shown only some examples of such sources. As it shown there many of the sources show an interestingly high turnover frequency being classified as HFP then.

In table 6.2 are shown the results for three interesting sources with redshift entries in the NASA Extragalactic Database (NED). As it is shown there, if the made assumptions are valid there is a population of sources worth following further starting with the investigation of their structure with high resolution imaging.

6.4 HFP 025515+0037

The current section is meant as a report of the study of an extreme example of HFP namely 025515+0037. The source exhibits a uniquely high turnover frequency that places it among the candidates for being an "infant" source in terms of radio activity. Moreover, it is highly variable as it is shown from its light curve made of data covering roughly 3 years. After exploiting the already available data we went on to initiate the measurement of its redshift, study the VLBI structure and to monitor its spectrum. All these are presented immediately.

To summarize, one could say that 025515+0037 is among the candidates of being at very early stages of its activity. As will be discussed later, very high angular resolution observations are necessary

Table 6.1: **The sources early detected as GPS/HFP candidates. The sources have been identified on the basis of their spectral indices. The selection is done so that $\alpha_{4.85}^{10.45} \geq 0$ for $S \propto \nu^{\alpha}$ that clearly favors the HFPs.**

| Source	$\alpha_{1.4}^{4.85}$	e	$\alpha_{4.85}^{10.45}$	e	Source	$\alpha_{1.4}^{4.85}$	e	$\alpha_{4.85}^{10.45}$	e
024718+0153	-0.122	0.135	0.606	0.083	145337+0017	-0.755	0.093	0.571	0.136
025528+0144	0.165	0.037	0.557	0.042	144216-0049	-0.201	0.113	0.049	0.219
025812+0122	-0.940	0.143	0.446	0.223	145147-0127	-0.710	0.064	0.175	0.096
024918+0125	-0.570	0.126	0.599	0.201	145810-0227	-0.715	0.160	1.538	0.197
023923+0105	0.512	0.036	0.194	0.092	144050-0225	0.241	0.087	0.118	0.125
024059+0049	0.318	0.140	0.215	0.173	145007-0306	-0.957	0.173	1.967	0.302
024240+0057	0.351	0.163	0.700	0.255	145144-0244	0.061	0.035	0.095	0.098
025515+0037	0.087	0.027	0.694	0.006	145005-0307	-1.377	0.144	0.417	0.257
025651+0036	-0.406	0.112	0.520	0.195	144254-0329	-0.122	0.081	0.233	0.267
025901+0053	-0.305	0.049	0.015	0.073	144539-0332	0.455	0.076	0.035	0.160
025807+0021	-0.569	0.045	0.367	0.197	144653-0337	-0.862	0.083	0.454	0.094
025333+0024	0.764	0.033	0.216	0.052	145837-0353	-1.295	0.120	1.324	0.224
024858+0019	-0.811	0.032	0.135	0.045	144138-0422	-0.475	0.164	0.710	0.351
025928-0020	0.805	0.024	0.634	0.010	143528-0451	-0.525	0.050	0.328	0.186
024002-0020	1.207	0.136	0.942	0.149	144338-0540	-1.303	0.137	0.909	0.264
024335-0055	-0.079	0.043	0.303	0.118	204248-0149	-0.535	0.029	0.151	0.071
024452-0058	-0.166	0.109	0.004	0.271	204459-0157	-0.982	0.155	0.601	0.266
024453-0109	-1.097	0.068	1.040	0.106	205749-0146	-0.195	0.153	0.149	0.213
025427-0110	-0.411	0.202	0.709	0.317	204745-0246	-0.087	0.029	0.180	0.029
024739-0153	-0.604	0.182	0.880	0.304	205824-0305	-0.315	0.040	0.421	0.229
025912-0224	-0.253	0.040	0.082	0.234	205809-0309	-0.617	0.074	0.486	0.171
025842-0225	-0.290	0.068	0.507	0.242	205755-0310	-0.576	0.153	0.767	0.220
025803-0229	-1.280	0.045	0.153	0.099	205210-0303	-0.707	0.128	0.061	0.183
025419-0225	0.624	0.050	0.520	0.023	204502-0301	-0.332	0.044	0.124	0.058
023945-0234	0.309	0.025	0.000	0.011	204336-0304	-0.581	0.129	1.578	0.194
025250-0310	0.110	0.035	0.145	0.218	204331-0302	-0.214	0.084	0.493	0.262
025658-0405	0.500	0.121	0.219	0.250	203909-0317	0.158	0.024	0.005	0.006
084441-0031	-1.270	0.118	0.180	0.311	203508-0330	0.124	0.053	0.211	0.082
085216-0013	-0.695	0.131	0.980	0.198	204635-0323	-0.638	0.158	0.291	0.255
084928-0057	-0.724	0.173	0.640	0.278	204720-0356	-0.699	0.089	0.427	0.275
084857-0139	0.006	0.070	0.009	0.260	203508-0450	0.486	0.159	0.140	0.325
084958-0229	0.162	0.089	0.197	0.153	204604-0527	-0.159	0.191	0.186	0.357
084744-0245	-0.365	0.115	0.047	0.215	204249-0518	-1.495	0.085	1.344	0.137
084235-0245	-0.913	0.090	0.487	0.148	205704-0547	-0.239	0.125	0.571	0.181
084032-0324	0.240	0.057	1.705	0.074	205658-0552	-0.685	0.042	0.077	0.259
084025-0321	0.573	0.051	0.894	0.118	205557-0615	-0.588	0.132	0.304	0.229
085212-0404	0.513	0.044	0.088	0.070	205135-0606	0.140	0.105	0.335	0.192
085559-0355	-0.064	0.078	0.892	0.130	203731-0625	0.725	0.043	0.106	0.088
					204341-0630	-0.610	0.103	0.519	0.253
					204446-0632	-0.334	0.029	0.626	0.042
					203621-0702	-0.636	0.061	0.295	0.103
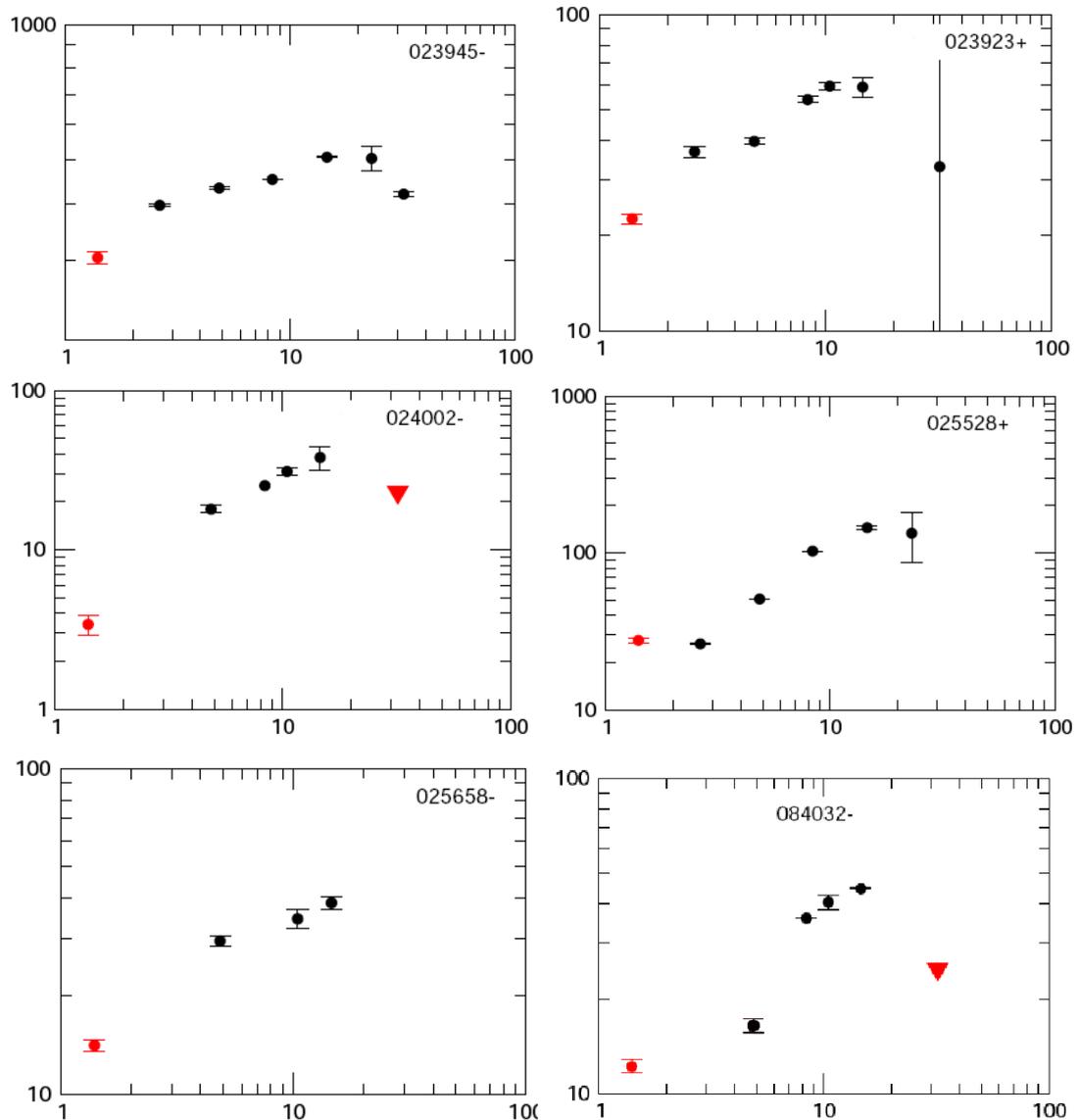
Figure 6.2: **A compilation of sources that have been identified as GPS/HFP candidates and have been re-targeted with the 100-meter telescope at Effelsberg. The x-axis is the frequency in GHz and the vertical is the flux density in mJy. The black solid circles represent simultaneous measurements. The red triangles represent upper limits. The red circles represent the non simultaneous NVSS measurements at 1.4 GHz. It is apparent that a significant number of those sources show a turnover high frequency being classified as HFPs. Note that the high frequencies often (23, 32 GHz) suffer from weather.**

Table 6.2: **Three of the sources in figure 6.2 for which there is an NED redshift entry. Here, we estimate the age of the radio activity according to the theory described in the introduction. In all these calculations we assumed $H_0 = 71$, $\Omega_{\mathrm{M}} = 0.27$, $\Omega_{\mathrm{vac}} = 0.73$.**

Source	NED RA (hh:mm:ss)	NED DEC (dd:mm:ss)	Type	z	ν_{max}(GHz)	Age (yr)
023945-0234	02:39:45.5	−02:34:41	QSO	1.116000	20	49
023923+0105	02:39:23.7	+01:05:38	G	0.008986	10	445
024002-0020	02:40:06.1	−00:20:38	QSO	1.704670	20	34
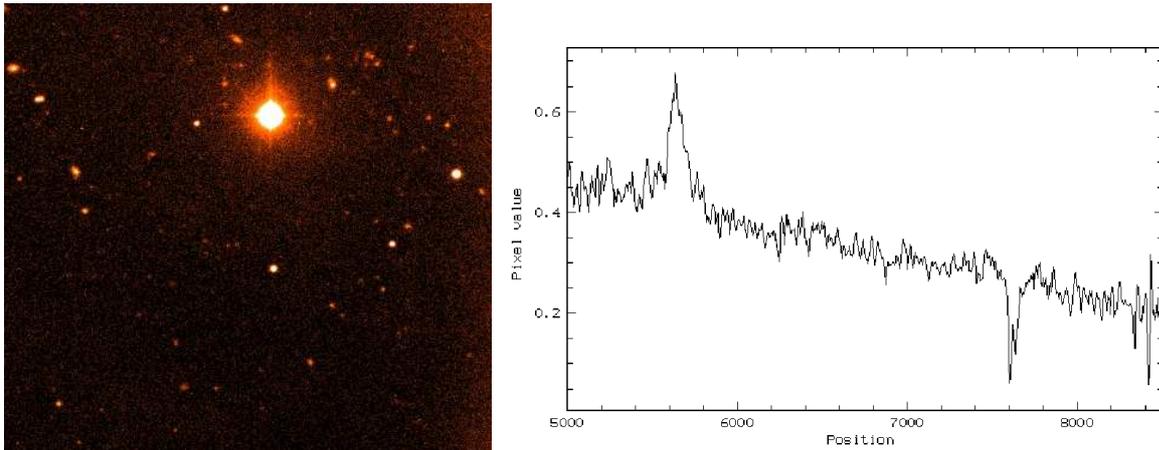
Figure 6.3: **025515+0037 in the optical band. In the left-hand side panel is shown the image of 025515+0037 in the R-band. In the right-hand side panel shown is the optical spectrum of the source with the MgII emission line at 5637Å.**

to clarify its structure and classify it as Compact Symmetric Object (CSO). If this is the case then it must be extremely young. Alternatively, it is a radio source in a flaring state. In this case a new component is expected to be seen.

6.4.1 The discovery

In the lower plot of figure 3.2 is shown the repeatability curve for the 10.45-GHz receiver. It is immediately noticeable that almost all the points lie within a moderate zone of scatter around the general trend fitted by the blue curve. Exceptional is the behavior of two data points marked with red points. One around 70 mJy and another between 1 and 2 Jy. The first point corresponds to the HFP source 025515+0037 reported here and the second one the the source NGC 1052 that is discussed later (see section 6.5). This observation immediately led to the suspicion that the corresponding source must be variable. That was proven to be indeed the case from studying its light curve (see sub-section 6.4.3).

6.4.2 The optical spectrum, redshift, classification

The knowledge of the source redshift is essential for calculations such as its brightness temperature, the expected size and so forth. Spectroscopic measurements have been done (Heidt 2006, priv. comm.) with Calar Alto 2.2-meter telescope. The spectrum is shown in figure 6.3. As can be seen there, the spectrum 0f 025515+0037 is dominated by one broad emission line at 5637 Å. This can only be MgII,

which allows the calculation of z:

$$z = 1.015 \pm 0.002 \tag{6.1}$$

The FWHM of the line in the source rest frame is roughly 38 Å. That corresponds to ∼4000 km/s classifying the source a radio-loud AGN.

At z=1.015 the distance modulus is 44.14 (in the concordance cosmology). For $m_R = 19$ and an assumed R-band extinction of 0.27 mag (NASA Extragalactic Database) the absolute brightness of 025515+0037 is $M_R = -25.12$ (i.e. the source is a Quasar).

6.4.3 The light curves
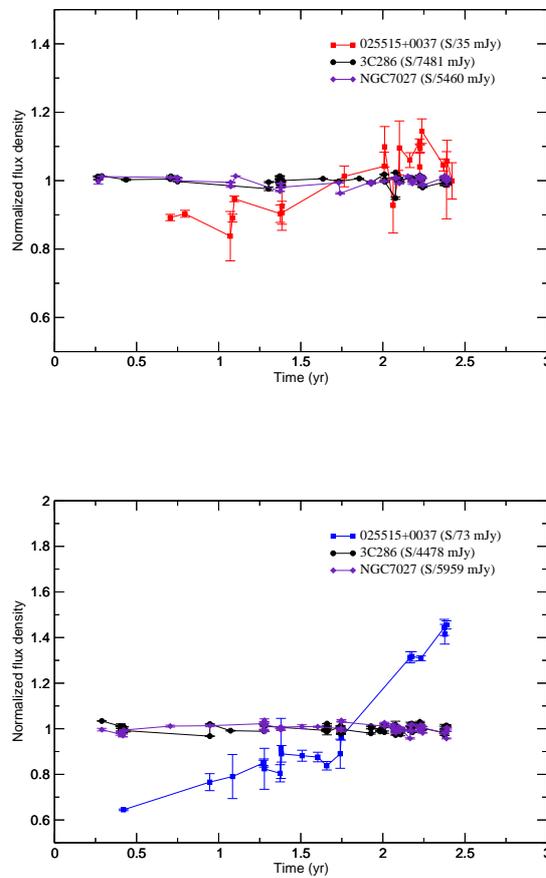
Figure 6.4: **The light curves of 025515+0037 along with that of two standard calibrators namely, 3C286 and NGC 7027 (see table 2.2.3).** *Upper panel*: **The light curve at 4.85 GHz. The peak-to-peak variation reaches 40%. Here, the** *Lower panel*: **The light curve at 10.45 GHz. Here, the peak-to-peak variation reaches 70%. In these plots the time coverage is of the order of two years.**

Since 025515+0037 happened to be among the repeaters, it has been regularly observed throughout almost the whole duration of the project. In fact, there exist light curves at both 4.85 and 10.45 GHz. These are shown in figure 6.4.

The light curves shown there cover approximately 2 years of observations. The 4.85-GHz curve appears to be noisy. This is mainly due to weather effects. On the other hand, the errors at 10.45 GHz are smaller. That is chiefly due to higher flux density that the source has at this frequency.

Despite the noisiness of the low frequency data, it is readily noticeable that the exhibits variability as has been mentioned earlier. In particular, the low frequency light curve shows a peak-to-peak variation of the order of 40% within a period of roughly two years. Even though sparse and demanding further investigation, there are indications for Intra-Day Variability (IDV, Witzel et al. 1986; Heeschen et al. 1987). For example, at $\sim$1.25 yr or $\sim$2.25 yr there is a strong evidence for rapid variability that will be examined later. So is the case for MJD$\approx$13000. At 10.45 GHz the situation is even more clear due to the better quality of data. In that case, the indication for fast variability is even more obvious although it also demands further investigation. However, the long term variability of nearly 70% is already very interesting. It indicates a radio source undergoing a flaring state as will be discussed later.

6.4.4 The brightness temperature

The flux density variability observed in 025515+0037 as shown in figures 6.4.3 can provide the ground for an estimate of the physical conditions in play at the source. In particular, under certain assumptions one can estimate its brightness temperature, $T_{\rm B}$, by measuring the variability at the turnover frequency of the spectrum $\nu_{\rm max}$, as follows.

Let us assume that the variability is intrinsic and originates at a relativistically moving sphere. Let the sphere be homogeneous (Marscher et al., 1979; Ghisellini et al., 1993), $\nu_{\rm max}$ be the turnover frequency of the radio spectrum (i.e. the frequency at which the optical depth becomes unity and $S_{\rm max}$ the corresponding flux density. The angular diameter of the source θ in mas can be approximated by:

$$\theta \leq 3.56 \times 10^{-4} \tau d_{\rm L}^{-1}(1+z) \tag{6.2}$$

where τ: the variability time scale in days
         $d_{\rm L}$:   the source luminosity distance in Gpc
         z: the redshift
         δ: the Doppler factor

That follows from light travel arguments (Marscher et al., 1979). On the other hand, the variability time scale in days, τ, is give by:

$$\tau = \frac{<S>}{\Delta S} \Delta t \tag{6.3}$$

where Δt: the time span over which the variation of flux density is measured
         ΔS: the variation of the flux density

It can be shown that $T_{\rm B}$ in K, is given by:

$$T_{\rm B} = 1.77 \times 10^{12} \frac{S_{\rm max}}{\nu_{\rm max}^2 \theta^2} \left(\frac{1+z}{\delta} \right) \tag{6.4}$$

where $S_{\rm max}$:   the maximum in the light curve
         $\nu_{\rm max}$:   the turnover frequency

As it is shown in figure and is discussed in sub-section 6.4.5, the radio spectrum of 025515+0037 displays an exceptionally high turnover frequency (30-40 GHz). Unfortunately, there are no light curves at such high frequencies available. Compromisingly, one can use the behavior at 10.45 GHz instead. Assuming then $\nu_{\rm max} =$10.45 GHz and $z = 1.015$ (see sub-section 6.4.2) and $\delta = 1$, one gets:

$$T_{\rm B} = 3.45 \times 10^{11} {\rm K} \tag{6.5}$$

where $< S >$:   73 mJy
S_{max}:   105 mJy
S_{min}:   48 mJy
Δt: 700 d

The adopted conventions are: $H_0 = 71$, $\Omega_{\mathrm{M}} = 0.27$, $\Omega_{\mathrm{vac}} = 0.73$. The inverse Compton catastrophe limiting brightness temperature of 10^{12} K computed by Kellermann and Pauliny-Toth (1969) as well as that of 3×10^{11} K computed by Readhead (1994), are comparable to the source brightness temperature. Nonetheless, one must keep in mind that the assumptions that the Doppler factor is 1 has been arbitrary. Moreover, ν_{max} is assumed to be 10.45 since it is the frequency at which the light curve is available. However, ν_{max} is apparently higher as can be seen from the observed spectrum shown in figure 6.5.

6.4.5 The radio spectrum

The light curves at 4.85 and 10.45 GHz discussed earlier indicate a source going through a flaring state. Interestingly, the radio spectrum on the other hand, leaves clues that the source may be a compact object encouraging further investigations. Let us recall the important properties of its spectrum then.
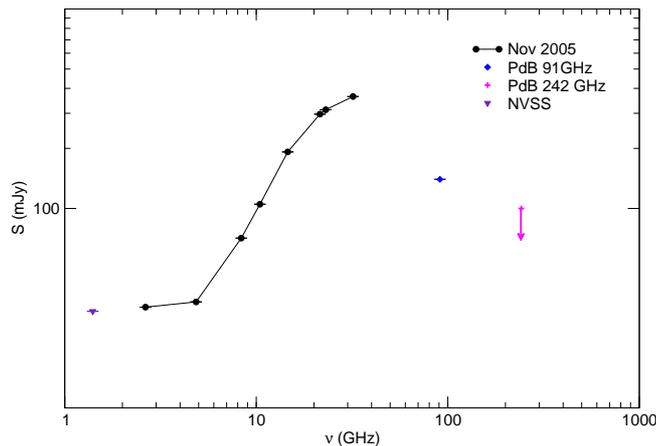
Figure 6.5:   **The radio spectrum of 025515+0037 between 1.4 and 242 GHz. The first point from the left at 1.4 GHz is taken from the NVSS catalog. The blue point is at 91 GHz measured at Plateau de Bure. So is the upper limit at 242 GHz in magenta. The rest are all simultaneous measurements (black points). This spectrum strongly suggests a source with a turnover frequency above 40 GHz. The mean spectral index between 4.85 and 32 GHz is roughly 1.2. The line connecting the points from Effelsberg is only used to make the reading more convenient and has no physical meaning. The measurements at Effelsberg were conducted in November 2005.**

Although the repeaters were selected to be mostly steep spectrum sources, 0025515+0037 happened to be an exception. Its low frequency spectral indices are rather flat or inverted. That is, $\alpha_{1.4}^{4.85} \sim 0.08$ and $\alpha_{4.85}^{10.45} \sim 0.36$ (see table 2.8). This very fact identified the source as a candidate for being a GPS or even HFP source. Subsequently therefore, the spectrum of the sources was measured simultaneously throughout the whole band covered at Effelsberg.

In figure 6.5 is shown the radio spectrum of the source. The points in black are measured at Effelsberg simultaneously. The point in violet at 1.4 GHz has been extracted from the NVSS catalog. The data in

blue and magenta at 91 and 242 GHz respectively are measured at Plateau de Bure. It must be noted that the latter is only an upper limit.

From all these data it is obvious how inverted the spectrum is between 4.85 and 32 GHz. Such an inverted spectrum is very rare among sources with similar spectra (e.g. Dallacasa et al., 2000). The shape reminds somehow of the canonical synchrotron self absorbed spectrum (figure 4.3) although the part below the turnover frequency rises with spectral index 1.2 which is very different from the theoretically expected value of 2.5 (see equation 4.7).

At first glance, the radio spectrum of 025515+0037 resembles that expected from a nearly homogeneous bulk of emitting material radiating as a synchrotron self-absorbed system. According to the current understanding of AGN that is to be expected mainly in either of two cases (e.g. Tinti et al., 2005):

1. A source in a **flaring state**. Let us assume a bulk of material being ejected in the jet. This entity will be emitting according to the synchrotron self-absorbed theory. The received then emission will consist of two parts. (a) That from the ejected component that causes the flare. This will be resembling the synchrotron self-absorbed spectrum evolving with time due to the aging of the emitting electrons. (b) The steep spectrum part coming from the jet itself. The evolution over time of the observed spectrum will be done so that the turnover frequency ν_{max} will be drifting towards lower frequencies. The flux density at ν_{max}, S_{max}, will be evolving as shown in figure 6.6.
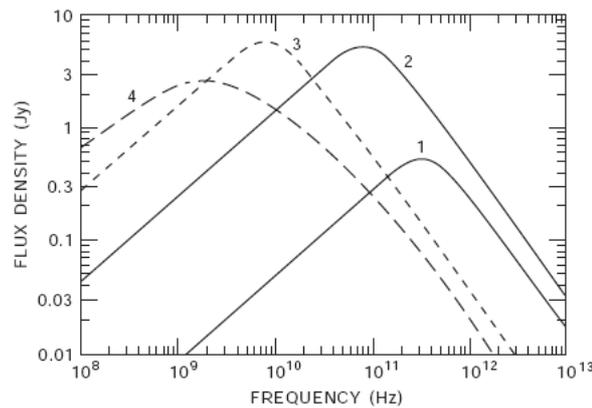
Figure 6.6: **The evolution of a flux density outburst (flare) according to Marscher and Gear (1985). The picture is taken from Zensus and Pearson (1990).**

2. **Compact Symmetric Object (CSO)**. In this case, the source consists of tow "lobes" symmetrically placed about the core. The orientation in the ideal (for observations) case is such that the axis of the ejection is parallel to the plane of the sky. The leading edges of the lobes meet the intergalactic material emitting also in a synchrotron self-absorbed fashion. In case the source is very small compared to the beam, one receives the spectrum from both the lobes. The spectrum then is not expected to change noticeably fast. This is because (contrary to the previous case) there is not emitting material that would age as in the case of a flare. The turnover frequency of the spectrum then is a measure of the source age.

In the latter, the source provides a unique opportunity to study the radio source at its very early evolutionary stages. That follows from the very high turnover frequency the source shows which, in turn, implies a very young object (see the discussion in section 6.2). In the immediately following sub-section the estimation of the radio activity age is calculated assuming that the source indeed shows a symmetric

structure. Afterwards, in sub-sections and the monitoring of the spectrum and high resolution imaging are described as means to distinguish between the flaring and the CSO case.

6.4.6 The age and the size estimate

The spectral shape in radio of 025515+0037 places it among the candidates of GPS sources exceptionally high turnover frequency namely HFPs. According to the youth scenario therefore, they are likely to be young radio sources. Thus, they provide an excellent opportunity to study the radio activity at its very first evolutionary stages.

Particularly, in the case of 025515+0037 the exceptionally high turnover frequency (30-40 GHz) implies a source extremely young and small if it is proved to be a symmetric object (see sub-section 6.4.5).

Fanti et al. (1990) first found an anti-correlation between the linear size l and the turnover frequency at the source rest frame $\nu_{max,0}$ which was later revised by O'Dea and Baum (1997) and Snellen et al. (2000) (see review by O'Dea, 1998). In particular, O'Dea and Baum (1997) found that:

$$\log(\nu_{max,0}) = -0.21\,(\pm 0.05) - 0.65\,(\pm 0.05)\log(l) \Rightarrow \nu_{max,0} \approx 0.62 \cdot l^{-0.65} \tag{6.6}$$

where $\nu_{max,0}$:   the rest frame turnover frequency in GHz
l: the projected linear size in kpc

Solving equation 6.6 for l, gives:

$$l = 0.48 \cdot \nu_{max,0}^{-1.54} \tag{6.7}$$

This is valid as long as the source is symmetric and its axis is laying on the plane of the sky. Now, if we assume that the separation of the two symmetric lobes takes place at a pace $u\,c$ then the age τ of the source in years, will be:

$$\tau = \frac{l}{u} \cdot 3.26 \times 10^3 \tag{6.8}$$

where u: the expanding speed in units of c
l: the projected linear size in kpc

Assuming the observed turnover frequency to be around $30\,(\pm 5)$ GHz and that the source is indeed a symmetric object and is expanding at a speed of $0.1\,c$ (e.g. Polatidis and Conway, 2003), the above equations will give a linear projected size:

$$l \approx 1\,(\pm 0.2)\,\mathrm{pc} \tag{6.9}$$

and an age of:

$$\tau \approx 28\,(\pm 7)\,\mathrm{yr} \tag{6.10}$$

Independently, from the interferometric measurements presented in sub-section 6.4.8 we could set limits to the size of the source. There it is discussed that the EVN observations were conducted with a resolution of about 1 mas. 025515+0037 is lying at a redshift $z = 1.015$ (see sub-section 6.4.2). At this redshift 1 arcsec corresponds to roughly 8.1 kpc and hence 1 mas to almost 8.1 pc. This estimate is in agreement of course in combination with the previous discussion shows that there would be needed a further higher resolution to reveal the source structure.

Admittedly this result is extracted on the basis of several assumptions that may very well be that not all of them are valid. Nonetheless, they at least provide clues about the order of magnitudes for the physical conditions at the source to be expected.

6.4.7   Monitoring the radio spectrum

In order to investigate the origin of the observed spectral shape and fathom the morphology of the sources, we have initiated a monitoring of the radio spectrum. If it happens so that the source is simply passing a flaring state then the turnover frequency is expected to be drifting at lower frequencies as the electrons of the emitting plasma loose their energy. Parallel to that is expected that the peak flux density of the source is decreasing. Eventually the convex in the spectrum will fade leaving behind only the synchrotron spectrum over which the flare is assuringly currently superposed. In answering the question of the morphology of the source it would be crucial to perform high angular resolution interferometry which is underway as it is discussed in sub-section 6.4.8 combined with the spectrum monitoring.
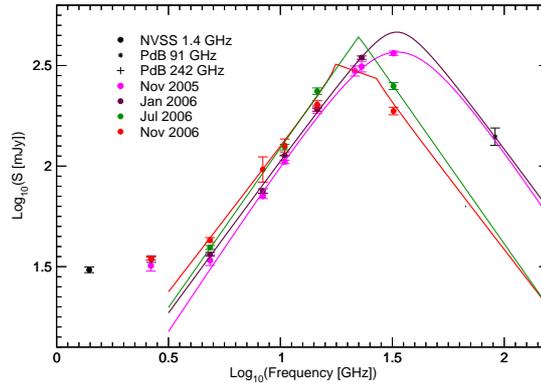
Figure 6.7:   **The "instantaneous" radio spectrum of 025515+0037 between 4.85 and 91 GHz for November 2005, January, July and November 2006. The 91-GHz measurement has been carried out at Plateau de Bure in February 2006. The fitted model is described by equation 6.11. The fitted values are shown in table 6.3. For more details see text.**

As it can be seen in figure 6.5, the spectrum exhibits a turnover frequency that is around $30\,\text{GHz}$. Assuming that the source is indeed a CSO then its age is anti-correlated with the turnover frequency of the radio spectrum. It therefore important to estimate the turnover frequency as accurately as possible. As Dallacasa et al. (2000) suggest, the spectrum can be fitted by a simple analytic expression of second order with respect to $\log(\nu)$:

$$\log(S) = a - \sqrt{b^2 + (c \cdot \log(\nu) - d)^2} \tag{6.11}$$

This expression has no physical meaning as regards the spectrum. It is only used as a convenient tool for locating the turnover frequency and estimating the peak flux density. The expression describing a homogeneous synchrotron self absorbed source can be found in Snellen et al. (1998) or Marecki et al. (1999). Equation 6.11 instead because it gives a more "solid" fit. Now, as soon as the four determining parameters have been computed, it can easily be shown that ν_{max} in GHz, will be given by:

$$\log(\nu_{\text{max}}) = \frac{d}{c} \Rightarrow \nu_{\text{max}} = 10^{\frac{d}{c}} \tag{6.12}$$

Consequently, S_{max} will be given by equation 6.11 for $\nu = \nu_{\text{max}}$.

In figure 6.7 are gathered the first results of the spectrum monitoring. The spectrum is measured "instantaneously" at Effelsberg every 2-3 months. For each spectrum the curve described by equation 6.11 is fitted to all the measured frequencies at Effelsberg apart from the $2.6\,\text{GHz}$ that is assumed to be

Table 6.3: **The parameters of the model fitted to the spectra described by equation 6.11. It must be made clear that for these fits also the 91-GHz measurements has been used.**

| Epoch	a	σ_a	b	σ_b	c	σ_c	d	σ_d	ν_{max}	$\sigma_{\nu_{max}}$	S_{max}
November 2005	2.99	0.17	0.42	0.17	1.72	0.18	2.62	0.28	33.1	13.4	372
January 2006	2.83	0.09	0.17	0.12	1.52	0.09	2.32	0.15	33.9	8.2	457
April 2006[†]	2.80	0.13	0.36	0.15	1.74	0.15	2.43	0.22	25.1	7.8	269
July 2006[*]	2.64		8.5e-5		1.58		2.14		22.4		430
November 2006	2.55	0.04	-0.10	0.09	1.44	0.05	1.90	0.07	20.9	2.6	282

[†] the 91-GHz observations from Plateau de Bure has been excluded from the fit

[*] since there are only 4 data points to determine 4 parameters the algorithm returns no errors

part of the assuringly jet background. Table 6.3 contains the results of the fit procedure. It is immediately apparent that for the shown sessions there, there has been a noticeable change in ν_{max}. Admittedly though, larger time spans must be covered in order for the drift to become prominent. It must be noted that the large variations in the computed S_{max} are a numerical artifact given the curve that we fit. The monitoring is going on but for the months between summer and fall 2006 there has been delays due to the replacement of the secondary reflector at the 100-meter telescope.

From the spectrum obtained in November 2006 there are hints that it has been rather a flare that is slowly shifting its peak frequency to lower frequencies. In any case the monitoring is ongoing.

6.4.8 The structure
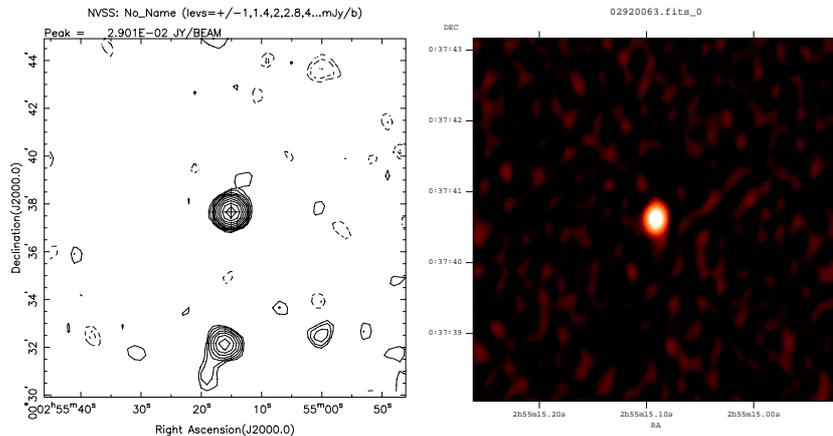
Figure 6.8: **The images of 025515+0037 with the VLA. The left-hand side image is done at 1.4 GHz with resolution of 45″. The right-hand side one is done with a resolution of 0.28″×0.19″ at 8.44 GHz and shows the central region of the left-hand side field. Still, the source is unresolved.**

Being part of the CBI-Effelsberg project 025515+0037 has been extracted from the NVSS catalog. Hence, it has been observed by VLA at 1.4 GHz with angular resolution of 45″. As it is illustrated in figure 6.8, the source appears point-like for this resolution. In the same figure is shown the the source with the same instrument at 8.44 GHz with a resolution of 0.25″×0.19″ within the context of the Cosmic

Lens All-Sky Survey (CLASS, Myers et al., 2003; Browne et al., 2003).

In June 2006 a dedicated project has been conducetd with the European VLBI Network (EVN) attempting the resolution of the source. The observations were done at 5 GHz using six antenas namely, Effelsberg, Urumqui, Torun, Shanghai, Haartebeesthoek and Westerbork. The achieved angular resolution 1.1 mas×0.8 mas. As one can see in figure 6.9 the source is still point-like i.e. its linear size is ≤ 8 pc in accordance with the HFP model. The measured flux at this frequency is 22.8 mJy/beam±1 mJy (Mòre 2006, priv. comm.).
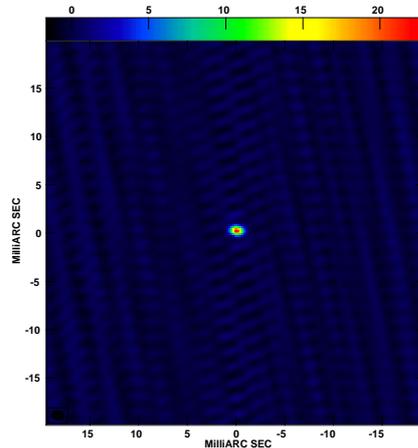
Figure 6.9: **The image of 025515+0037 with six EVN antennas (see text) at 5 GHz. The resolution 1.1×0.8 mas^2 and yet the source is unresolved (More 2006, priv. comm.).**

From this discussion it is obvious that higher resolution interferometric observations are required in order to manage resolving the structure if the source. Particularly, Global mm VLBI (GMV) measurements are necessary for revealing the nature of the source.

6.4.9 Polarization

In chapter 7 are collectively presented all the results concerning the polarization properties of all the sources in our sample. Among them also 025515+0037. As O'Dea (1998) pointed out not much is known about the polarization of GPS and HFP at high radio frequencies. At the centimeter wavelengths the polarization is very low. As is show by several studies (e.g. Pearson and Readhead, 1988; Aller et al., 1992) at around 5 GHz for instance, the polarization is a fraction of a percentile. Assuming therefore that 025515+0037 falls in this category it is not expected to show significant polarization.

In the case of 025515+0037 the study of the polarization properties are especially important. In fact it can assist the distinction between the "flaring state" and the "symmetric object" scenario discussed in sub-section 6.4.5. In the former case the ejection of a new component should be accompanied by a change in the characteristics. That follows simply from the fact that assuming the emitted components to be close to homogeneity it will be characterized by a significant degree of polarization that will change the overall source polarization properties. In the latter case they will be no divergence from the usual polarization state.

For both 4.85 and 10.45 GHz 025515+0037 appears practically completely unpolarized. The average linearly polarized flux density is less than 1 mJy which is at the level of noise. Of course that does not comprise of proof against the flaring state hypothesis. Nevertheless, it gives an indication. Ultimately the answer of the real nature of 025515+0037 will have to be revealed via high angular resolution observations.

6.4.10 Discussion

It is currently strongly believed that the study of HFPs has a great potential impact on the understanding of the extragalactic radio source physics (e.g. Dallacasa, 2003). As long as the conceptual connection assumed in the introduction (section 6.2) is valid, they are the probes to early stages of radio activity. Especially, combined with very high resolution observations this study can reveal the conditions at those environments.

025515+0037 is sitting at the high end of the turnover frequency distribution being possibly a very young object. This result is the outcome of several assumptions many of which being admittedly questionable. It is nonetheless worth the effort to take the exploration of its nature as far as possible. Besides, even if it proves that it is only a source at a flaring state it has served as a prototype for the analysis for several other candidates extracted from samples like the one exploited here.

Beyond, the importance of 025515+0037 within the context of studying the young radio source physics is its significance in the study of CMB. Recalling the flux densities at 1.4 (NVSS catalog) and that at $\sim 32\,$GHz (Effelsberg) makes clear that sources with similar characteristics but weaker by a factor of ~ 10 would have been missed by such surveys. But yet the contamination of higher frequency data would have been exceptional making the analysis of CMB data unreliable. Statistics therefore on such populations are necessary. In any case it is a rather under-studied class of objects given the bias to the centimeter wavelengths of most surveys.

6.5 NGC 1052

In sub-section it was reported that 025515+0037 had been dug up from the repeatability curves shown in figure 3.2. As it was discussed there, all the sources were lying within a a reasonable belt of noise apart from two prominent outliers. The one with flux density of the order 70 mJy was the HFP 025515+0037. The second one at the higher flux density levels (1-2 Jy) appeared to be one of the used pointing sources namely 024104$-$08. Contrary to the former case this object is an already well known and extensively studied source better known as NGC 1052. Here are gathered some results from our studies.

6.5.1 Facts

In figure 6.10 are collected some images of NGC 1052 that reveal the interesting structure of the source at different bands. As is shown in the lower-left panel there the source is an elliptical galaxy. In fact, NGC 1052 shows substantial evidence for a recent merger (e.g. Pierce et al., 2005). Due to its characteristics it provides an excellent opportunity to study the obscuring torus around a super-massive black hole (Kadler et al., 2004). That is predicted within the standard model of active galactic nuclei. Figure 6.11 shows the spectral energy distribution over several frequency decades.

Given that it happened to be among our pointing sources there are data available for the last almost three years at both 4.85 and 10.45 GHz. As it has been done in the case of 025515+0037, one can extract some useful physical parameters about the source.

6.5.2 The light curves and the brightness temperature

In figure are shown the data compiled during the Effelsberg-CBI observations (July 2003 - July 2006). There both 4.85 and 10.45 GHz are presented. In red and magenta are shown the low frequency data and in blue and violet the high frequency ones.

The peak-to-peak variations are roughly 70% and 20% at 10.45 and 4.85 GHz, respectively over an almost 3-year long period.

Similarly to the procedure followed for 025515+0037 one can compute the brightness temperature of NGC 1052. The source is at a $z = 0.005037$ (NED). Assuming $S_{\min} = 1155\,$mJy and $S_{\max} = 1730\,$mJy
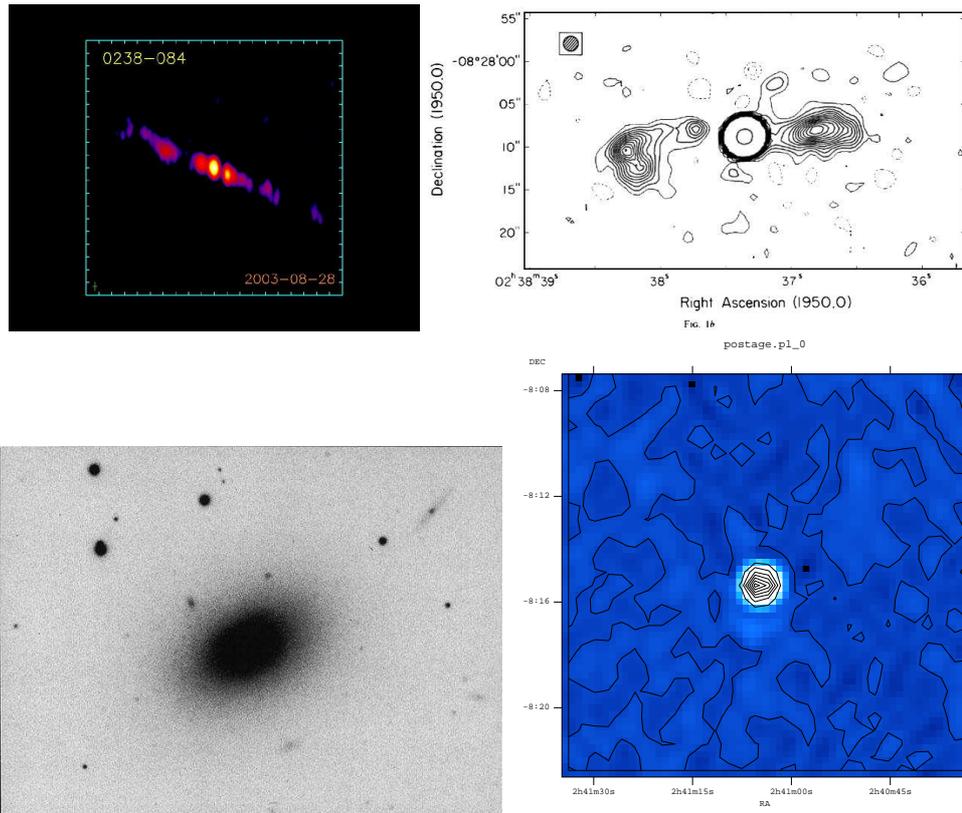
Figure 6.10:   **Images of NGC 1052 at different bands.** *Upper-left panel*: **The 15-GHz VLBA image (MOJAVE 2cm Survey, Kellermann et al., 2004; Lister and Homan, 2005).** *Upper-right panel*: **1.7-GHz VLA image (Wrobel and Heeschen, 1984).** *Lower-left panel*: **Optical image taken from Palomar.** *Lower-right panel*: **The NVSS image at 1.4 GHz with VLA.**
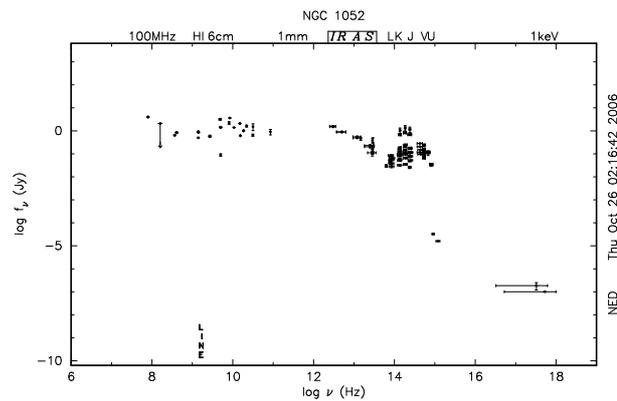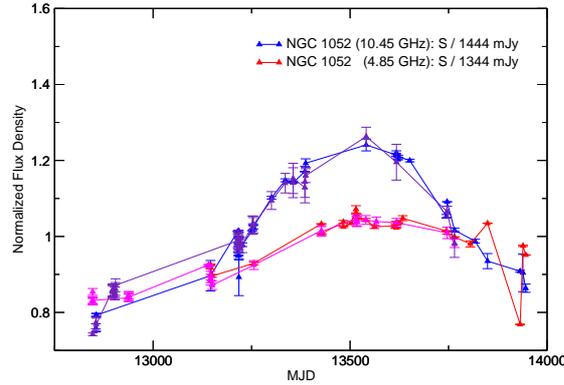

Figure 6.11:   **The spectral energy distribution of NGC 1052 throughout a substantial part of the whole spectrum. It is taken from the NASA Extragalactic database (NED).**

Figure 6.12: **The light curves of NGC 1052 at 4.85 (red and magenta points) and 10.45 GHz (blue and violet points). The peak-to-peak variations are roughly 70% and 20% at 10.45 and 4.85 GHz, respectively over an almost 3-year long period. In these light curves there are evidences even for intra-day variability (for insatnance at MJD around 14000.)**

at 10.45 GHz and a period of 1100 days and a Doppler factor $\delta = 1$ results in:

$$T_{\mathrm{B}} = 1.3 \cdot 10^{10}\,\mathrm{K} \qquad (6.13)$$

This value is only a average value giving an impression of the source energetics. Besides, as Kadler et al. (2004) showed there exist a gradient in th brightness temperature along the jet axis.

6.6 Ultra Steep Spectrum Sources / High redshift Radio Galaxies

The study of High Redshift Radio Galaxies, hereafter HzRGs, is clearly important in the understanding the formation and evolution of massive elliptical galaxies. In the case of HzRGs the light is spatially resolved allowing a clear view of the host galaxy (e.g. De Breuck et al., 1999).

Traditionally, the searches of such objects has been based on the spectroscopic studies of radio source positions with undetected optical counterpart (e.g. Kristian et al., 1974). The discovery of HzRGs has been revolutionized from the fact that the radio sources with unidentified optical counterpart tend to exhibit a steeper radio spectrum (e.g. Klamer et al., 2006).

There have been suggested mainly two effects that justify the observation that HzRGs appear with steeper spectral indices ($z - \alpha$ correlation):

1. Spectral Energy distribution characteristics of radio galaxies. It has been shown that they tend to steepen at higher frequencies. Hence, for a given frequency band the higher the redshift the higher frequency the part of the spectrum observable is and therefore the steeper.

2. The intrinsic steepening of the SED of HzRGs due to the Inverse Compton losses of the relativistic electron population on the CMB photons. Since the density of the latter is increasing proportionally to $(1 + z)^4$ (Krolik and Chen, 1991) that will result a steepening of the SED.

This method of tracing HzRGs has proved to be very efficient having revealed a significant number of such (e.g. De Breuck et al., 2004). Within the context of a constant attempt to exploit the available sample in every possible way, we have looked for such candidates as well.

Although only limited effort has so far being put in this direction, it is worth it at least mentioning our sparse findings concerning HzRGs candidates.

Generally speaking, one could explore the available sample in order to reveal such candidates in two ways. Directly, judging from the low frequency spectral index that they display ($\alpha_{1.4}^{4.85}$) among source that have of course been detected at both the frequencies used. Indirectly, by examining the flux densities and the spectral properties at frequency bands lower than that of NVSS.

From all the above it is clear that the small number of sources that appear to be of very steep spectrum comprise the candidates for being HzRGs. Following the convention often used, sources with $\alpha_{1.4}^{4.85} \leq -1.3$ have been selected. They are shown in table 6.4. To be fair, it must be made clear that this convention has been used for lower frequency samples (e.g. De Breuck et al., 2004). From the discussion in the introduction of the current section, it becomes clear that once the frequency band increases, the HzRGs will be found among the sources with even steeper spectra.

Table 6.4: **A selected sample of HzRGs candidates. The selection is done on the basis of their low frequency spectral index $\alpha_{1.4}^{4.85}$. In particular, it has set $\alpha_{1.4}^{4.85} \leq -1.3$. As it is discussed in the text though sources not detected at 4.85 GHz are already candidates of this class.**

Source	$S_{1.4}$ (mJy)	e (mJy)	$S_{4.85}$ (mJy)	e (mJy)	$\alpha_{1.4}^{4.85}$	e
024918−0227	37.4	1.5	7.3	0.8	−1.311	0.094
024912−0245	14.1	0.6	≤2.8		−1.304	0.134
085558−0303	242.2	7.3	28.9	0.2	−1.710	0.025
145828−0326	45.7	1.8	6.5	0.2	−1.570	0.039
205556−0214	333.2	11.8	65.2	0.9	−1.313	0.031
204407−0224	102.7	3.1	14.2	2.3	−1.595	0.132
204722−0303	64.3	2.0	10.8	0.2	−1.438	0.030

Additionally, such candidates can be found indirectly (without having detected them at both frequencies). In sub-section 3.3.2 (table 3.5) it was discussed that a significant percentage of sources (46%) have not been detected even at 4.85 GHz. That can, crudely speaking, be attributed to very steep spectral indices. That would correspond to HzRG sources discussed earlier. Therefore, one could retrieve data from lower frequency surveys and identify the real candidates.

All this discussion is very simplified and is based on assumptions of several sorts. In any case it can serve as fair starting point.

7. Polarization Studies

The important thing in science is not so much to obtain new facts as to discover new ways of thinking about them.

William Bragg

Abstract

The linear polarization characteristics of extragalactic radio sources are so far under-studied especially in the high frequency regime. It is however a topic of great interest not only since it can provide constraints in the emission models; also, because the polarization of such sources may contaminate the polarization properties of the Cosmic Microwave Background Radiation.

The observation of polarization is an exceptionally complicated task since there is always a percentage of such artificially introduced by the used apparatus. Since the CBI-Effelsberg project has not been designed for such studies we present the result of only scratching the surface of the matter. For rigid results to be reached especially designed projects are required.

7.1 Introduction

It has been already mentioned that the mechanism responsible for the emission from extragalactic radio sources is the synchrotron radiation. When the relativistic electron gas responsible for the radiation is contained in an ordered magnetic field, the electrons in every energy range will produce linearly polarized radiation.

In the case of optically thin emitting regions the detected radiation is the superposition of that originating throughout the line of sight. Assuming a homogenous magnetic field it can be shown (Le Roux, 1961) that the fractional linear polarization for particles with a power law energy distribution as described by equation 4.4, is given by:

$$\Pi = \frac{\gamma + 1}{\gamma + \frac{7}{3}} \tag{7.1}$$

where Π: The fractional linear polarization
           γ: electron energy spectrum index

For the typical energy distribution index of $\gamma = 2$ it follows:

$$\Pi \approx 70\% \tag{7.2}$$

Such high degree of polarization have been measured in radio lobes (e.g. Cygnus A, Carilli et al., 1989) and BL Lac objects (e.g. Gabuzda et al., 1994). In order for such high degrees of polarization

to be detected the magnetic field must sustain its homogeneity for angular scales at least as that of the resolution of the telescope. In the optically thick case on the other hand, the intrinsic degree of polarization is much smaller (Jones and Odell, 1977). In particular:

$$\Pi = \frac{3}{6\,\gamma + 13} \tag{7.3}$$

which for an energy distribution index of $\gamma = 2$, gives:

$$\Pi \approx 12\% \tag{7.4}$$

That is, the synchrotron radiation from a population of electrons in a uniform magnetic field is expected to be highly linearly polarized.

7.1.1 Parameterization of polarization

A monochromatic electromagnetic wave is in the general case elliptically polarized and can be described as the superposition of either two linear or circularly polarized components. Assuming the latter case, the wave can be written as:

$$\vec{E}(\vec{x}, t) = (E_+ \, \vec{\epsilon}_+ + E_- \, \vec{\epsilon}_-) \, e^{\mathrm{i}(\vec{k}\vec{x} - \omega t)} \tag{7.5}$$

Then, the complex amplitude will be:

$$E_\pm = a_\pm \cdot e^{\mathrm{i}\delta_\pm} \tag{7.6}$$

where $\delta_\pm$:   the phases of the two components

Under these assumptions one can describe the properties of the wave with the convenient set of the *Stokes parameters* introduced by Stokes (1852):

$$I \;\; = \;\; a_+^2 + a_-^2 \tag{7.7}$$
$$V \;\; = \;\; a_+^2 - a_-^2 \tag{7.8}$$
$$Q \;\; = \;\; 2\,a_+ a_- \cos(\delta_- - \delta_+) \tag{7.9}$$
$$U \;\; = \;\; 2\,a_+ a_- \sin(\delta_- - \delta_+) \tag{7.10}$$

The parameter I describes the total intensity whereas V describes the circular polarization and (Q,U) the linear polarization. Specifically, the measure of the linear polarization vector is given by:

$$P = \sqrt{Q^2 + U^2} \tag{7.11}$$

The angle of the polarization vector will be:

$$\chi = \frac{1}{2} \arctan\left(\frac{U}{Q}\right) \tag{7.12}$$

The uncertainty in that is calculated from the formal error distribution formula, as:

$$\sigma_\chi = 0.5 \cdot \frac{\sqrt{\sigma_Q^2 + \sigma_U^2}}{P} \tag{7.13}$$

The degree of linear polarization, by:

$$\Pi = \frac{\sqrt{Q^2 + U^2}}{I} \tag{7.14}$$

and it uncertainty will be:

$$\sigma_\Pi = \sqrt{(\sigma_P/I)^2 + (P \cdot \sigma_I/I^2)^2} \tag{7.15}$$

A very consistent description of all these matters can be found in Klein et al. (2003).

7.1.2 Faraday rotation, depolarization

Despite the high degrees of linear polarization expected in extragalactic radio sources, only very small such percentages are measured. It is believed that this is mainly due to the de-polarization of the radiation from internal *Faraday rotation*.

A linearly polarized electromagnetic wave propagating through plasma with an embedded magnetic field is subject to Faraday rotation. That is, the polarization angle changes by:

$$\Delta\chi = 8.1 \cdot 10^5 \, \lambda^2 \int_L n_{\text{e}} \, B \, \cos\theta \, dL \tag{7.16}$$

where λ: the wavelength in meters
   n_{e}:   electron number density in cm^{-3}
   B: the magnetic field in Gauss
   θ: the angle between the magnetic field and the wave direction of travel
   L: the thickness of the medium in pc

Defining the *rotation measure* as:

$$RM = 8.1 \cdot 10^5 \int_L n_{\text{e}} \, B \, \cos\theta \, dL \tag{7.17}$$

one can write the polarization angle after the Faraday rotation as:

$$\chi(\lambda) = \chi_0 + RM \cdot \lambda^2 \tag{7.18}$$

The Faraday rotation can result in *de-polarization*. When observing an optically thin medium polarized emission from different depths is superposed. Radiation originating at different depths though, is experiencing different degrees of Faraday rotation. The observed radiation then is the integral of differently Faraday rotated polarization vectors that result a de-polarization of the signal.

7.2 Müller calculus: Removing the instrumental polarization

Generally, when a beam of light, initially in a polarization state $\vec{S}_{\text{real}}$, passes through an optical element M it is inevitably imposed some instrumental polarization and comes out in a new state $\vec{S}_{\text{obs}}$. The influence of the element M can be described by a 3×3 matrix (ignoring circular polarization, i.e. Stokes V) namely the *Müller matrix* **M** so that:

$$\vec{S}_{\text{obs}} = \mathbf{M} \cdot \vec{S}_{\text{real}} \tag{7.19}$$

This formalism was introduced in 1943 by Hans Mueller. For our purposes, **M** can be decomposed into a time-dependent part **P** and a constant part **T**. The former describes the effect of the change in the parallactic angle of the source and the latter the instrumental effects (e.g. Turlo et al., 1985). It can be written then:

$$\vec{S}_{\text{obs}} = \mathbf{T} \cdot \mathbf{P} \cdot \vec{S}_{\text{real}} \Rightarrow \begin{pmatrix} I_{\text{obs}} \\ Q_{\text{obs}} \\ U_{\text{obs}} \end{pmatrix} = \begin{pmatrix} t_{11} & t_{12} & t_{13} \\ t_{21} & t_{22} & t_{23} \\ t_{31} & t_{32} & t_{33} \end{pmatrix} \cdot \begin{pmatrix} 1 & 0 & 0 \\ 0 & \cos 2q & \sin 2q \\ 0 & -\sin 2q & \cos 2q \end{pmatrix} \cdot \begin{pmatrix} I_{\text{real}} \\ Q_{\text{real}} \\ U_{\text{real}} \end{pmatrix} \tag{7.20}$$

where t_{ij}:   the instrumental polarization elements
   q: the parallactic angle

Hence, the computation of the "real" polarization state vector $\vec{S}_{\text{real}}$ of the source can be computed by solving equation 7.20 provided that the matrices **T** and **P** are known. In that equation the parallactic angle q is known and therefore, **P** is known. The determination of **T** on the other hand is not as trivial.

The matrix **T** is determined on the basis of observing some standard sources (calibrators) of known polarization state for several different parallactic angles. Under those circumstances, the standard sources are observed repeatedly at different parallactic angles so that the whole (Q, U) space is covered. For each measurement, the vectors $\vec{S}_{\mathrm{real}}$ and $\vec{S}_{\mathrm{obs}}$ of equation 7.20 are known. So is the matrix **P**. Consequently, **T** can be termined. Apparently the more available observations of the calibrators there are the more accurate the determination of **T** is. The details of this procedure are described by Kraus (1997); Kraus et al. (2003).

The assumed linear polarization characteristics of the calibrators are shown in table 7.1 (Kraus, priv. comm.). In fact, 3C286 is used as the main reference source. That is because its high galactic latitude ($80.7°$) implies small Faraday rotation in the interstellar material and subsequently more stable polarization characteristics.

Table 7.1: **The standard polarization state assumed for the used calibrators.**

| Source | 4.85 GHz | | | 10.45 GHz | | |
	S (Jy)	Π (%)	χ (deg)	S (Jy)	Π (%)	χ (deg)
3C286	7.48	11.0	33.0	4.45	11.7	33.0
3C48	5.48	4.2	106.6	2.60	5.9	115.9
3C161	6.62	4.8	122.4	3.06	2.4	93.8
NGC 7027	5.48	0	-	5.92	0	-

Once the instrumental polarization has been determined the "real" polarization parameters can be calculated by solving equation 7.20 for $\vec{S}_{\mathrm{real}}$ after inserting the matrices **T** and **P**. The polarization degree will then be given by equation 7.14 and the polarization angle by 7.12.

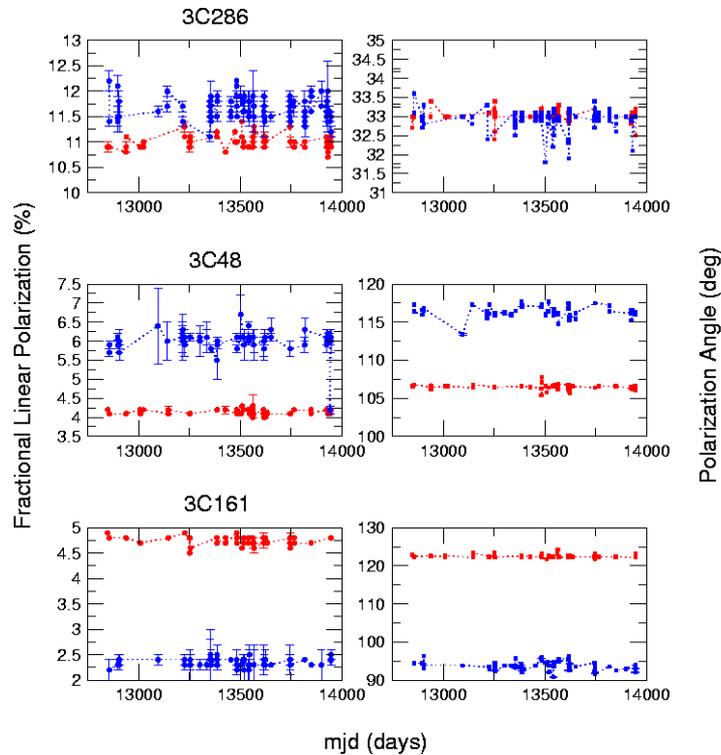## 7.3 The polarization of the calibrators and the "repeaters"

From the previous discussions it is clear that the instrumental polarization is better determined when the number of standard sources is larger or more observations of the same standard source are available. That is simply because the coverage of the (Q, U) space is better resulting a large number of equations of the form 7.20 that assist the calculation of all the elements of matrix **T**, t_{ij}.

The need of having often measurements of standard sources (polarization calibrators) immediately reveals a problem inherit in our project. In sub-section 2.1.4 it was explained that the a calibrator is observed every, roughly, six hours. That implies that the determination of the instrumental polarization is only rarely accurate. That is, only in cases of long observing sessions during which the calibrators have been measured repeatedly. It would be ideal if more sources could be used as standards in the computation of the instrumental polarization. Good candidates for that would also be those "repeaters" that show linear polarization.

For both, the main calibrators and the repeaters one can aquire a impression of their polarization state on the basis of their statistics since they have been observed repeatedly throughout the whole observing period. It is worth therefore having a closer look at those results. This will also be the first result of our work in this direction to be presented.

7.3.1 The polarization of the calibrators

To begin with, assuming the polarization characteristics of table 7.1 it would be interesting to see how they repeat throughout the long term period of the CBI-Effelsberg observations. Figure 7.1 illustrates the

Figure 7.1: **The polarization characteristics of the four main calibrators as a function of time. The covered period is of the order of three years. On the left-hand side column are the plots of the polarization degree. On the right-hand side one are the polarization angle ones. The red data points correspond to 4.85-GHz measurements and the blue ones to the 10.45-GHz measurements.**

findings for all the four major calibrators observed. The covered span is of the order of 3 years. The red color represents the measurements at 4.85 GHz and the blue indicates the 10.45-GHz measurements.

The data presented in figure 7.1 provide us with the opportunity to study the behavior of the system since the polarization satte of these sources is assumed consnat (especially for 3C286). Table 7.2 includes all the polarization characteristics averaged over all available data points (roughly three years of observations). It can immediately be seen there that the polarization characteristics of those sources are very stable. Comparing the data in tables 7.1 and 7.2 makes clear that within the errors they are identical. Besides, from figure 7.1 it is clear that there is no apparent systematic effect. Given the substantial time of the current work been invested in technical details, it is irresistible to the author to mention the difference in the noisiness of the data between the two receivers. From those plots it is clear that the high frequency observations are largely more noisy than the 4.85-GHz ones. That is of course partly attributable to the weather to which the 10.45-GHz measurements is more sensitive. Provided though that the channels delivering the Stokes parameters Q and U are correlation channels supports the idea that the 4.85-GHz receiver is more stable itself (whcih is the case). That is because the correlation procedure results better removal of the atmospheric effects.

Table 7.2: **The measured polarization characteristics of the calibrators averaged over all available data points.**

Source	4.85 GHz				10.45 GHz			
	$< \Pi >$ (%)	σ (%)	$< \chi >$ (deg)	σ (deg)	$< \Pi >$ (%)	σ (%)	$< \chi >$ (deg)	σ (deg)
3C286	11.0	0.1	33.0	0.2	11.6	0.2	32.9	0.3
3C48	4.2	0.1	106.5	0.3	6.0	0.3	116.3	0.7
3C161	4.7	0.1	122.6	0.4	2.3	0.1	93.7	1.2
NGC 7027	< 0.05	-	-	-	< 0.05	-	-	-

7.3.2   The polarization of the "repeaters"

Here we summarize the results concerning the polarization of the repeaters. The main benefit of such a study is the discovery of sources that could possibly serve as new polarization calibrators.

In table 7.3 are gathered the polarization characteristics of a number of repeaters that showed significant polarization. Some of them are too weak to give reliable measurements at 10.45 GHz. It must be kept in mind that their majority are steep spectrum sources. In this table are shown the flux densities and the polarization characteristics (the fractional polarization Π and the polarization angle χ), averaged over all the available data points with statistical errors. In fact, only data points of very high signal-to-noise ratio (SNR) have been used. In particular, for the total power measurements only points with SNR larger than 7 have been used whereas for the polarization P, values larger than 5 have been demanded. As one can see there, within the bound of errors the polarization angles do not change significantly between 4.85 and 10.45-GHz measurements. This is very likely due to the fact that those sources being selected from the CBI-Effelsberg are lying at high galactic latitude. Hence, the Faraday rotation is small.

From table 7.3 one can estimate the overall median values for the polarization degree, admittedly though, on the basis of extremely small number statistics. Nevertheless, the median polarization degree at 4.85 GHz appears to be 4.5 % with a median error 0.6 %. For the high frequency Π is 6.45 % with a median error 1.0 %.

7.4   The polarization of the 6000 sources

The study of the polarization parameters of the target sources is of great interest even through the statistical approach. For example Klein et al. (2003) point out several interesting topics to be studied. For instance, the investigation of the possible correlation between the spectral index and the polarization parameters is one of them (e.g. Ricci, Prandoni, Gruppioni, Sault and De Zotti, 2004). Moreover, it is expected that there is a correlation of the polarization degree and the source redshift (e.g. Mesa et al., 2002). Further, as it has often been mentioned throughout this work, these data can be utilized for estimating their influence on the CMB characteristics. In this particular case the polarization of the CMB (e.g. Kovac et al., 2002).

However, it must be borne in mind that the currently discussed results comprise only a by-product of the whole project. In fact, the currently discussed project was clearly designed on the basis of a urgent time efficiency. It is therefore clear that the polarization result have somewhat higher errors compared to the toatal power ones. Nonetheless, these resukts give some indication for the polarization behavior in this extended sample.

Table 7.3: **The measured polarization characteristics of those repeaters that exhibit signifficant degree of linear polar-
ization in either observing frequency. Sources with hyphen in their polarization data do not appear to be polarized at
the corresponding frequency or they are too weak to allow reliable polarization measurements.**

	4.85 GHz			10.45 GHz		
Source	$< S >$	$< \Pi >$	$< \chi >$	$< S >$	$< \Pi >$	$< \chi >$
	(mJy)	**(%)**	**(deg)**	**(mJy)**	**(%)**	**(deg)**
024137−0647	215±4	6.4 ±0.6	98.6 ±4.4	92 ±3	8.7 ±1.0	94.4 ±8.1
024747+0131	74 ±2	11.1±1.3	119.8±1.9	30 ±2	11.2±5.6	130.5±12.2
025341+0100	137±3	8.3 ±0.7	77.9 ±1.4	52 ±2	10.1±1.8	70.0 ±14.2
084709−0047	22 ±1	14.6±1.3	14.7 ±2.0	9 ±2	-	-
085509−0715	421±2	1.0 ±0.2	166.7±2.4	197 ±4	-	-
085537+0312	215±7	1.6 ±0.3	153.3±3.1	101 ±4	3.2 ±1.3	141.4±14.2
144839+0018	569±7	3.2 ±0.1	45.3 ±1.2	251 ±8	4.2 ±0.7	40.8 ±3.4
145421−0016	34 ±1	4.5 ±0.8	93.6 ±2.7	17 ±2	-	- ±-
145510−0539	315±4	2.4 ±0.1	86.6 ±1.3	145 ±4	3.8 ±0.9	74.3 ±10.3
145548−0037	36 ±2	3.2 ±0.4	29.6 ±4.2	19 ±2	-	-
205001−0249	91 ±5	6.0 ±1.8	170.4±1.1	46 ±2	-	-

7.4.1 Median polarization

Using the main calibrators as the standard for the determination of the instrumental polarization we
have calculate the linear polarization of the target sources. Then we selected a small fraction of sources
(roughly 280 at 4.85 GHz, calibrators are not included) that are characterized by very large SNR for both
total power and polarized intensity. In particular, SNR larger that 7 has been demanded for the former
and larger than 5 for the latter. This un-uniformity can be justified by the fact that the Stokes parameters
Q and U are delivered by correlation channels that are expected to have a better atmospheric subtraction.
Hence, the polarized intensity is expected to be more reliable. It must always be kept in mind that the
major part of the data analysis has been always kept as automatic as possible. That is why so often very
pessimistic conventions have been done.

Under these assumptions the median fractional polarization at 4.85 GHz appears to be roughly:

$$\Pi_{4.85} \approx 4.7\% \tag{7.21}$$

with a median error:

$$\sigma_{\Pi,4.85} \approx 0.4\% \tag{7.22}$$

This number is rather high. Klein et al. (2003) for example calculate a value of 4.1 ± 0.3 % for the same
frequency that agrees with these values within the errors. This number is calculated for all the sources in
their sample independently of the spectral index. For the steep spectrum ones on the other hand they find
a median polarization degree of roughly 5.2 ± 0.3 %. In any case our sample is definitely not complete.
Therefore, the comparison is rather rough. Rudnick et al. (1985) report that the overall median value for
the frequency range between 1.4-90 GHz is ~ 2.5 %, significantly lower than our values. So is the case
of other works by Okudaira et al. (1993); Aller et al. (1999).

At 10.45 GHz a sample of roughly 90 sources characterized by the same SNR thresholds as before

has been examined. The median fractional polarization then is:

$$\Pi_{10.45} \approx 3.7\% \qquad (7.23)$$

with a median error:

$$\sigma_{\Pi,10.45} \approx 0.4\% \qquad (7.24)$$

This value is definitely contradicting that in equation 7.21. Generally, it is expected that the higher the frequency the higher the fractional polarization. That follows easily from the fact that the Faraday rotation is a decreasing function of frequency. Nevertheless the latter value is in good agreement with the work by the authors mentioned earlier that are mostly based on complete samples.

7.4.2   Polarization as a function of spectral index

On the basis of the argument that the steep spectrum sources are generally less compact than the the flat spectrum ones, it is in turn expected that the steep spectrum source must exhibit a larger fractional polarization than those of flat spectrum (Ricci, Prandoni, Gruppioni, Sault and De Zotti, 2004). It is worth investigating whether this is indeed the case.
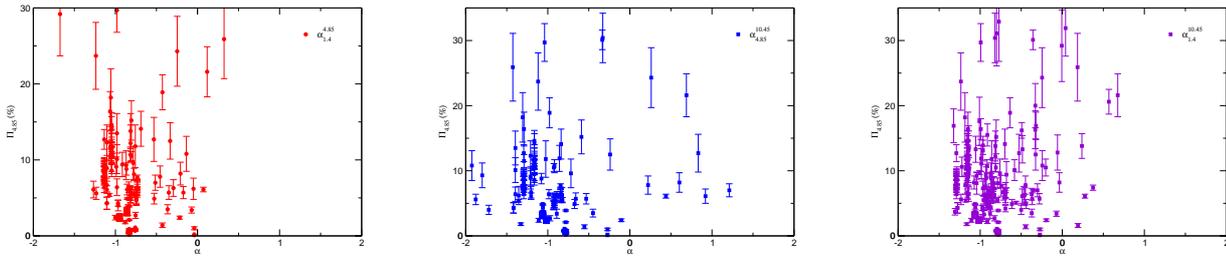
Figure 7.2:   **The fractional polarization at 4.85 GHz as a function of spectral index. In red is the spectral index between 1.4 (NVSS) and 4.85 GHz ($\alpha_{1.4}^{4.85}$). In blue is shown the spectral index between 4.85 and 10.45 GHz and in violet is shown the spectral index from 1.4 to 10.45 GHz as calculated by the Least Square Fit method.**
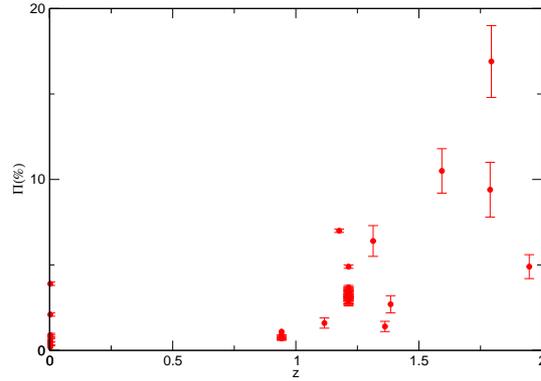
In figure 7.2 is plotted the fractional polarization at 4.85 GHz as a function of the spectral index. In fact, in that plot all three spectral indices have been used, namely $\alpha_{1.4}^{4.85}$, $\alpha_{4.85}^{10.45}$ and $\alpha_{1.4}^{10.45}$. Contrary to what Ricci, Prandoni, Gruppioni, Sault and De Zotti (2004) find concerning the polarization degree at 18.5 GHz and the spectral index $\alpha_5^{18.5}$ we detect no clear correlation. Again, this may be due to biases in our sample.

7.4.3   Polarization as a function of redshift

Ricci, Prandoni, Gruppioni, Sault and De Zotti (2004) suggested that there is a correlation between the polarization degree and the redshift. They argue that an increase in the fractional polarization with frequency as expected in the case of a Faraday screen at the source can be translated into a positive correlation of Π with redshift. That follows naturally considering that the apparent rotation measure RM_{obs} of a source with intrinsic rotation measure RM_{intr}, is:

$$RM_{obs} = RM_{intr} \cdot (1+z)^{-2} \qquad (7.25)$$

Now, assuming the existence of a Faraday screen at the source, the observed fractional polarization is inversely proportional to the rotation measure. For a source with observed RM_{obs} the inferred Π_{obs} will

Figure 7.3: **The fractional linear polarization at 4.85 GHz as a function of for a very small number of sources ($\sim$80).**

be scaling with redshift as:

$$\Pi_{\mathrm{obs}} \propto (1 + z)^{+2} \tag{7.26}$$

In figure 7.3 is plotted this relation for a small number of sources for which there is a redshift available. Interestingly, it seems that there is indeed such a behavior. This is at least qualitatively in agreement with the idea of Ricci, Prandoni, Gruppioni, Sault and De Zotti (2004).

They state that they have not found a significant correlation. It is noteworthy though that Mesa et al. (2002) suggested that a null correlation imply a relation between the intrinsic polarization degree and radio luminosity.

Nevertheless, it is beyond any doubt how interesting this whole issue is. To be fair, it is clear that the investigation of linear polarization properties of the sample of our target sources is not very reliable due to the lack of polarization-focused design.

A. Theoretical material

A.1 Radiative transfer in the terrestial atmosphere

Assume a source of specific intensity $I_\nu(0)$ observed through the atmosphere which both emits and absorbs radiation (for a full description see e.g. Kraus (1986) see figure A.1). A volume element of length dr will absorb part of the incident intensity that depends on its absorption coefficient κ_ν. It also contributes some intensity depending on its emission coefficient ϵ_ν. The total change in I_ν, dI_ν, due to the presence of the volume element dr, will be given by:

$$dI_\nu = -\kappa_\nu \cdot I_\nu \cdot dr + \epsilon_\nu \cdot dr \Rightarrow \frac{dI_\nu}{dr} = -\kappa_\nu \cdot I_\nu + \epsilon_\nu \tag{A.1}$$

where I_ν: specific intensity at the position of the volume element dr
  κ_ν: absorption coefficient
  ϵ_ν: emission coefficient

The absorption coefficient can be expressed in terms of optical depth since:

$$\tau_\nu = \int_0^L \kappa_\nu dr' \Rightarrow d\tau_\nu = \kappa_\nu dr \tag{A.2}$$

Because of equation A.2 and the *source function* definition $J_\nu = \epsilon_\nu/\kappa_\nu$, equation A.1 can be written:

$$\frac{dI_\nu}{d\tau_\nu} = J_\nu - I_\nu \tag{A.3}$$

This is the *equation of transfer* which happens to be differential equation of Leibnitz's form. For the initial condition $I_\nu = I_\nu(0)$ the solution will be:

$$I_\nu = I_\nu(0) \cdot e^{-\tau_\nu} + e^{-\tau_\nu} \cdot \int_0^{\tau_\nu} e^{\tau_\nu'} \cdot J(\tau_\nu') \cdot d\tau_\nu' \tag{A.4}$$

where $I_\nu(0)$: The intrinsic specific intensity of the source

In case the source function J is independent of the optical depth (ie $\partial J/\partial \tau_\nu = 0$), the last equation can be written as:

$$I_\nu = I_\nu(0) \cdot e^{-\tau_\nu} + J \cdot \left(1 - e^{-\tau_\nu}\right) \tag{A.5}$$

Having calculated the intensity then one can work out the flux density, by:

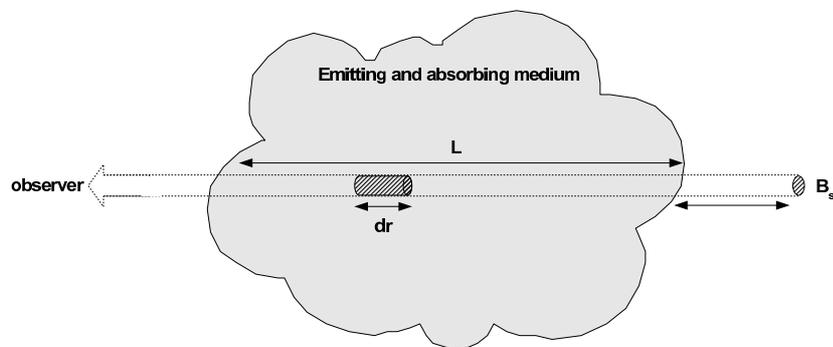$$S = \int\int I_\nu(\theta, \phi)\, d\Omega \tag{A.6}$$

Figure A.1: **Radiative transfer in earth's atmosphere. The question is: what would be the brightness of a source of intrinsic brightness B_s after its radiation has traveled through a medium that both emits and absorbs radiation. Each volume element $d\tau$ of height dr absorbs a part $-BK\rho\,dr$ of the radiation and adds a part $\frac{j}{4\pi}\rho\,dr$ where B is the brightness at the position of the volume $d\tau$.**

B. Technical material

Here are gathered some pieces of information that may possess some practical interest relative to the rest of the text. It is attempted to be kept as short as possible.
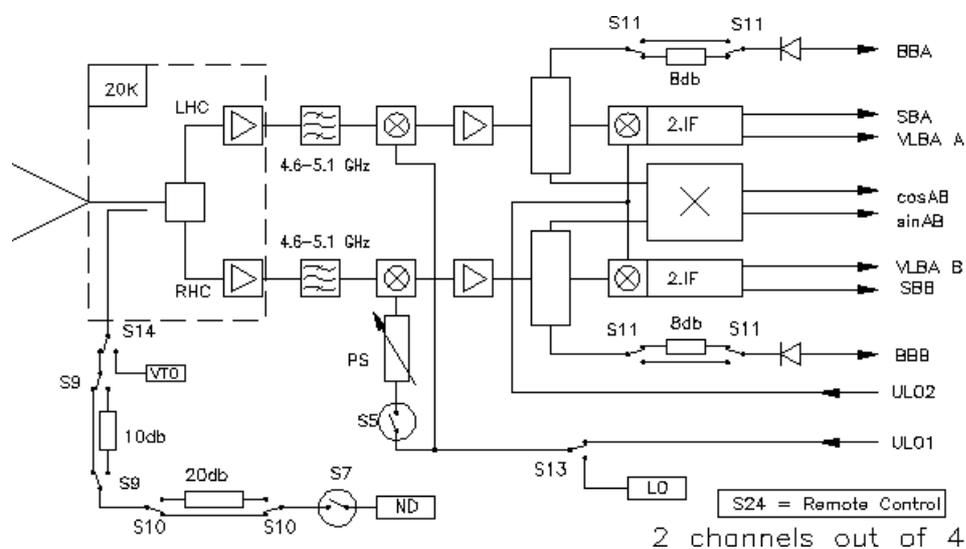
B.1 Receivers

Figure B.1: The block diagram of the 4.85 GHz receiver. It is mounted in the secondary focus of the 100-meter telescope at Effelsberg.

In figures B.1 and B.2 respectively can are shown the block diagrams of the 4.85 and 10.45-GHz multi-beam receivers used at Effelsberg.

B.2 The *cal* problem

Here we attempt to track the reason that causes the instabilities of the noise diode signal. As it has already being discussed the noise diode appears to be unstable in short time scales and long ones. Here a somewhat more detailed discussion on the matter is done.

Intra-scan peculiarities. The problem and its solution.

The intra-scan stability of the noise diode signal is especially important when low flux density levels are attempted. As it is illustrated in figure B.3, the diode signal can vary significantly and in several fashions.

The most often case is analytically shown in figure B.4. There, the case where the calibration signal shows a sudden short-lasting increase in its power is presented. 12 consecutive observations show that the power "step" is drifting within the scan. These example are already enough to show that according to
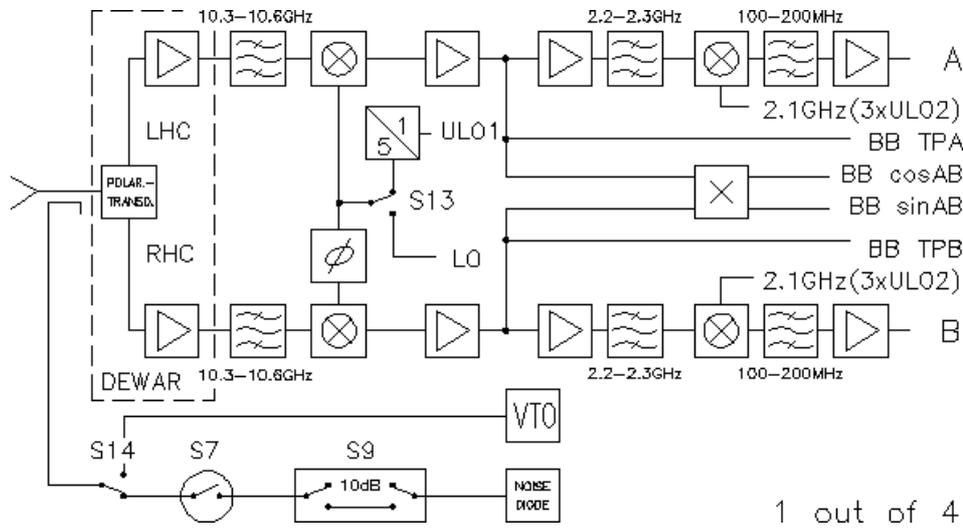
Figure B.2:   **The block diagram of the 10.45 GHz receiver. It is mounted in the secondary focus of the 100-meter telescope at Effelsberg.**
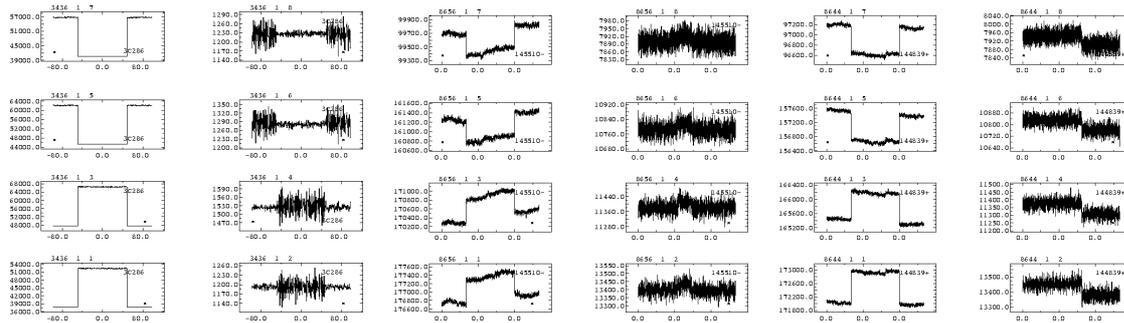

Figure B.3: Some of the most often appearing irregularities in of the noise diode signal. Here three scans are presented. Each row corresponds to one channel. Each left-hand side column corresponds to the astronomical signal (sig) and each right-hand side column to the calibrations signal (cal).

the phase in the scan that the "step" appears it may either hide a detection (when the step appears in on sub-scan) or fake a detection (when its appears in the off sub-scan). This is expected from the calibration method as reviewed in sub-section 2.1.1 where the it is described as essentially a comparison between two signals. Apparently, this can prove severe especially when weak sources are measured (a few mJy). In figure B.5 it is presented an example of highly distorted data due to wrong primary calibration. There, the data calibrated according to the "traditional" way (point-by-point) as well as the non-calibrated ones are presented. It is obvious that from the calibrated data the detection is uncertain whereas it becomes unambiguously clear from the the raw data (non-calibrated).

All these features are independent of the observing frequency and they are basically harmless when very strong sources are measured (a few hundred mJy). Given that a significant portion of currently reported sample consists of weak sources, these issue become of outstanding importance.

The way we have adopted to overcome the problem is to use one calibration signal per scan instead of calibrating the data in a point-by-point basis. That is, for each scan the average of the *cal* signal ($\langle cal \rangle$) is measured in counts and then substituted in equation 2.4. Admittedly this introduces other uncertainties since only average values are used. Nevertheless, experience shows that this way a high level of stability is achieved as figure B.5 clearly indicates. Two important assumptions implicit here are (a) that the receiver is stable for the duration of the sub-scan and (b) that the diode signal does not change significantly from sub-scan to the next within the duration of a scan. Both assumptions are basically valid.

Inter-scan peculiarities.

Having successfully dealt with the intra-scan irregularities is only half way to resolving the calibration signal problems. Further issues arise from the long term, inter-scan, variation of $< cal >$. In figure B.6 are gathered some plots illustrating how $< cal >$ changes over the observing session. There, for each session both the data for the 4.85 and th 10.45 GHz receiver are presented. Generally, the observed variation are confined to less than 2 %. This is very satisfactory already. However, in exceptional cases there have been detected variations that reach several percent (can reach 10%). In such cases further action should be taken. For instance, during an Intra Day Variability experiment usually a group of sources are repeatedly measured for detection of change in their flux density of a few percent. Hence, in deciding whether any detected variation is real one must rule out the case of *cal* variations. For that particular case the instability problem could be resolved in two steps:

1. Calculate the $< cal >$ for every scan

2. Remove the trend described by $< cal >$ as function of time

Excluding any other factor, any remaining variability must then be attributed to anything but the system. For the current project no further processing of the data has been carried out. The calibration signal is monitored and restricted to 2-3 % in terms of RMS. Cases of larger RMSs are flagged as "bad" and repeated.

A clear dependence on the ambient temperature is indicated in the plots of figure B.6 via the dependence on the UT. At the moment of the current manuscript preparation it is still unclear what is this behavior originating from. Refers to the next paragraph for a brief discussion on this matter.

It is noteworthy that each channel's behavior is independent of that of the others as is shown from the *cal* behavior. As shown in B.6 it is often that the *cal* signal behaves totally differently in different channels due to the fact that each channel is routed through independent systems. For example, in the bottom right plot of that figure all four channels decrease smoothly with increasing UT time but with slopes. That is indicative of different sensitivity to temperature of different channels. Those facts, make even more urgent the need for calibrating each channel independently.
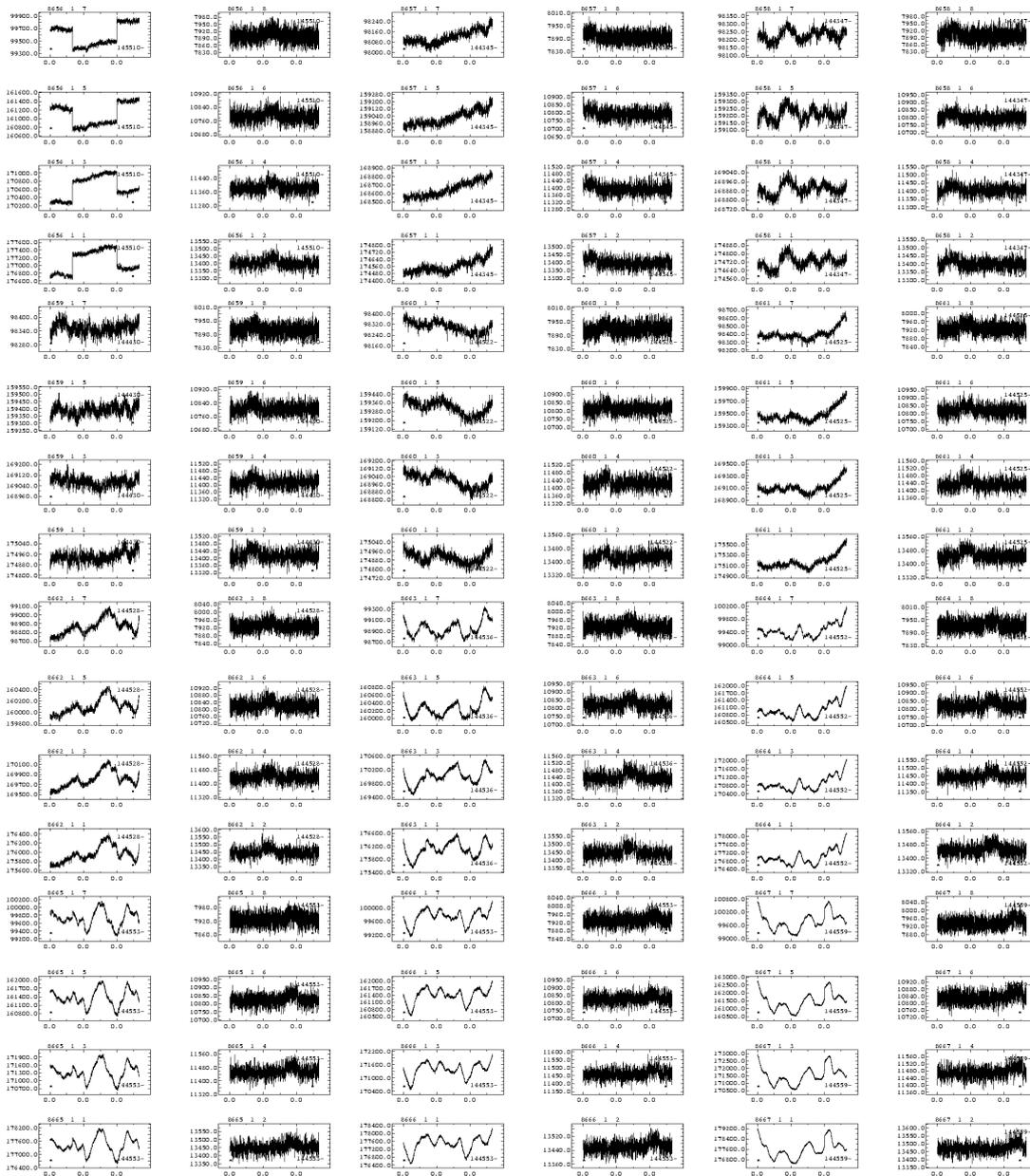
Figure B.4: **The most common case of problematic calibration signal. Here 12 consecutive observations at 10.45 GHz are plotted. The scan number is printed on the top left corner of each frame. The left column and from bottom to top is the astronomical signal before calibration (in counts) for channels A, B, E and F, respectively. The column on the right hand side shows the corresponding calibration signal also in counts for each channel.**
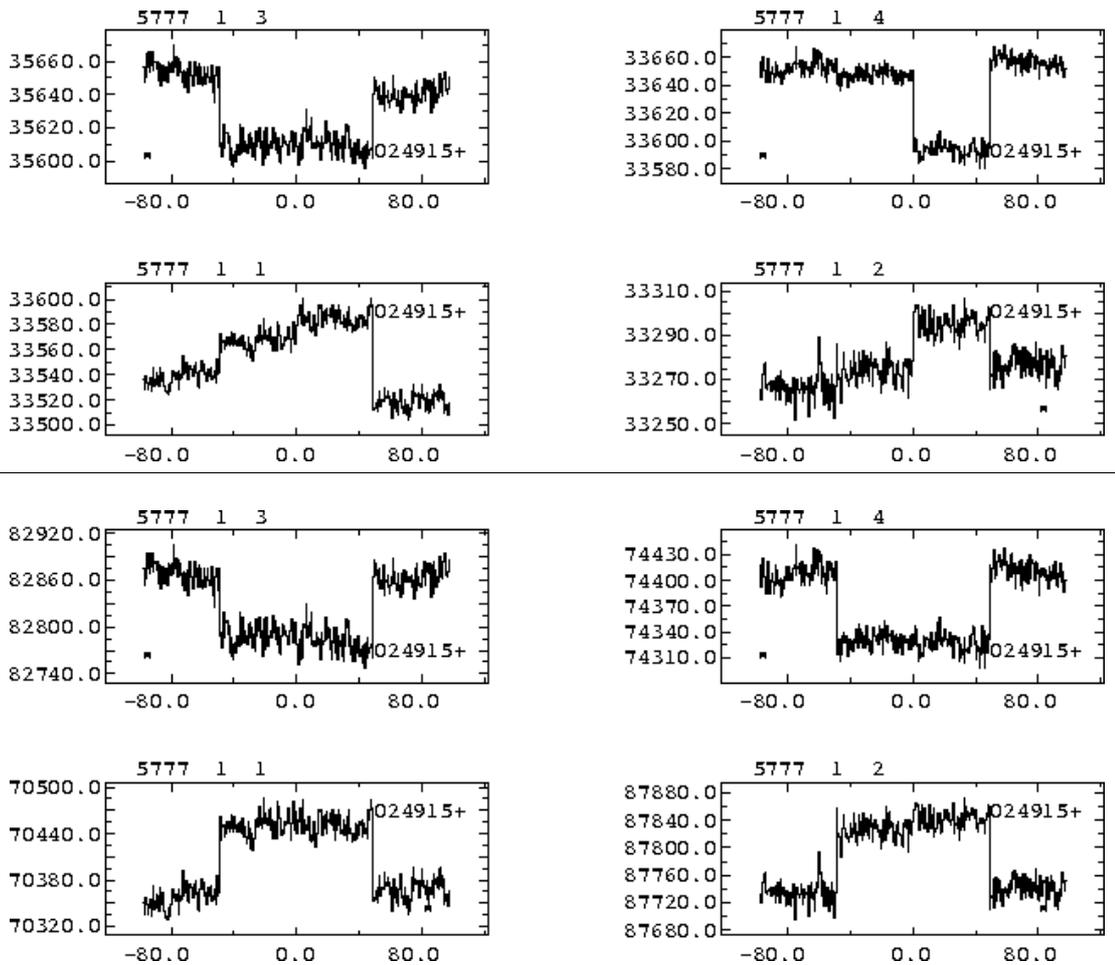
Figure B.5:   **An extreme example of data distortion due to unstable calibration signal compared with non-calibrated data. In the upper frame the data are calibrated within the Effelsberg software according to the traditional routine of point-by-point calibration. In the lower frame they are not calibrated.**
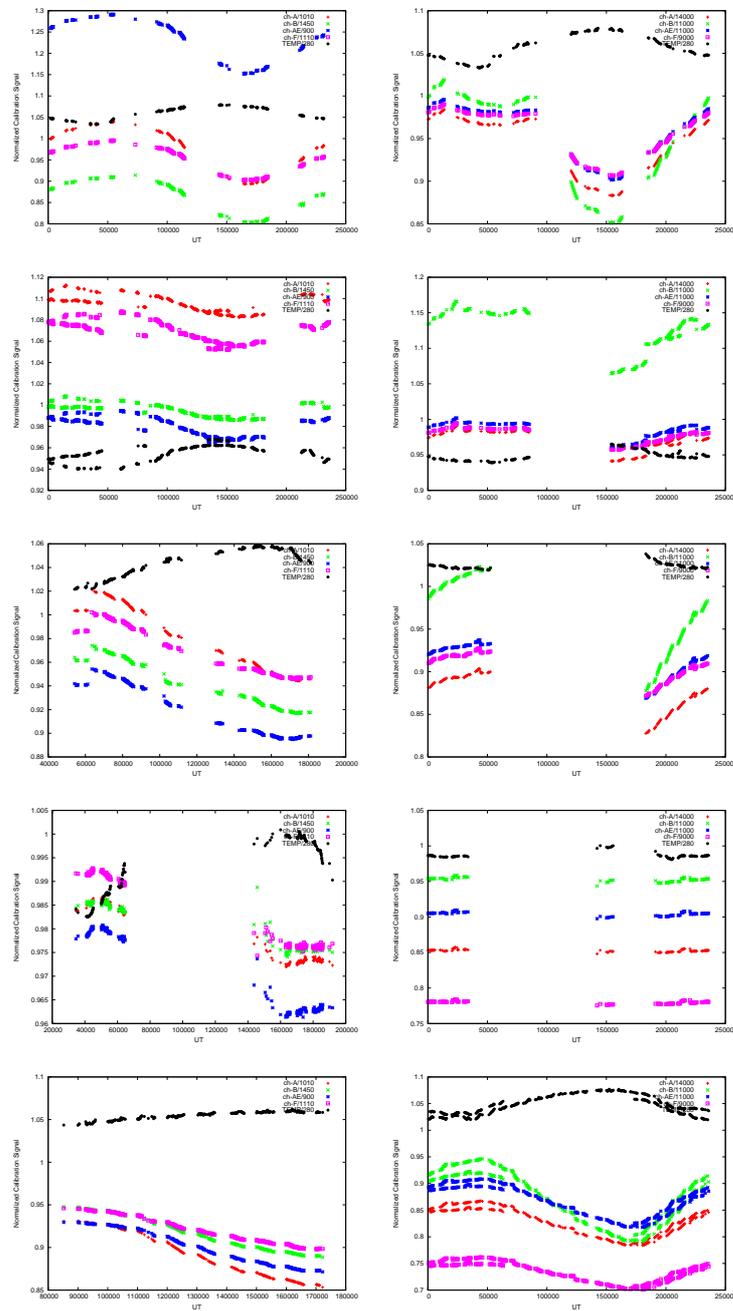
Figure B.6: **Examples inter-scan variations of the calibrations signal for both the 4.85 and 10.45 GHz receiver. Here the normalized** *cal* **signal for each channel is plotted as a function of UT. Also the normalized ambient temperature is shown in black. The temperature dependence is already apparent.**

What causes the instability in cal

In an attempt to inquire the origin of the inter-scan variations discussed previously, it is reasonable to examine three possibilities. (a) changes occurring in the output of the noise diode itself, (b) instabilities in the gain of the receivers or (c) a combination of the two.

In order to get some insight in the reason for this behavior one could investigate a signal free of the gain influence. Lets assume the signal $sig = a_3$ where only phase 3 is kept. This will be:

$$sig = a_3 = g \cdot P + g \cdot D \tag{B.1}$$

where P: the power from the sky
            D: the power from the diode
            g: the gain factor of the receiver

Assume a calibration signal for that as:

$$cal = a_2 = g \cdot P \tag{B.2}$$

Then, the calibration procedure will result a calibrated signal SIG, as:

$$SIG = 1000 \cdot \frac{sig}{cal} = 1000 \cdot \frac{a_3}{a_2} = 1000 \cdot \frac{g \cdot P + g \cdot D}{g \cdot P} = 1000 \cdot \left(1 + \frac{D}{P}\right) \tag{B.3}$$

The factor 1000 is used only for scaling reasons. Plotting then only the sub-scans that are of source will clearly be free of gain influence. As it is shown in figure B.7 (red symbols) the peak-to-peak variation is less than 1 percent. The second signal that has been studied, is CAL from equation B.3 but calibrated as described in subsection 2.1.1 by the signal:

$$CAL = -a_2 - a_2 + a_3 + a_4 = g\, 2\, D \tag{B.4}$$

So, the second signal after applying the calibration formula 2.4 , is:

$$Q = T_{\text{cal}} \frac{SIG}{CAL} = T_{\text{cal}} \frac{1000 \left(1 + \frac{D}{P}\right)}{4\, g\, D} \tag{B.5}$$

which obviously is not free of g anymore.
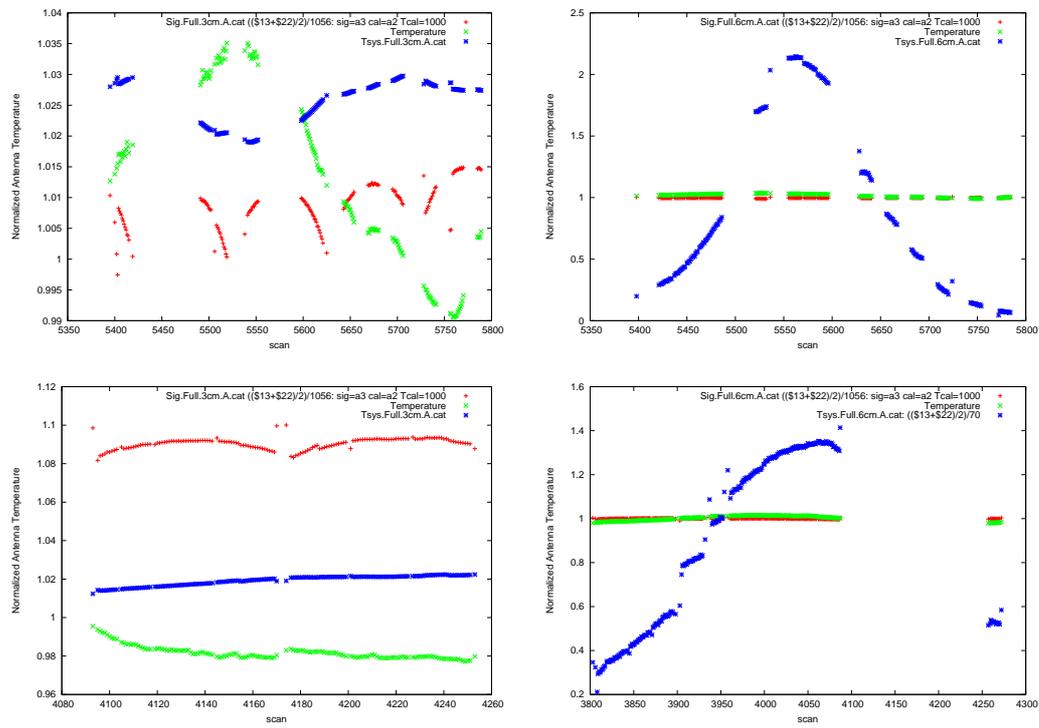
Figure B.7: Distinguishing between a change in the diode output and the change in the receiver gain. In red is shown the signal SIG of equation **B.3** and in blue the signal Q as described in equation **B.5**. These plots speaks in favor of a gain change rather than diode instability.

Bibliography

Alfvén, H. and Herlofson, N.: 1950, Cosmic Radiation and Radio Stars, *Physical Review* **78**, 616–616.

Aller, M. F., Aller, H. D. and Hughes, P. A.: 1992, Pearson-Readhead survey sources - Properties of the centimeter-wavelength flux and polarization of a complete radio sample, *ApJ* **399**, 16–28.

Aller, M. F., Aller, H. D., Hughes, P. A. and Latimer, G. E.: 1999, Centimeter-Wavelength Total Flux and Linear Polarization Properties of Radio-loud BL Lacertae Objects, *ApJ* **512**, 601–622.

Alpher, R. A. and Herman, R. C.: 1950, Theory of the Origin and Relative Abundance Distribution of the Elements, *Reviews of Modern Physics* **22**, 153–212.

Baars, J. W. M., Genzel, R., Pauliny-Toth, I. I. K. and Witzel, A.: 1977, The absolute spectrum of CAS A - an accurate flux density scale and a set of secondary calibrators, *A&A* **61**, 99–106.

Baum, S. A., O'Dea, C. P., de Bruyn, A. G. and Murphy, D. W.: 1990, 0108 + 388 - A compact double source with surprising properties, *A&A* **232**, 19–26.

Bennett, C. L., Hill, R. S., Hinshaw, G., Nolta, M. R., Odegard, N., Page, L., Spergel, D. N., Weiland, J. L., Wright, E. L., Halpern, M., Jarosik, N., Kogut, A., Limon, M., Meyer, S. S., Tucker, G. S. and Wollack, E.: 2003, First-Year Wilkinson Microwave Anisotropy Probe (WMAP) Observations: Foreground Emission, *ApJS* **148**, 97–117.

Bicknell, G. V., Dopita, M. A. and O'Dea, C. P. O.: 1997, Unification of the Radio and Optical Properties of Gigahertz Peak Spectrum and Compact Steep-Spectrum Radio Sources, *ApJ* **485**, 112–+.

Blandford, R. D. and Begelman, M. C.: 1999, On the fate of gas accreting at a low rate on to a black hole, *MNRAS* **303**, L1–L5.

Bolton, J. G., Gardner, F. F. and Mackey, F. B.: 1963, A Radio Source with a Very Unusual Spectrum, *Nature* **199**, 682–+.

Browne, I. W. A., Wilkinson, P. N., Jackson, N. J. F., Myers, S. T., Fassnacht, C. D., Koopmans, L. V. E., Marlow, D. R., Norbury, M., Rusin, D., Sykes, C. M., Biggs, A. D., Blandford, R. D., de Bruyn, A. G., Chae, K.-H., Helbig, P., King, L. J., McKean, J. P., Pearson, T. J., Phillips, P. M., Readhead, A. C. S., Xanthopoulos, E. and York, T.: 2003, The Cosmic Lens All-Sky Survey - II. Gravitational lens candidate selection and follow-up, *MNRAS* **341**, 13–32.

Carilli, C. L., Dreher, J. W. and Perley, R. A.: 1989, Cygnus A and the Williams model, *in* K. Meisenheimer and H.-J. Roeser (eds), *LNP Vol. 327: Hot Spots in Extragalactic Radio Sources*, pp. 51–60.

Cleary, K. A., Taylor, A. C., Waldram, E., Battye, R. A., Dickinson, C., Davies, R. D., Davis, R. J., Genova-Santos, R., Grainge, K., Jones, M. E., Kneissl, R., Pooley, G. G., Rebolo, R., Rubiño-Martín, J. A., Saunders, R. D. E., Scott, P. F., Slosar, A., Titterington, D. and Watson, R. A.: 2005, Source subtraction for the extended Very Small Array and 33-GHz source count estimates, *MNRAS* **360**, 340–353.

Coble, K., Carlstrom, J. E., Bonamente, M., Dawson, K., Holzapfel, W., Joy, M., LaRoque, S. and Reese, E. D.: 2006, Radio Point Sources Toward Galaxy Clusters at 30 GHz, *ArXiv Astrophysics e-prints* .

Condon, J. J.: 1984, Cosmological evolution of radio sources, *ApJ* **287**, 461–474.

Condon, J. J., Broderick, J. J. and Seielstad, G. A.: 1989, A 4.85 GHz sky survey. I - Maps covering delta between 0 and + 75 deg, *AJ* **97**, 1064–1073.

Condon, J. J., Cotton, W. D., Greisen, E. W., Yin, Q. F., Perley, R. A., Taylor, G. B. and Broderick, J. J.: 1998, The NRAO VLA Sky Survey, *AJ* **115**, 1693–1716.

Conway, J.: 1997, VLBI Observations of HI absorption in CSO/SSC's, *in* I. A. G. Snellen, R. T. Schilizzi, H. J. A. Roettgering and M. N. Bremer (eds), *Gigahertz Peaked Spectrum and Compact Steep Spectrum Radio Sources*, pp. 198–207.

Conway, J. E.: 1999, VLBI spectral absorption in AGN, *New Astronomy Review* **43**, 509–513.

Cooray, A. R., Grego, L., Holzapfel, W. L., Joy, M. and Carlstrom, J. E.: 1998, Radio Sources in Galaxy Clusters at 28.5 GHz, *AJ* **115**, 1388–1399.

Dallacasa, D.: 2003, High Frequency Peakers, *Publications of the Astronomical Society of Australia* **20**, 79–84.

Dallacasa, D., Stanghellini, C., Centonza, M. and Fanti, R.: 2000, High frequency peakers. I. The bright sample, *A&A* **363**, 887–900.

Danese, L., Franceschini, A., Toffolatti, L. and de Zotti, G.: 1987, Interpretation of deep counts of radio sources, *ApJ* **318**, L15–L20.

De Breuck, C., Hunstead, R. W., Sadler, E. M., Rocca-Volmerange, B. and Klamer, I.: 2004, A search for distant radio galaxies from SUMSS and NVSS - I. Sample definition, radio and K-band imaging, *MNRAS* **347**, 837–853.

De Breuck, C., van Breugel, W., Röttgering, H., Miley, G. and Stanford, A.: 1999, Searches for High Redshift Radio Galaxies, *in* H. J. A. Röttgering, P. N. Best and M. D. Lehnert (eds), *The Most Distant Radio Galaxies*, pp. 477–+.

De Zotti, G., Ricci, R., Mesa, D., Silva, L., Mazzotta, P., Toffolatti, L. and González-Nuevo, J.: 2005, Predictions for high-frequency radio surveys of extragalactic sources, *A&A* **431**, 893–903.

Dicke, R. H., Peebles, P. J. E., Roll, P. G. and Wilkinson, D. T.: 1965, Cosmic Black-Body Radiation., *ApJ* **142**, 414–419.

Dunlop, J. S. and Peacock, J. A.: 1990, The Redshift Cut-Off in the Luminosity Function of Radio Galaxies and Quasars, *MNRAS* **247**, 19–+.

Fabian, A. C. and Rees, M. J.: 1995, The accretion luminosity of a massive black hole in an elliptical galaxy, *MNRAS* **277**, L55–L58.

Fanti, C., Fanti, R., Dallacasa, D., Schilizzi, R. T., Spencer, R. E. and Stanghellini, C.: 1995, Are compact steep-spectrum sources young?, *A&A* **302**, 317–+.

Fanti, R., Fanti, C., Schilizzi, R. T., Spencer, R. E., Nan Rendong, Parma, P., van Breugel, W. J. M. and Venturi, T.: 1990, On the nature of compact steep spectrum radio sources, *A&A* **231**, 333–346.

Fomalont, E. B., Kellermann, K. I., Partridge, R. B., Windhorst, R. A. and Richards, E. A.: 2002, The Microjansky Sky at 8.4 GHz, *AJ* **123**, 2402–2416.

Fomalont, E. B., Windhorst, R. A., Kristian, J. A. and Kellerman, K. I.: 1991, The micro-Jansky radio source population at 5 GHz, *AJ* **102**, 1258–1277.

Gabuzda, D. C., Mullan, C. M., Cawthorne, T. V., Wardle, J. F. C. and Roberts, D. H.: 1994, Evolution of the milliarcsecond total intensity and polarization structures of BL Lacertae objects, *ApJ* **435**, 140–161.

Gamow, G.: 1946, Expanding Universe and the Origin of Elements, *Physical Review* **70**, 572–573.

Ghisellini, G., Padovani, P., Celotti, A. and Maraschi, L.: 1993, Relativistic bulk motion in active galactic nuclei, *ApJ* **407**, 65–82.

Ginzburg, V. L. and Syrovatskii, S. I.: 1965, Cosmic Magnetobremsstrahlung (synchrotron Radiation), *ARA&A* **3**, 297–+.

Gregory, P. C., Scott, W. K., Douglas, K. and Condon, J. J.: 1996, The GB6 Catalog of Radio Sources, *ApJS* **103**, 427–+.

Heeschen, D. S., Krichbaum, T., Schalinski, C. J. and Witzel, A.: 1987, Rapid variability of extragalactic radio sources, *AJ* **94**, 1493–1507.

Hinshaw, G., Nolta, M. R., Bennett, C. L., Bean, R., Dore', O., Greason, M. R., Halpern, M., Hill, R. S., Jarosik, N., Kogut, A., Komatsu, E., Limon, M., Odegard, N., Meyer, S. S., Page, L., Peiris, H. V., Spergel, D. N., Tucker, G. S., Verde, L., Weiland, J. L., Wollack, E. and Wright, E. L.: 2006, Three-Year Wilkinson Microwave Anisotropy Probe (WMAP) Observations: Temperature Analysis, *ArXiv Astrophysics e-prints* .

Hubble, E.: 1929, A Relation between Distance and Radial Velocity among Extra-Galactic Nebulae, *Proceedings of the National Academy of Science* **15**, 168–173.

Jackson, C. A. and Wall, J. V.: 1999, Extragalactic radio-source evolution under the dual-population unification scheme, *MNRAS* **304**, 160–174.

Jones, M. E.: 1991, Microwave background interferometry in Cambridge, *in* T. J. Cornwell and R. A. Perley (eds), *ASP Conf. Ser. 19: IAU Colloq. 131: Radio Interferometry. Theory, Techniques, and Applications*, pp. 395–399.

Jones, T. W. and Odell, S. L.: 1977, Transfer of polarized radiation in self-absorbed synchrotron sources. I - Results for a homogeneous source, *ApJ* **214**, 522–539.

Kadler, M., Ros, E., Lobanov, A. P., Falcke, H. and Zensus, J. A.: 2004, The twin-jet system in NGC 1052: VLBI-scrutiny of the obscuring torus, *A&A* **426**, 481–493.

Keating, B., Timbie, P., Polnarev, A. and Steinberger, J.: 1998, Large Angular Scale Polarization of the Cosmic Microwave Background Radiation and the Feasibility of Its Detection, *ApJ* **495**, 580–+.

Kellermann, K. I., Lister, M. L., Homan, D. C., Vermeulen, R. C., Cohen, M. H., Ros, E., Kadler, M., Zensus, J. A. and Kovalev, Y. Y.: 2004, Sub-Milliarcsecond Imaging of Quasars and Active Galactic Nuclei. III. Kinematics of Parsec-scale Radio Jets, *ApJ* **609**, 539–563.

Kellermann, K. I. and Pauliny-Toth, I. I. K.: 1969, The Spectra of Opaque Radio Sources, *ApJ* **155**, L71+.

Kiepenheuer, K. O.: 1950, Cosmic Rays as the Source of General Galactic Radio Emission, *Physical Review* **79**, 738–739.

Klamer, I. J., Ekers, R. D., Bryant, J. J., Hunstead, R. W., Sadler, E. M. and de Breuck, C.: 2006, A search for distant radio galaxies from SUMSS and NVSS - III. Radio spectral energy distributions and the z-α correlation, *MNRAS* **371**, 852–866.

Klein, U., Mack, K.-H., Gregorini, L. and Vigotti, M.: 2003, Multi-frequency study of the B3-VLA sample. III. Polarisation properties, *A&A* **406**, 579–592.

Kovac, J. M., Leitch, E. M., Pryke, C., Carlstrom, J. E., Halverson, N. W. and Holzapfel, W. L.: 2002, Detection of polarization in the cosmic microwave background using DASI, *Nature* **420**, 772–787.

Kraus, A.: 1997, *Ph.D. Thesis* .

Kraus, A., Krichbaum, T. P., Wegner, R., Witzel, A., Cimò, G., Quirrenbach, A., Britzen, S., Fuhrmann, L., Lobanov, A. P., Naundorf, C. E., Otterbein, K., Peng, B., Risse, M., Ros, E. and Zensus, J. A.: 2003, Intraday variability in compact extragalactic radio sources. II. Observations with the Effelsberg 100 m radio telescope, *A&A* **401**, 161–172.

Kraus, J. D.: 1986, *Radio astronomy*, Powell, Ohio: Cygnus-Quasar Books, 1986.

Kristian, J., Sandage, A. and Katem, B.: 1974, On the systematic optical identification of the remaining 3C radio sources. I. A search in 47 fields., *ApJ* **191**, 43–50.

Krolik, J. H. and Chen, W.: 1991, Steep radio spectra in high-redshift radio galaxies, *AJ* **102**, 1659–1662.

Le Roux, E.: 1961, Étude théorique du rayonnement synchrotron des radiosources, *Annales d'Astrophysique* **24**, 71–+.

Lister, M. L. and Homan, D. C.: 2005, MOJAVE: Monitoring of Jets in Active Galactic Nuclei with VLBA Experiments. I. First-Epoch 15 GHz Linear Polarization Images, *AJ* **130**, 1389–1417.

Longair, M. S.: 1994, *High energy astrophysics. Vol.2: Stars, the galaxy and the interstellar medium*, Cambridge: Cambridge University Press, —c1994, 2nd ed.

Marecki, A., Falcke, H., Niezgoda, J., Garrington, S. T. and Patnaik, A. R.: 1999, Gigahertz Peaked Spectrum sources from the Jodrell Bank-VLA Astrometric Survey. I. Sources in the region 35degr lt= delta lt= 75degr, *A&AS* **135**, 273–289.

Marquardt, D. W.: 1963, An algorithm for least-squares estimation of nonlinear parameters, *Journal of the Society for Industrial and Applied Mathematics* **11**(2), 431–441.

Marscher, A. P. and Gear, W. K.: 1985, Models for high-frequency radio outbursts in extragalactic sources, with application to the early 1983 millimeter-to-infrared flare of 3C 273, *ApJ* **298**, 114–127.

Marscher, A. P., Marshall, F. E., Mushotzky, R. F., Dent, W. A., Balonek, T. J. and Hartman, M. F.: 1979, Search for X-ray emission from bursting radio sources, *ApJ* **233**, 498–503.

Mason, B. S., Pearson, T. J., Readhead, A. C. S., Shepherd, M. C., Sievers, J., Udomprasert, P. S., Cartwright, J. K., Farmer, A. J., Padin, S., Myers, S. T., Bond, J. R., Contaldi, C. R., Pen, U., Prunet, S., Pogosyan, D., Carlstrom, J. E., Kovac, J., Leitch, E. M., Pryke, C., Halverson, N. W., Holzapfel, W. L., Altamirano, P., Bronfman, L., Casassus, S., May, J. and Joy, M.: 2003, The Anisotropy of the Microwave Background to l = 3500: Deep Field Observations with the Cosmic Background Imager, *ApJ* **591**, 540–555.

Mather, J. C.: 1982, The Cosmic Background Explorer /COBE/, *Optical Engineering* **21**, 769–774.

Mesa, D., Baccigalupi, C., De Zotti, G., Gregorini, L., Mack, K.-H., Vigotti, M. and Klein, U.: 2002, Polarization properties of extragalactic radio sources and their contribution to microwave polarization fluctuations, *A&A* **396**, 463–471.

Myers, S. T., Jackson, N. J., Browne, I. W. A., de Bruyn, A. G., Pearson, T. J., Readhead, A. C. S., Wilkinson, P. N., Biggs, A. D., Blandford, R. D., Fassnacht, C. D., Koopmans, L. V. E., Marlow, D. R., McKean, J. P., Norbury, M. A., Phillips, P. M., Rusin, D., Shepherd, M. C. and Sykes, C. M.: 2003, The Cosmic Lens All-Sky Survey - I. Source selection and observations, *MNRAS* **341**, 1–12.

O'Dea, C. P.: 1998, The Compact Steep-Spectrum and Gigahertz Peaked-Spectrum Radio Sources, *PASP* **110**, 493–532.

O'Dea, C. P. and Baum, S. A.: 1997, Constraints on Radio Source Evolution from the Compact Steep Spectrum and GHz Peaked Spectrum Radio Sources, *AJ* **113**, 148–161.

Okudaira, A., Tabara, H., Kato, T. and Inoue, M.: 1993, Radio polarization observations of a complete sample of core-dominated radio sources, *PASJ* **45**, 153–166.

Ott, M., Witzel, A., Quirrenbach, A., Krichbaum, T. P., Standke, K. J., Schalinski, C. J. and Hummel, C. A.: 1994, An updated list of radio flux density calibrators, *A&A* **284**, 331–339.

Padin, S., Cartwright, J. K., Mason, B. S., Pearson, T. J., Readhead, A. C. S., Shepherd, M. C., Sievers, J., Udomprasert, P. S., Holzapfel, W. L., Myers, S. T., Carlstrom, J. E., Leitch, E. M., Joy, M., Bronfman, L. and May, J.: 2001, First Intrinsic Anisotropy Observations with the Cosmic Background Imager, *ApJ* **549**, L1–L5.

Padin, S., Shepherd, M. C., Cartwright, J. K., Keeney, R. G., Mason, B. S., Pearson, T. J., Readhead, A. C. S., Schaal, W. A., Sievers, J., Udomprasert, P. S., Yamasaki, J. K., Holzapfel, W. L., Carlstrom, J. E., Joy, M., Myers, S. T. and Otarola, A.: 2002, The Cosmic Background Imager, *PASP* **114**, 83–97.

Park, C.-G., Park, C. and Ratra, B.: 2002, Effects of Foreground Contamination on the Cosmic Microwave Background Anisotropy Measured by MAP, *ApJ* **568**, 9–19.

Partridge, R. B., Richards, E. A., Fomalont, E. B., Kellermann, K. I. and Windhorst, R. A.: 1997, Small-Scale Cosmic Microwave Background Observations at 8.4 GHz, *ApJ* **483**, 38–+.

Peacock, J. A.: 1999, *Cosmological Physics*, Cosmological Physics, by John A. Peacock, pp. 704. ISBN 052141072X. Cambridge, UK: Cambridge University Press, January 1999.

Pearson, T. J. and Readhead, A. C. S.: 1988, The milliarcsecond structure of a complete sample of radio sources. II - First-epoch maps at 5 GHz, *ApJ* **328**, 114–142.

Penzias, A. A. and Wilson, R. W.: 1965, A Measurement of Excess Antenna Temperature at 4080 Mc/s., *ApJ* **142**, 419–421.

Peterson, B. M.: 1997, *An Introduction to Active Galactic Nuclei*, An introduction to active galactic nuclei, Publisher: Cambridge, New York Cambridge University Press, 1997 Physical description xvi, 238 p. ISBN 0521473489.

Pierce, M., Brodie, J. P., Forbes, D. A., Beasley, M. A., Proctor, R. and Strader, J.: 2005, Evolutionary history of the elliptical galaxy NGC 1052, *MNRAS* **358**, 419–431.

Polatidis, A. G. and Conway, J. E.: 2003, Proper Motions in Compact Symmetric Objects, *Publications of the Astronomical Society of Australia* **20**, 69–74.

Readhead, A. C. S.: 1994, Equipartition brightness temperature and the inverse Compton catastrophe, *ApJ* **426**, 51–59.

Readhead, A. C. S., Myers, S. T., Pearson, T. J., Sievers, J. L., Mason, B. S., Contaldi, C. R., Bond, J. R., Bustos, R., Altamirano, P., Achermann, C., Bronfman, L., Carlstrom, J. E., Cartwright, J. K., Casassus, S., Dickinson, C., Holzapfel, W. L., Kovac, J. M., Leitch, E. M., May, J., Padin, S., Pogosyan, D., Pospieszalski, M., Pryke, C., Reeves, R., Shepherd, M. C. and Torres, S.: 2004, Polarization Observations with the Cosmic Background Imager, *Science* **306**, 836–844.

Readhead, A. C. S., Taylor, G. B., Pearson, T. J. and Wilkinson, P. N.: 1996, Compact Symmetric Objects and the Evolution of Powerful Extragalactic Radio Sources, *ApJ* **460**, 634–+.

Rees, M. J.: 1967, Studies in radio structure-II. The relaxation of relativistic electron spectra in self-absorbed radio sources, *MNRAS* **136**, 279–+.

Refregier, A.: 1999, Overview of Secondary Anisotropies of the CMB, *in* A. de Oliveira-Costa and M. Tegmark (eds), *ASP Conf. Ser. 181: Microwave Foregrounds*, pp. 219–+.

Refregier, A., Spergel, D. N. and Herbig, T.: 2000, Extragalactic Foregrounds of the Cosmic Microwave Background: Prospects for the MAP Mission, *ApJ* **531**, 31–41.

Ricci, R., Prandoni, I., Gruppioni, C., Sault, R. J. and De Zotti, G.: 2004, High-frequency polarization properties of southern Kühr sources, *A&A* **415**, 549–558.

Ricci, R., Prandoni, I., Gruppioni, C., Sault, R. J. and de Zotti, G.: 2006, High-frequency radio observations of the Kühr sample and the epoch-dependent luminosity function of flat-spectrum quasars, *A&A* **445**, 465–469.

Ricci, R., Sadler, E. M., Ekers, R. D., Staveley-Smith, L., Wilson, W. E., Kesteven, M. J., Subrahmanyan, R., Walker, M. A., Jackson, C. A. and De Zotti, G.: 2004, First results from the Australia Telescope Compact Array 18-GHz pilot survey, *MNRAS* **354**, 305–320.

Rohlfs, K. and Wilson, T. L.: 2004, *Tools of radio astronomy*, Tools of radio astronomy, 4th rev. and enl. ed., by K. Rohlfs and T.L. Wilson. Berlin: Springer, 2004.

Rudnick, L., Jones, T. W., Fiedler, R. L., Aller, H. D., Aller, M. F., Hodge, P. E., Owen, F. N., Bignell, R. C. and Puschell, J. J.: 1985, Broad-band polarization observations of active compact radio sources, *ApJS* **57**, 693–709.

Rybicki, G. B. and Lightman, A. P.: 1986, *Radiative Processes in Astrophysics*, Radiative Processes in Astrophysics, by George B. Rybicki, Alan P. Lightman, pp. 400. ISBN 0-471-82759-2. Wiley-VCH , June 1986.

Scheuer, P. A. G.: 1957, A statistical method for analysing observations of faint radio stars, *Proceedings of the Cambridge Philisophical Society*, pp. 764–773.

Seymour, N., McHardy, I., Gunn, K. and Moss, D.: 2005, The nature of the faint sub-mJy radio population, *in* A. Wilson (ed.), *The Dusty and Molecular Universe: A Prelude to Herschel and ALMA*, pp. 323–324.

Smoot, G. F.: 1999, CMB Synchrotron Foreground, *in* A. de Oliveira-Costa and M. Tegmark (eds), *ASP Conf. Ser. 181: Microwave Foregrounds*, pp. 61–+.

Smoot, G. F., Bennett, C. L., Kogut, A., Wright, E. L., Aymon, J., Boggess, N. W., Cheng, E. S., de Amici, G., Gulkis, S., Hauser, M. G., Hinshaw, G., Jackson, P. D., Janssen, M., Kaita, E., Kelsall, T., Keegstra, P., Lineweaver, C., Loewenstein, K., Lubin, P., Mather, J., Meyer, S. S., Moseley, S. H., Murdock, T., Rokke, L., Silverberg, R. F., Tenorio, L., Weiss, R. and Wilkinson, D. T.: 1992, Structure in the COBE differential microwave radiometer first-year maps, *ApJ* **396**, L1–L5.

Snellen, I. A. G., Schilizzi, R. T., de Bruyn, A. G., Miley, G. K., Rengelink, R. B., Roettgering, H. J. and Bremer, M. N.: 1998, A new sample of faint Gigahertz Peaked Spectrum radio sources, *A&AS* **131**, 435–449.

Snellen, I. A. G., Schilizzi, R. T., Miley, G. K., de Bruyn, A. G., Bremer, M. N. and Röttgering, H. J. A.: 2000, On the evolution of young radio-loud AGN, *MNRAS* **319**, 445–456.

Sokasian, A., Gawiser, E. and Smoot, G. F.: 2001, Contribution of Bright Extragalactic Radio Sources to Microwave Anisotropy, *ApJ* **562**, 88–94.

Steppe, H., Jeyakumar, S., Saikia, D. J. and Salter, C. J.: 1995, Millimeter-wavelength observations of compact steep-spectrum sources., *A&AS* **113**, 409–+.

Stokes, G. C.: 1852, On the composition and resolution of streams of polarized light from different sources, *Trans. Cambridge Philos. Soc.* **9**, 399–416.

Sunyaev, R. A. and Zeldovich, Y. B.: 1970, Small-Scale Fluctuations of Relic Radiation, *Ap&SS* **7**, 3–+.

Sunyaev, R. A. and Zeldovich, Y. B.: 1972, The Observations of Relic Radiation as a Test of the Nature of X-Ray Radiation from the Clusters of Galaxies, *Comments on Astrophysics and Space Physics* **4**, 173–+.

Taylor, A. C., Carreira, P., Cleary, K., Davies, R. D., Davis, R. J., Dickinson, C., Grainge, K., Gutiérrez, C. M., Hobson, M. P., Jones, M. E., Kneissl, R., Lasenby, A., Leahy, J. P., Maisinger, K., Pooley, G. G., Rebolo, R., Rubiño-Martin, J. A., Rusholme, B., Saunders, R. D. E., Savage, R., Scott, P. F., Slosar, A., Sosa Molina, P. J., Titterington, D., Waldram, E., Watson, R. A. and Wilkinson, A.: 2003, First results from the Very Small Array - II. Observations of the cosmic microwave background, *MNRAS* **341**, 1066–1075.

Taylor, A. C., Grainge, K., Jones, M. E., Pooley, G. G., Saunders, R. D. E. and Waldram, E. M.: 2001, The radio source counts at 15 GHz and their implications for cm-wave CMB imaging, *MNRAS* **327**, L1–L4.

Tegmark, M., Eisenstein, D. J., Hu, W. and de Oliveira-Costa, A.: 2000, Foregrounds and Forecasts for the Cosmic Microwave Background, *ApJ* **530**, 133–165.

Tinti, S., Dallacasa, D., de Zotti, G., Celotti, A. and Stanghellini, C.: 2005, High Frequency Peakers: Young radio sources or flaring blazars?, *A&A* **432**, 31–43.

Toffolatti, L., Argueso Gomez, F., de Zotti, G., Mazzei, P., Franceschini, A., Danese, L. and Burigana, C.: 1998, Extragalactic source counts and contributions to the anisotropies of the cosmic microwave background: predictions for the Planck Surveyor mission, *MNRAS* **297**, 117–127.

Turlo, Z., Forkert, T., Sieber, W. and Wilson, W.: 1985, Calibration of the instrumental polarization of radio telescopes, *A&A* **142**, 181–188.

von Hoerner, S.: 1967, Design of large steerable antennas, *AJ* **72**, 35–+.

Waldram, E. M., Pooley, G. G., Grainge, K. J. B., Jones, M. E., Saunders, R. D. E., Scott, P. F. and Taylor, A. C.: 2003, 9C: a survey of radio sources at 15 GHz with the Ryle Telescope, *MNRAS* **342**, 915–925.

Watson, R. A., Carreira, P., Cleary, K., Davies, R. D., Davis, R. J., Dickinson, C., Grainge, K., Gutiérrez, C. M., Hobson, M. P., Jones, M. E., Kneissl, R., Lasenby, A., Maisinger, K., Pooley, G. G., Rebolo, R., Rubiño-Martin, J. A., Rusholme, B., Saunders, R. D. E., Savage, R., Scott, P. F., Slosar, A., Sosa Molina, P. J., Taylor, A. C., Titterington, D., Waldram, E. and Wilkinson, A.: 2003, First results from the Very Small Array - I. Observational methods, *MNRAS* **341**, 1057–1065.

Weiler, K. W. and de Pater, I.: 1983, A catalog of high accuracy circular polarization measurements, *ApJS* **52**, 293–327.

White, M. and Cohn, J. D.: 2002, The theory of anisotropies in the cosmic microwave background, *American Journal of Physics* **70**, 106–118.

White, R. L., Becker, R. H., Helfand, D. J. and Gregg, M. D.: 1997, A Catalog of 1.4 GHz Radio Sources from the FIRST Survey, *ApJ* **475**, 479–+.

Windhorst, R. A., Fomalont, E. B., Partridge, R. B. and Lowenthal, J. D.: 1993, Microjansky source counts and spectral indices at 8.44 GHz, *ApJ* **405**, 498–517.

Witzel, A., Heeschen, D. S., Schalinski, C. and Krichbaum, T.: 1986, Kurzzeit-Variabilität extragalaktischer Radioquellen, *Mitteilungen der Astronomischen Gesellschaft Hamburg* **65**, 239–+.

Wright, A. E., Griffith, M. R., Burke, B. F. and Ekers, R. D.: 1994, The Parkes-MIT-NRAO (PMN) surveys. 2: Source catalog for the southern survey (delta greater than -87.5 deg and less than -37 deg), *ApJS* **91**, 111–308.

Wright, E. L.: 1987, Long-wavelength absorption by fractal dust grains, *ApJ* **320**, 818–824.

Wrobel, J. M. and Heeschen, D. S.: 1984, Compact-core-dominated radio emission from bright E/S0 galaxies, *ApJ* **287**, 41–65.

Zensus, J. A. and Pearson, T. J. (eds): 1990, *Parsec-Scale Radio Jets*.